11

NASA CR-144500

E7.6-10154

EXPERIMENTAL EVALUATION OF ATMOSPHERIC EFFECTS ON RADIOMETRIC MEASUREMENTS USING THE EREP OF SKYLAB

ERT Document No. 0410-F

Final Report

December 1975

Contract No. NAS 9-013343

RONALD G. ISAACS

DAVID T. CHANG

prepared for

PRINCIPAL INVESTIGATOR OFFICE

NATIONAL AERONAUTICS AND SPACE ADMINISTRATION

LYNDON B. JOHNSON SPACE CENTER

HOUSTON, TEXAS 77958

ENVIRONMENTAL RESEARCH & TECHNOLOGY, INC.

696 VIRGINIA ROAD, CONCORD, MA. 01742 (617) 369-8910

EXPERIMENTAL EVALUATION OF ATMOSPHERIC EFFECTS ON RADIOMETRIC MEASUREMENTS USING THE EREP OF SKYLAB

ERT Document No. 0410-F
Final Report

December 1975

Contract No. NAS 9- 13343

RONALD G. ISAACS
DAVID T. CHANG - PRINCIPAL INVESTIGATOR

prepared for
PRINCIPAL INVESTIGATOR OFFICE
NATIONAL AERONAUTICS AND SPACE ADMINISTRATION
LYNDON B. JOHNSON SPACE CENTER
HOUSTON, TEXAS 77958

ENVIRONMENTAL RESEARCH
& TECHNOLOGY, INC.
696 VIRGINIA ROAD, CONCORD, MA. 01742 (617) 369-8910

ABSTRACT

The objective of the study was to study the effects of the atmosphere on remote sensing of Earth Resources. In particular, the study made use of the Skylab/EREP measurements, especially those obtained by the S192 Experiment, as base for comparison with model calculations.

Four test cases over two target areas of Skylab data were selected for analysis. The target areas were (1) in the vicinity of the Great Salt Lake and (2) in the vicinity of the Salton Sea. Comparisons of Skylab measurements with computation values suggests that, for the purpose at hand, the model adequately represents the measurement situation.

Using the "calibrated" model, computations were made on the effects of the atmosphere on certain radiometric parameters commonly used in earth resources studies. These parameters include radiance, surface reflectance, reflectance contrast, spectral contrast, and other derived parameters. Graphs to assist in the correction of atmospheric effects are also provided.

TABLE OF CONTENTS

LIST OF ILLUSTRATIONS

LIST OF TABLES

1. INTRODUCTION

Techniques for monitoring earth resources using multispectral sensors at visible and near-infrared wavelengths rely on the observer's ability to establish a one-to-one correspondence between the spectral properties of the surface and those of the reflected solar radiation measured at the spacecraft. Unfortunately, the atmosphere between the spacecraft sensor and the surface target is an integral, though generally uncontrollable, part of the total measurement system. Atmospheric gases and particles absorb, emit, and scatter solar radiation in a unique and spectrally structured manner. Consequently, the sensor responds not only to the radiant energy reflected by the target surface, but also to the radiative processes of the atmosphere within its field of view. In the context of resource monitoring, these latter contributions to the measured intensity constitute a source of system introduced noise which may effect spectrum matching techniques of surface type classification.

The intensity of the atmospheric noise is dependent on a number of factors including the wavelength of measurement, solar elevation angle, sensor viewing geometry, and composition of the atmosphere. For most measurement situations, the geometric factors are known or can be readily determined. The composition of the atmosphere at the time of measurement, however, is generally unknown. To the extent that this is unknown, the quantitative interpretation of the remote measurements must remain ambiguous.

In the past, a number of techniques have been proposed and investigated to provide atmospheric correction factors to measurements from spacecraft sensors. These have ranged in scope from radiative transfer computations to the use of strictly empirical correction factors derived from actual measurements. In this study, evaluations have been made of the atmospheric effects influencing measurements using the SKYLAB EREP S192 MSS providing high spatial-resolution, quantitative, line scan data on the solar radiation that is reflected in twelve spectral intervals in the visible and near-infrared and emitted radiation in one thermal band covering those regions most extensively used in aircraft surveys of earth resources.

Theoretical calculations have been performed utilizing a simple surface-atmosphere geophysical model and the SKYLAB EREP S192 band spectral response functions to reproduce synthetic radiance spectra characteristic of given viewing configurations and surface types. Analogous spectra for the hypothetical case of no atmosphere are also calculated to provide a calibration of the atmospheric correction. The spectral character of the results are dependent upon: (1) the atmosphere's transmission and scattering properties; (2) the surface reflectance spectrum; and (3) the sensor response characteristics. The surface is assumed to be a Lambert reflector (usually a good assumption at high solar elevation angles) and the atmosphere diffuse reflected solar radiation (path radiance) is interpolated from exact radiative transfer calculations. Computations of atmospheric transmissivities require a thorough knowledge of the abundances and vertical distributions of radiatively active gases (primarily H_2O and O_3 in this spectral region) in addition to temperature structure and aerosol content. This information is input in the form of a finite number of model atmospheres.

Synthetic radiance values computed using nearby radiosonde data are compared with actual S192 digital data measured over selected test sites. These include the Salton Sea Desert (#547119) and the Great Salt Lake-Bonneville region (#547220). Ground truth assembled for the latter site include in situ reflectance and incident radiation measurements in addition to basic meteorological parameters. For each test site maps were prepared to appropriate scale from S190B earth terrain photography to document the relative surface homogeneity of the particular area to be investigated and serve as base maps. Overlays were prepared to scale which delineate the surface distribution of mineralogical species and relate regions of relatively uniform topography. Minerological information (to indicate reflectance properties) has been extracted from appropriate USGS, state, and local maps which are available. A geological analysis was prepared for each site to accompany and explain the map overlays. These reports discuss surface minerology, uniformity, and morphology in addition to containing a key to the overlay. Specific S192 digital data elements are ground correlated using a two level density slicing technique on chosen S192 MSS raw channel counts. Calibrated radiances for specific scan lines and pixels are then obtained. Comparison between actual and synthetic radiances enables an assessment to be made regarding the accuracy of the model calculation.

2. ATMOSPHERIC EFFECTS

This study is concerned with the potential effect of the atmosphere in degrading the quality of earth resources data obtainable from spectral data in the visible and near-infrared regions covered by the EREP S192 MSS. To achieve this goal and to obtain synthetic radiance spectra from model calculations due consideration must be taken of those processes influencing the reflection of incident solar radiation from the earth-atmosphere system. This section will discuss the particular influence of the atmosphere on radiation of visible and near-infrared wavelengths.

The atmosphere is composed primarily of nitrogen, oxygen, and traces of carbon dioxide, water vapor, inert gases, and aerosol. As incident solar radiation interacts with these atmospheric constituents the transmission of the beam is selectively modified as a function of wavelength due to the spectral character of the interaction mechanisms. These include both molecular absorptions at specific wavelengths (removal of photons from incident beam) and molecular and aerosol scattering (redirection of photons in incident beam).

Figure 2.1 illustrates the relationship between EREP S192 band response and the fundamental atmospheric extinction (= scattering + absorption) properties. Atmospheric transmittance [= $\exp(-\tau)$, where τ is the total atmospheric optical path or the extinction per unit length integrated along the geometric path] from sea level to space is plotted against wavenumber [wavenumber (cm^{-1}) = 10^5/wavelength (μm)] for a summer midlatitude atmosphere (Selby and McClatchey, 1972). Along the upper part of the figure are overlapping wedges delineating the spectral response regions for each of the EREP S192 visible and near-infrared bands. Rather than using the nominal band responses [i.e. band 1 (.41-.46 μm), band 2 (.26-.51 μm)] which are only approximate, maximum sensitivity has been plotted at a response weighted mean wavenumber for each band:

$$\bar{\nu}_i = \int_0^\infty \nu\phi_i(\nu)d\nu \Big/ \int_0^\infty \phi_i(\nu)d\nu \tag{2.1}$$

where ϕ_i is the spectral responsivity of the i^{th} band (NASA-JSC, 1973). Upper and lower limits are set where response falls to less than approximately 1.0%. As can be seen there is considerable overlap between the bands. In this manner true spectral sensitivity of each band to an atmos-

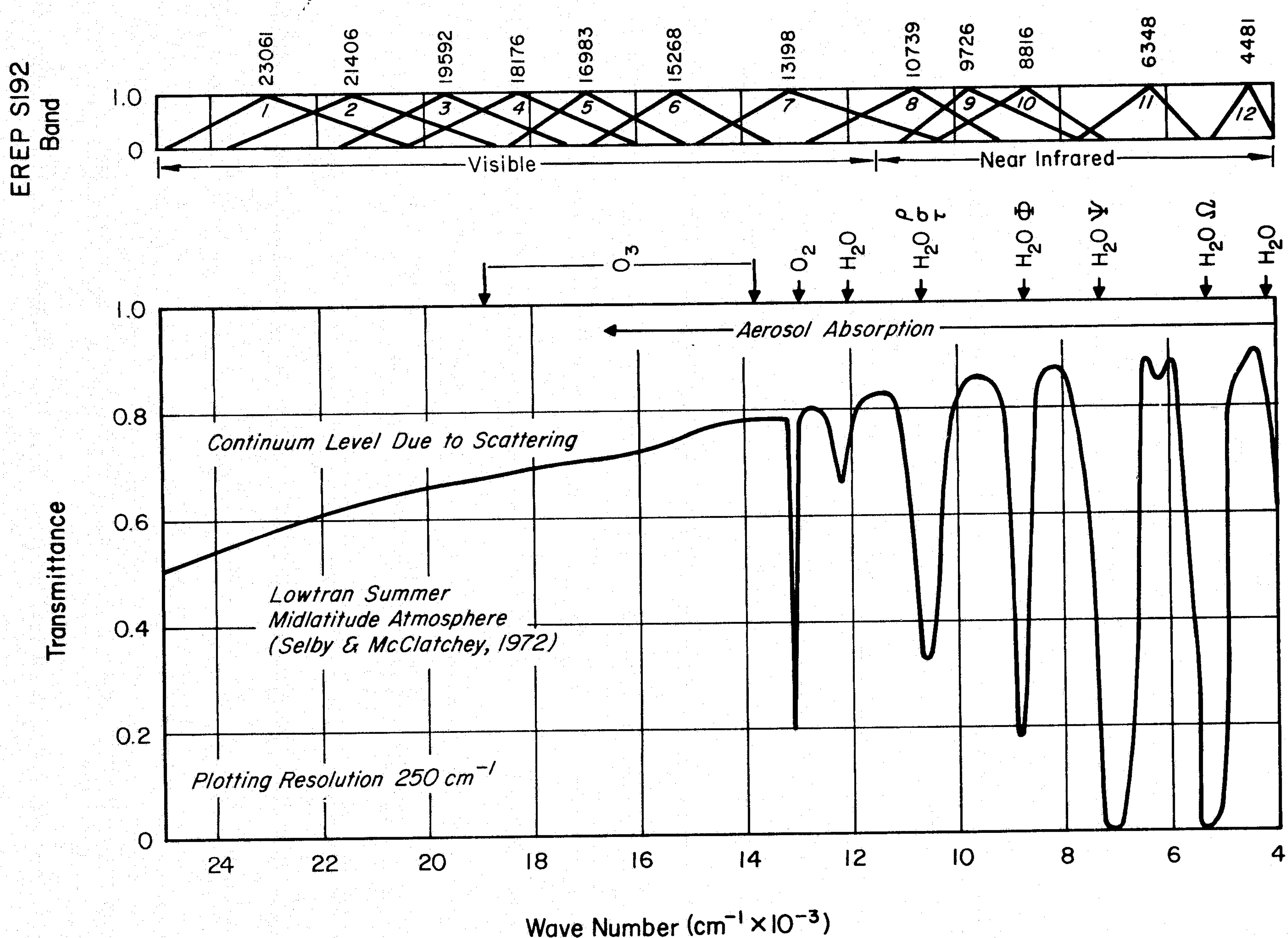

Figure 2.1 Relationship between S192 Bands and Atmospheric Extiction

pheric extinction mechanism can be seen. Plotted along the middle of the figure are the location of significant interaction mechanisms.

As can be seen from the figure, water vapor bands are plentiful in this spectral region (.40-2.50 μm:25000-4000 cm^{-1}). Bands in the visible are relatively weak ground state transitions while those in the near-infrared are quite strong and completely black out the solar spectrum (Goody, 1964). The near-IR bands are commonly identified by the Greek letters: Ω, Ψ, Φ, ρ, σ, τ. Approximate band centers are located by arrows. When transmittance is much less than one, very little information concerning the surface can be obtained. Although EREP S192 bands were chosen to be in "window" or relatively transparent regions in the near-IR, it can be seen that some band "wings" may be affected by atmospheric absorptions due to the strong H_2O bands.

In the visible region there is some weak absorption due to the Chappuis bands of ozone between 15,000 and 18,000 cm^{-1}, however, by far the most important interaction mechanisms are those due to scattering by molecules and aerosol. These processes produce the continuum extinction upon which the molecular absorptions are superimposed. As can be seen, attenuation due to scattering increases markedly at higher wavenumbers (shorter wavelength). Thus, we expect the visible S192 bands to be most critically affected.

Figure 2.2 illustrates the spectral modification of incoming solar radiation by the atmosphere whose transmittance is plotted above. Also included are a set of measurements of the attenuated direct solar beam gathered as ground truth during one of the EREP passes (Salt Lake Desert, EREP pass 5, Ground Track 34, Rev. 318/319, 6-5-73). Agreement is quite good. The reduced solar beam which reaches the surface is available for back-reflection to space by the surface. Since it is this back-reflected component which is measured, information concerning the surface (as manifested in its reflection properties) is coupled with the atmosphere's effect on both the incoming solar beam and the exiting reflected beam. Note that scattering (in the visible) and molecular absorption (in the near-IR) decrease the available energy by a factor of approximately two.

507037

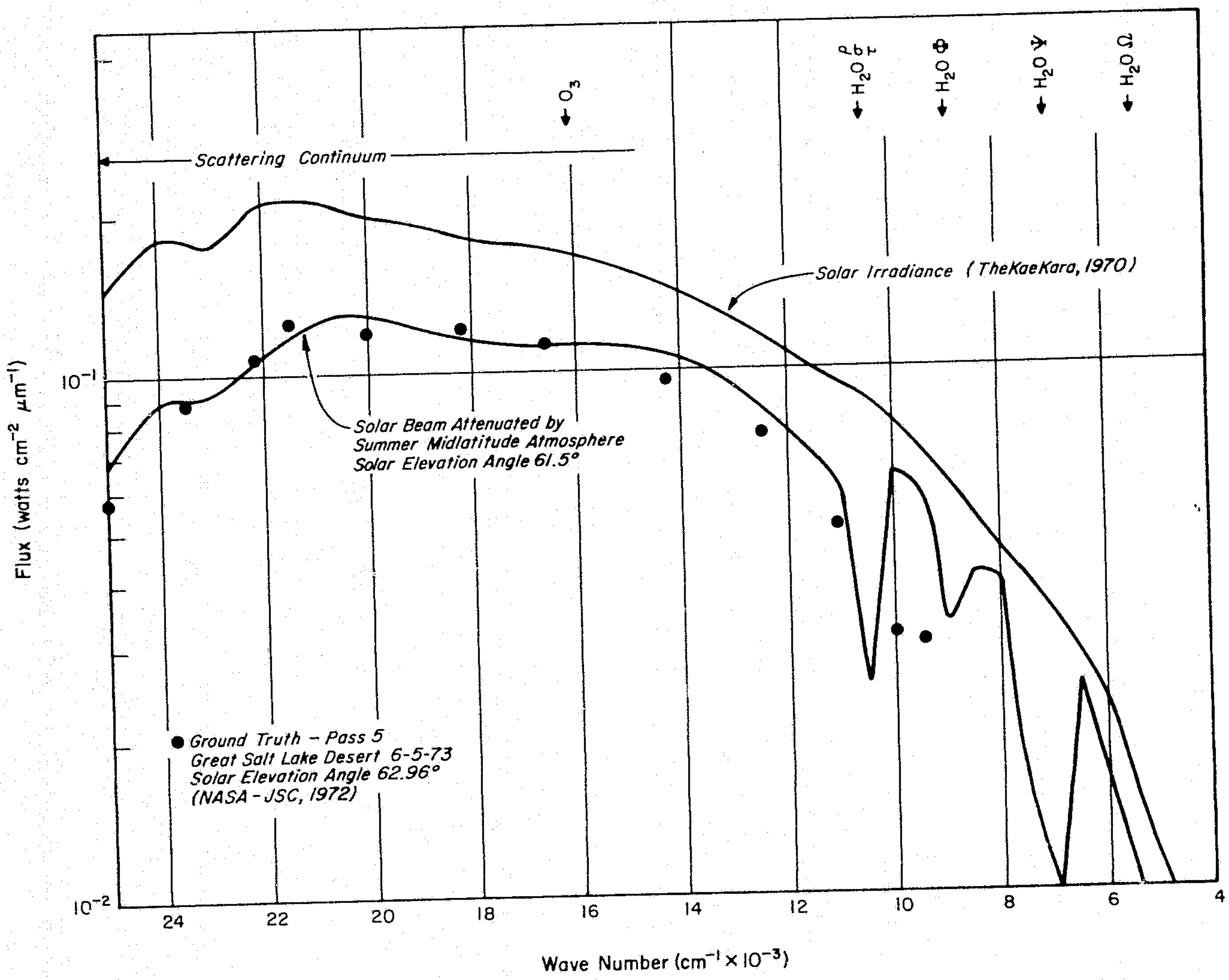

Figure 2.2 Atmospheric Effects on In-coming Solar Radiation

3. SIMULATION OF SKYLAB RADIANCES

A suitable technique was desired to simulate SKYLAB EREP radiances over selected target surfaces while taking into account the complicated atmospheric attenuation mechanisms in a relatively simple parameterized calculation. This tool could then be used to predict the degree of atmospheric effect over a wide range of surface and atmosphere models. For this purpose, a simple surface-atmosphere system was adopted (see Figure 3.1). The measured surface reflected solar radiation (sun at elevation angle Θo) at wavelength λ, $R_T(\lambda)$ [watts cm^{-2} μm^{-1} str^{-1}] will be dependent on: (1) the transmission properties of the atmosphere as defined by the total optical depth, τ^*; (2) the surface reflectance properties defined by the surface reflectance spectrum $r(\lambda)$; and (3) the spectral response function $\phi_i(\lambda)$ of the i^{th} EREP S192 band. In the simplified geometry illustrated the S192 sensor is considered to view nadir and therefore the angular dependence inherent in the conical scan sequence is not modeled. The solar irradiance, $I(\lambda)$, is taken from Thekaekara (1970) and modified by an appropriate factor to correct for variation from the mean solar distance. Since solar elevation angles are high for all EREP passes, the viewing geometry reduces azimuthal dependence to a minimum. The treatment of potential paths available to photons reaching the sensor from the surface-atmosphere system is limited to two sources: a direct surface reflected beam, R_s and a path radiance, R_a. The total measured radiance is the product of the sum of these source radiances and the sensor response as indicated in Figure 3.1.

3.1 The Direct Surface Reflected Component, R_s

The direct surface reflected radiance, R_s, is computed in the following manner. The available monochromatic solar flux (watts cm^{-2} μm^{-1}) at optical depth $\tau = 0$ for a sun at elevation angle Θo is given by: $I(\lambda)\sin\Theta o$. The attenuated solar flux at the surface after interaction with an atmosphere of optical depth τ^* is: $I(\lambda)\sin\Theta o \exp(-\tau^*/\sin\Theta o)$ or $I(\lambda)\sin\Theta o T_{\Theta o}(\lambda)$. The amount of energy reflected from the surface is determined by the surface reflectance spectrum, $r(\lambda)$. The amount of incident flux reflected from the surface is given by: $r(\lambda)I(\lambda)\sin\Theta o T_{\Theta o}(\lambda)$. Assuming Lambert reflectance (equal intensities in all upward directions), the intensity reflected to the sensor direction is: $r(\lambda)I(\lambda)\sin\Theta o T_{\Theta o}(\lambda)/\pi$ (watts $cm^{-2}\mu m^{-1}str^{-1}$).

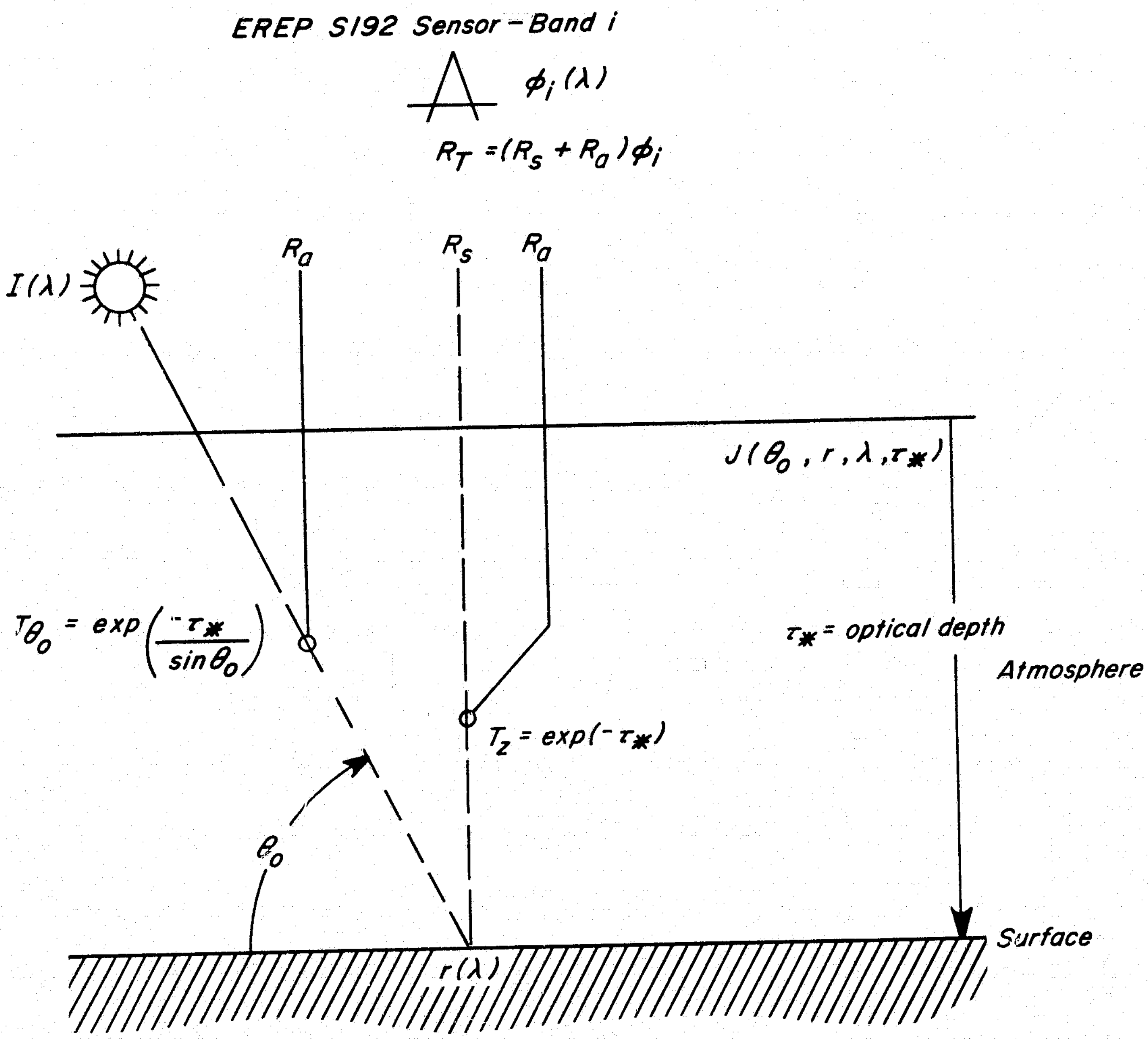

Figure 3.1 Schematic of Computation Geometry

507043

Finally, additional attenuation occurs as the beam exits the atmosphere by a factor: $T_z(\lambda) = \exp(-\tau^*)$. The monochromatic direct surface reflected beam at the sensor is therefore given by:

$$R_s(\lambda) = \frac{r(\lambda)I(\lambda)\sin\Theta o}{\pi} \exp(\frac{-\tau^*}{\sin\Theta o}) \exp(-\tau^*) \tag{3.1}$$

[The implicit assumption to neglect the surface incident diffuse solar radiation will introduce a small (∿ 10%) error in the shorter wavelength spectral regions which is compensated for by the path radiance term.]

Atmospheric transmissivities for the sun-target and target-sensor paths are calculated using the LOWTRAN 2 computer code (Selby and McClatchey, 1972). This program is designed to compute transmittances at low spectral resolution between 350 and 40000 cm^{-1}. Specifiable parameters include the model atmosphere (pressure, temperature, water vapor, ozone, and aerosol distributions), type of path traversed (such as that from surface to space at a given angle), and spectral resolution. A sample transmittance table is illustrated in Table 3.1 below. A resolution of 50 cm^{-1} was used for all calculations. The model atmosphere used to generate the table was a standard summer midlatitude case (LOWTRAN model atmosphere 2). In performing ground truth correlated EREP simulations, nearby radiosonde data of temperature and water vapor vertical distribution were employed. For all cases, the aerosol distribution corresponds to Deirmendjian's (1963) Haze Model C with a number density vertical distribution corresponding to the model of Elterman (1968, 1970) yielding a ground level visibility of approximately 23 km. In general, the accuracy of these computed transmissivities is on the order of 10% placing an identifiable limit to the accuracy of the simulated radiance values. The LOWTRAN 2 program was specially modified to compute transmissivities in the format required for this study in addition to performing calculations of independent absorber optical depths, total optical depth, and single scattering albedo as a function of optical depth.

3.2 The Atmosphere Reflected Component, R_a

This component of the sensor incident radiance is often called the "path" radiance and is essentially the intensity of the scattered (by molecules and aerosols) or diffuse solar radiation. As described in Section 2, a continuum due to scattering crosses the entire region of the EREP S192's

FREQ CM-1	WAVELENGTH MICRONS	TOTAL TRANS	H2O TRANS	CO2+ TRANS	OZONE TRANS	N2 CONT TRANS	H2O CONT TRANS	MOL SCAT TRANS	AEROSOL TRANS
19000	0.5263	0.6771	1.0000	1.0000	0.9824	1.0000	1.0000	0.8912	0.7733
19050	0.5249	0.6763	1.0000	1.0000	0.9830	1.0000	1.0000	0.8901	0.7728
19100	0.5236	0.6755	1.0000	1.0000	0.9837	1.0000	1.0000	0.8890	0.7724
19150	0.5222	0.6747	1.0000	1.0000	0.9843	1.0000	1.0000	0.8879	0.7719
19200	0.5208	0.6739	1.0000	1.0000	0.9849	1.0000	1.0000	0.8868	0.7715
19250	0.5195	0.6730	1.0000	1.0000	0.9855	1.0000	1.0000	0.8857	0.7711
19300	0.5181	0.6721	1.0000	1.0000	0.9860	1.0000	1.0000	0.8846	0.7706
19350	0.5168	0.6713	1.0000	1.0000	0.9866	1.0000	1.0000	0.8835	0.7702
19400	0.5155	0.6704	1.0000	1.0000	0.9871	1.0000	1.0000	0.8823	0.7697
19450	0.5141	0.6692	1.0000	1.0000	0.9873	1.0000	1.0000	0.8812	0.7693
19500	0.5128	0.6661	1.0000	1.0000	0.9874	1.0000	1.0000	0.8800	0.7688
19550	0.5115	0.6669	1.0000	1.0000	0.9876	1.0000	1.0000	0.8789	0.7684
19600	0.5102	0.6657	1.0000	1.0000	0.9877	1.0000	1.0000	0.8777	0.7680
19650	0.5089	0.6645	1.0000	1.0000	0.9878	1.0000	1.0000	0.8765	0.7675
19700	0.5076	0.6633	1.0000	1.0000	0.9878	1.0000	1.0000	0.8753	0.7671
19750	0.5063	0.6620	1.0000	1.0000	0.9879	1.0000	1.0000	0.8741	0.7666
19800	0.5051	0.6607	1.0000	1.0000	0.9879	1.0000	1.0000	0.8729	0.7662
19850	0.5038	0.6599	1.0000	1.0000	0.9886	1.0000	1.0000	0.8717	0.7657
19900	0.5025	0.6591	1.0000	1.0000	0.9893	1.0000	1.0000	0.8705	0.7653
19950	0.5013	0.6582	1.0000	1.0000	0.9900	1.0000	1.0000	0.8693	0.7649
20000	0.5000	0.6574	1.0000	1.0000	0.9907	1.0000	1.0000	0.8681	0.7644
20050	0.4988	0.6565	1.0000	1.0000	0.9913	1.0000	1.0000	0.8668	0.7640
20100	0.4975	0.6556	1.0000	1.0000	0.9920	1.0000	1.0000	0.8656	0.7636
20150	0.4963	0.6548	1.0000	1.0000	0.9927	1.0000	1.0000	0.8643	0.7631
20200	0.4950	0.6539	1.0000	1.0000	0.9934	1.0000	1.0000	0.8631	0.7627
20250	0.4938	0.6527	1.0000	1.0000	0.9936	1.0000	1.0000	0.8618	0.7622
20300	0.4926	0.6515	1.0000	1.0000	0.9938	1.0000	1.0000	0.8605	0.7618
20350	0.4914	0.6503	1.0000	1.0000	0.9940	1.0000	1.0000	0.8593	0.7614
20400	0.4902	0.6491	1.0000	1.0000	0.9943	1.0000	1.0000	0.8580	0.7609
20450	0.4890	0.6477	1.0000	1.0000	0.9942	1.0000	1.0000	0.8567	0.7605
20500	0.4878	0.6463	1.0000	1.0000	0.9941	1.0000	1.0000	0.8554	0.7601
20550	0.4866	0.6449	1.0000	1.0000	0.9940	1.0000	1.0000	0.8541	0.7596
20600	0.4854	0.6435	1.0000	1.0000	0.9939	1.0000	1.0000	0.8527	0.7592
20650	0.4843	0.6422	1.0000	1.0000	0.9941	1.0000	1.0000	0.8514	0.7588
20700	0.4831	0.6410	1.0000	1.0000	0.9943	1.0000	1.0000	0.8501	0.7583
20750	0.4819	0.6397	1.0000	1.0000	0.9945	1.0000	1.0000	0.8487	0.7579
20800	0.4808	0.6385	1.0000	1.0000	0.9947	1.0000	1.0000	0.8474	0.7575
20850	0.4796	0.6373	1.0000	1.0000	0.9951	1.0000	1.0000	0.8460	0.7570
20900	0.4785	0.6362	1.0000	1.0000	0.9955	1.0000	1.0000	0.8447	0.7566
20950	0.4773	0.6351	1.0000	1.0000	0.9959	1.0000	1.0000	0.8433	0.7562
21000	0.4762	0.6339	1.0000	1.0000	0.9963	1.0000	1.0000	0.8419	0.7557
21050	0.4751	0.6327	1.0000	1.0000	0.9966	1.0000	1.0000	0.8405	0.7553
21100	0.4739	0.6315	1.0000	1.0000	0.9969	1.0000	1.0000	0.8391	0.7549
21150	0.4728	0.6303	1.0000	1.0000	0.9972	1.0000	1.0000	0.8377	0.7544
21200	0.4717	0.6291	1.0000	1.0000	0.9975	1.0000	1.0000	0.8363	0.7540
21250	0.4706	0.6277	1.0000	1.0000	0.9977	1.0000	1.0000	0.8349	0.7536
21300	0.4695	0.6264	1.0000	1.0000	0.9978	1.0000	1.0000	0.8335	0.7532
21350	0.4684	0.6250	1.0000	1.0000	0.9979	1.0000	1.0000	0.8320	0.7527
21400	0.4673	0.6237	1.0000	1.0000	0.9981	1.0000	1.0000	0.8306	0.7523
21450	0.4662	0.6221	1.0000	1.0000	0.9979	1.0000	1.0000	0.8292	0.7519

Table 3.1 Sample LOWTRAN 2 (Selby and McClatchy, 1972) Computations Results using Summer Midlatitude Atmosphere with Visual Range of 23 km

spectral sensitivity being strongest in the shortwave visible (Rayleigh's scattering law) and dropping off into the near-IR where aerosols are the predominant scattering species. Solution of the radiative transfer equation for distributions of aerosols at individual wavelengths, and with varying vertical temperature and moisture structures is complex and time consuming. Additionally, the number of calculations required to simulate the twelve EREP S192 bands prompted adoption of a highly parameterized scheme.

In general, the significance of atmosphere scattered intensity components will be a function of geometry, wavelength, optical depth, and single scattering albedo. This last parameter is a measure of the importance of scattering (relative to absorption) as an attenuation mechanism (e.g. $0 \leq \omega o \leq 1.0$, $\omega o = 1.0$ complete scattering, $\omega o = 0.0$ complete absorption). The scattered intensity is directly proportional to the single scattering albedo. The magnitude of these intensities will be of greatest significance in spectral regions where $\omega o \rightarrow 1.0$ and $\tau^* > 1.0$. The EREP S192 spectral interval suggests a single scattering approximation since this condition is never fulfilled. The table below (Table 3.2) illustrates the point. In the near-infrared when the single scattering albedo is large (e.g. at 1.0 μm), the optical depth is very small. Conversely, a large optical depth (e.g. at 2.0 μm) is due almost entirely to molecular absorption and the scattered contribution is minimal. Even in the worse case, the short wavelength visible (e.g. at .40 μm), the optical depth is a respectible .65. (These values were calculated for the summer-midlatitude atmosphere described above.) Exact multiple scattering radiative transfer calculations at visible and near-IR wavelengths indicate that total surface-atmosphere reflected radiance will be a near linear function of surface reflectance (Malila and Nalepka, 1973). Since the direct surface reflected component varies linearly with surface reflectance, one expects the path radiance to exhibit complementary behavior. In fact, this result is exact if single scattering alone is considered. Based on the discussion above, the assumption of single scattering and, therefore, linear dependence on the surface reflectance appears valid for the spectral region under

Table 3.2 Characteristic values of Single Scattering Albedo and Optical Depth at three wavelengths

λ(μm)	$\nu(cm^{-1})$	ωo	τ^*
0.4	25000	1.00	.65
1.0	10000	.85	.07
2.0	5000	.02	1.00

discussion except for absorption regions. Based on these considerations, the following parameterization of the path radiance term is adopted:

An "atmospheric reflectance", J, is defined as the ratio of the outward path radiance and the incident solar radiance. Its dependence on single scattering albedo is modeled as a function of optical depth as described above, i.e.

$$J(\lambda, \Theta o, r, \omega o, \tau^*) \to J(\lambda, \Theta o, r, \tau^*)$$

For large optical depths, the single scattering albedo is assumed to be small and the path radiance negligible. For small optical depths, the single scattering albedo is presumed to be near unity and a linear dependence of path radiance on surface reflectance is computed. This dependence is also assumed in the visible region ($\lambda < 0.7$ μm) where scattering predominates. A smooth transition is assumed between these limits, the upper value being taken at $\tau^* = 0.4$ and the lower at $\tau^* = 0.1$.

$$J(\lambda, \Theta o, r, \tau^*) = \beta\{J(\lambda, \Theta o, 0, \tau^*) + r[J(\lambda, \Theta o, 1, \tau^*) - J(\lambda, \Theta o, 0, \tau^*)]\}$$

$$\text{where } \beta = \begin{cases} 1.0 & \tau^* < 0.1 \text{ or } \lambda < 0.7\ \mu\text{m} \\ \dfrac{0.4 - \tau^*}{.3} & \tau^* \le 0.4,\ \ge 0.1 \\ 0.0 & \tau^* > 0.4 \end{cases} \tag{3.2}$$

Values of $J(\lambda, r = 0.0)$ and $J(\lambda, r = 1.0)$ are interpolated in wavelength from exact radiative transfer calculations by Plass and Kattawar (1968) at .40 μm (25000 cm^{-1}), .70 μm (14286 cm^{-1}) and 1.67 μm (5988 cm^{-1}). Interpolation is not extended beyond the 1.67 μm data point. Calculations characterize the size and vertical distributions of Diermendjian and Elterman, respectively, referenced above. Outside of molecular absorption regions, wavelength interpolation is valid, as attenuation coefficients for both molecular and aerosol scattering are smooth functions of wavelength. The values for interpolation are obtained by subtracting the respective direct reflected component at each wavelength. Figure 3.2 demonstrates J values computed by Equation 3.2 for a midlatitude summer atmosphere. The values are generally valid for solar elevation angles greater than 50° since the exact calculations cited exhibit smooth dependence at high solar elevation angles.

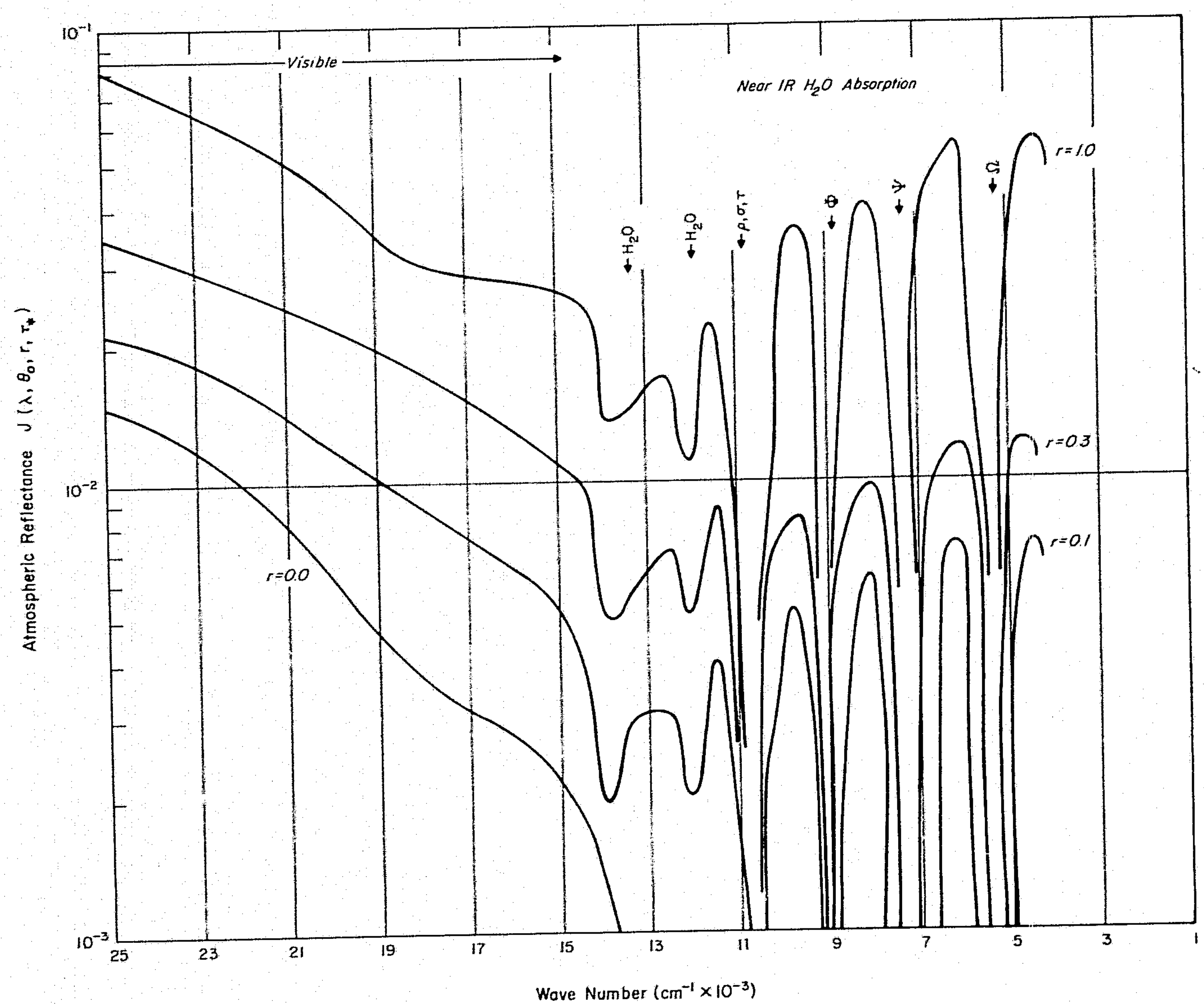

Figure 3.2 J-value (Atmospheric Reflectance) for a Midlatitude Summer Atmosphere

The atmosphere reflected component, R_a, is the product of the atmospheric reflectance defined above (Eq. 3.2) and the incident solar intensity $I(\lambda)/\pi$:

$$R_a = \frac{I(\lambda)}{\pi} J(\lambda, \Theta o, r, \tau^*) \qquad (3.3)$$

3.3 Total Band-Weighted Radiance

The total monochromatic sensor incident radiance is given by the sum of the direct surface reflected component, R_s and the path radiance, R_a given by equations 3.1 and 3.3, respectively, i.e.:

$$R_T(\lambda) = \frac{I(\lambda)}{\pi} \left[r(\lambda)T_{\Theta o}(\lambda)T_z(\lambda)\sin\Theta o + J(\lambda, \Theta o, r, \tau^*)\right] \qquad (3.4)$$

Monochromatic radiances, $R_T(\lambda)$, computed above must be band pass weighted to simulate EREP S192 data. At each wavelength the product of the monochromatic radiance and the band pass response function for the i^{th} EREP S192 band is formed. Integrating in wavelength over limits of the i^{th} band yields the weighted radiance:

$$R_T(i) = \frac{\int_{\Delta\lambda i} R_T(\lambda)\phi_i(\lambda)d\lambda}{\int_{\Delta\lambda i} \phi_i(\lambda)d\lambda} \qquad (3.5)$$

where $\phi_i(\lambda)$ is the spectral response function of the i^{th} EREP S192 band [NASA-JSC, 1973] and $\Delta\lambda_i$ is the wavelength interval of non-zero response in the i^{th} band, and is therefore the inferral of the integration.

In this report the monochromatic expression (3.4) will be used for data comparison while band-weighted calculations (3.5) will be reported as theoretical results. In the following sections (4 and 5) SKYLAB EREP S192 data will be used to verify the validity of the model.

4. ANALYSIS OF SKYLAB DATA

Data from the SKYLAB EREP instruments sensing in the visible, near-infrared, and thermal infrared was obtained to assist in carrying out this study. Imagery from the S190A Multispectral Photographic Camera and S190B Earth Terrain Camera were utilized primarily to document the areal homogeneity of surface targets and to provide real time base maps upon which to portray sensor scan lines, aircraft ground truth data locations, and surface ground truth targets. Information potentially obtainable from the S191 Infrared Spectrometer long wavelength (LWL) data (6.6 - 16 μm) was to have been used to deduce ground truth data of the atmospheric structure over selected test sites. However, instrumental problems encountered degraded that segment of the required data such that inference of atmospheric vertical structure was not deemed feasible. Of significant impact in this regard was the incidence of off-band radiation contamination in strongly absorbing regions. Ideally, atmospheric vertical structure (i.e. temperature-water vapor profiles) should be obtainable by inverting radiance measurements in the 6-7 μm water vapor and 14-15 μm carbon dioxide absorbing regions. The stability and accuracy of inversion procedures, however, are extremely sensitive to noisy data. A statement describing "S191 Thermal Infrared Radiance Accuracies" (NASA-JSC, TF 6-74-10-38; November 1974) states that in profiling spectral regions, radiance accuracies are "uncertain enough to frustrate attempts at inversion for atmospheric profiles". Based on these assessments, it was decided to substitute nearby conventional radiosonde profiles for S191 remotely-sensed inversions. It is believed that any potential accuracy advantage of simultaneous inversion over conventional sounding is cancelled by the cited noise problem.

The primary source of SKYLAB EREP data for this study has been the S192 Multispectral Scanner (MSS). This instrument provided measurements in twelve bands in the visible and near-infrared regions corresponding to those wavelengths most widely utilized in earth resource monitoring applications. The MSS data available in the form of computer compatible tapes of calibrated aperture radiances provides measured spectra of solar radiation reflected from the earth-atmosphere system. A primary task of this study is to evaluate the effect of the atmosphere in these measurements.

4.1 EREP Sensor Summary

A considerable amount of data, both in imagery format and computer compatible digital tapes, was received in order to carry out this study. The following subsections catalog the data received and analyzed.

4.1.1 S190A Imagery

Pass	Magazine	Frame	Description
2	01/02	113/120	1 ea. Pos/1 ea. neg.
	03/04	129/126	
	05/06	113/120	
5	07/12	001/010	1 ea. Pos/1 ea. neg.
20	25/26	186/189	1 ea. Pos/1 ea. neg.
	28/30	186/189	
37	37/38	140/150	1 ea. Pos/1 ea. neg.
	39/40	140/150	1 ea. Pos
	41/42	140/150	1 ea. Pos/1 ea. neg.
39	37/38	196/205	
	39/40	196/205	(Same)
	41/42	195/205	
43	37/38	329/335	
	39/40	329/335	(Same)
	41/42	329/335	
45	43/44	052/058	
	45/46	052/058	(Same)
	47/48	052/058	

4.1.2 S190B Imagery

Pass	Magazine	Frame	Description
5	81	001/014	1 each Pos.
20	85	002/005	1 each Pos.
37	86	321/333	1 each Pos.
39	88	010/017	1 each Pos.
43	87	110/116	1 each Pos.
45	88	093/101	1 each Pos.

4.1.3 S191 Digital Tapes

These data were received in two batches: (a) initial processing (I) received prior to a letter of 23 April 1974 describing problems in both SWL and LWL data; (b) reprocessed data (R) received in second go-round.

Pass	Output Tape No.	Remark (I or R)
2	909166/909167	I
	909344/909345	I
	926534/926535	R
5	906332/906333	I
	926488/926489	R
12	906225/906/226	I
	916219/916220	R
20	906367/906368	I
	917747/917751	R
37	906400/906401	I
	916694/916695	R
	918136/918137	R
39	906402/906403	I
	916689/916617	R
43	907217/907219	I
	916692/916693	R
94	922754/922955	R

4.1.4 S192 Digital Tapes

Pass	Output Tape No.	SDO's
2	921002/921003	All
	932866/932867	1-14, 17-20, 22
5	920042/920043	All
	920044/920045	
	921006/921007	
39	934524	15, 16, 21
	934525	15, 16, 21
	934526	15, 16, 21
	934828/934831	All
43	932720/932721	All

4.2 EREP Test Site Documentation

Validation of atmospheric models and simulated radiance computations is to be achieved by comparison with actual EREP S192 measurements within the context of a "controlled" experiment. By this is meant documentation of as many of the variables as possible which enter into the simulation calculations. Potentially, these include such measurable ground truth elements as surface reflectance and atmospheric structure to be correlated with S192 MSS data at the time of overpass. Based on the availability of ground truth and screening of S190 imagery two specific test sites were selected. These areas were (1) Salton Sea-Sonoran Desert (Site #547119) and (2) Great Salt Lake-Salt Lake Desert (Site #547220). Each of these sites provided the following desirable characteristics:

(a) ease of site acquisition from spacecraft altitudes

(b) topographical uniformity within definable limits

(c) a high response (reflectivity) target

(d) a nearby low response (reflectivity) target

(e) relative surface areal homogeneity within the target surface

(f) ground truth and/or correlative aircraft data

Test site surface characteristics were documented in the following manner:

Base maps were prepared to appropriate scale from S190B Earth Terrain imagery. Overlays were prepared to scale which delineate the surface distribution of minerological species and regions of relatively uniform topography. Minerological information was extracted from available appropriate USGS, state, and local maps. A geological analysis was prepared for each site to explain the map overlays and discuss surface minerology and morphology. These exhibits were prepared to help choose the surface spectral reflectance curves within the EREP S192 MSS bands appropriate to the given surface.

Concurrent S192 MSS data for each test site was located by viewing appropriate screening film products [Product No. S055-2] of individual MSS channels. Based on the screening film, specific GMT segments of digital S192 MSS data [Product No. S051-3] were ordered. These correspond to EREP passes 2 and 43 for site #547119 and 5 and 39 for site #547220. Data ordered is cataloged below:

<u>EREP Pass 2 (2 June 1973)</u>

GMT Time Interval: 200822.0 - 200828.0 GMT
Location: 33.5 N, 116.0 W (Salton Sea)
Channels: 2, 3, 4, 5, 6, 7, 8, 9, 10, 11, 12

<u>EREP Pass 5 (5 June 1973)</u>

1. Segment A

GMT Time Interval: 175737.0 - 175742.0 GMT
Location: 40.7 N, 113.8 W (Bonneville Salt Flat)
Channels: 2, 3, 4, 5, 6, 7, 8, 9, 10, 11, 12

2. Segment B

GMT Time Interval: 175810.0 - 175814.0 GMT
Location: 39.3 N, 11.4 W (Wasach Range)
Channels: 2, 3, 4, 5, 6, 7, 8, 9, 10, 11, 12

EREP Pass 39 (13 September 1973)

1. Segment A

GMT Time Interval: 193404.3 - 193407.0 GMT
Location: 40.7 N, 113.8 W (Bonneville Salt Flat)
Channels: 2, 3, 4, 5, 6, 7, 8, 9, 10, 11, 12

2. Segment B

GMT Time Interval: 193421.7 - 193424.2 GMT
Location: 41.25 N, 112.6 W (Great Salt Lake)
Channels: 2, 3, 4, 5, 6, 7, 8, 9, 10, 11, 12

3. Segment C

GMT Time Interval: 193416.8 - 193418.9 GMT
Location: 41.1 N, 113.0 W (Desert)
Channels: 2, 3, 4, 5, 6, 7, 8, 9, 10, 11, 12

EREP Pass 43 (15 September 1973)

1. Segment A

GMT Time Interval: 180504.7 - 180505.9 GMT
Location: 33.3 N, 115.9 W (Salton Sea)
Channels: 2, 3, 4, 5, 6, 7, 8, 9, 10, 11, 12

2. Segment B

GMT Time Interval: 180501.5 - 180503.7 GMT
Location: 33.2 N, 116.1 W (Desert)
Channels: 2, 3, 4, 5, 6, 7, 8, 9, 10, 11, 12

In selecting these digital segments account was taken of the S192 instrument's circular scan mode, specifying start and stop GMT's based on the correlating time scale on the screening film product. A base map overlay of the corresponding S192 field-of-view was prepared for each pass using the GMT correlated latitude/longitude grid points of the scan line center and two end points. Special techniques were developed to identify and calibrate S192 digital data pixels (Section 4.3).

4.2.1 Bonneville Salt Flat-Salt Lake Desert (Site No. 547220)

Location of EREP S192 data segments selected from the Bonneville Salt Flat-Salt Lake Desert are portrayed in Figure 4.1. The instrument field-of-view for EREP passes 5 (SL2) and 39 (SL3) is delineated by plotting the locus of right most (R), left most (L), and center (C) scan pixels against a base map (scale ∿ 1:1,000,000) prepared from consecutive S190B frames (Pass 39, Roll 88, Frames 021/013). Four specific surface target pixel subsets

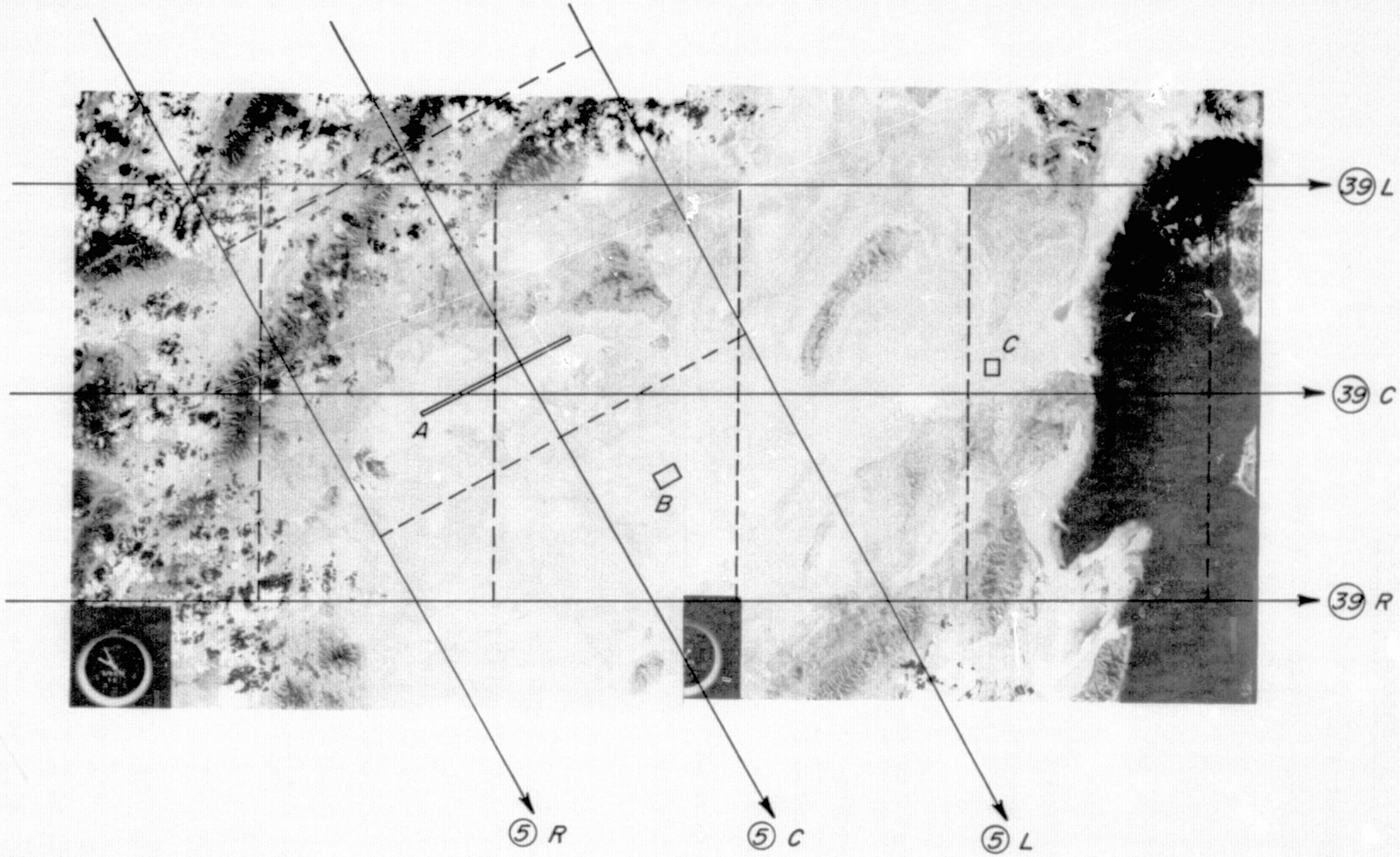

Site A - Bonneville Salt Flats
Pass 5 No. 920042
Scan Line 533-537
Pixel 235-734

Site B - Salt Lake Desert - Ground Truth
Pass 5 No. 921006
Scan Line 360-390
Pixel 770-829

Site C - Salt Lake Desert
Pass 39 No. 934829
Scan Line 80-100
Pixel 582-602

Site D - Great Salt Lake
Pass 39 No. 934829
Scan Line 400-403
Pixel 375-610

L - Left Most Pixel

C - Center Pixel

R - Right Most Pixel

Figure 4.1 Location of S192 Data Segements over the Salt Flat - Salt Lake Desert are designated as sites A, B, C, D, respectively. These sites were isolated using the binary slicing technique described in the following section and have the following properties:

Site	Pass #	Surface Target	GMT	S192CCT	Solar Elevation	Remarks
A	5	Salt Flat	156:17:57:40.6	920042	62.65	High response target
B	5	Desert	156:17:57:45.0	921006	62.96	Ground truth collected
C	39	Desert	256:19:34:20.7	934829	52.57	High response target
D	39	Salt Lake	256:19:34:23.9	934829	52.45	Low response target

Three surface types (salt flat, desert, water surface) are represented within this set and concurrent ground truth exists for site B. The character of the surface targets selected has been investigated by a literature search of relevant geological information. The Bonneville Salt Flats of northwestern Utah lie in the central western portion of the Great Salt Lake Desert which extends to the western edge of the Great Salt Lake. Like most of the salt flats around the Lake, they are composed of lake bed sediments with a good deal of clay and high salt content. Trench-like salt evaporators form a pattern of curves and rectangles in the center of the Bonneville Salt Flats as a means of extracting potash. The main geological features outside of the Desert itself, are the Wasatch National Forest and Cedar Mountains on its eastern side, the Desert Range in the west, the Pilot Range in the northwest, and the Hogup and Promentory Mountains to the north. Finally, northeast of the Desert, lies the Great Salt Lake bordered by salt flats, the remnant of a larger ancient lake. The Great Salt Lake Desert and the area immediately surrounding the Great Salt Lake share a fairly level terrain ranging from about 3,000 to 5,000 feet above sea level. The mountainous areas tend to have an elevation of approximately 7,000 to 10,000 feet (Figure 4.2). The mineralogy of the region is considerably homogeneous; mostly salty lake bed sediments (Figure 4.3). The lake bed sediments of the Desert and salt flats contain a significant amount of clay and have very high salt content. Immediately surrounding the Desert, the sediments contain clay or rust and enough salt to prohibit agriculture. Sand dunes are scattered through a few parts of the Desert. Some spots among the salt

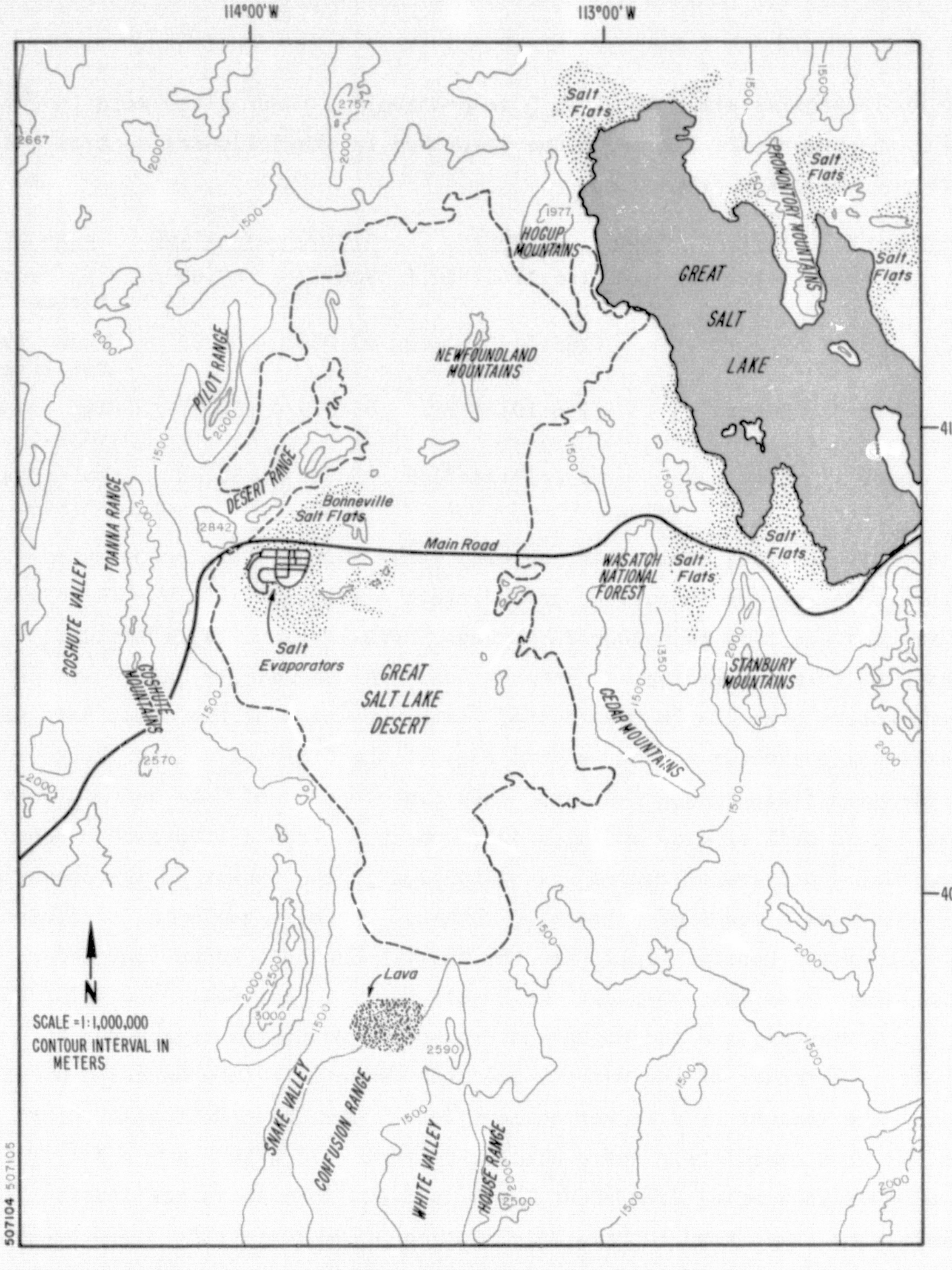

Figure 4.2 Topography of the Great Salt Lake Target Area

flats and an area south of the Salt Lake are marshlands. Mostly colluvium and alluvium surround the Cedar Mountains and the Pilot and Desert Ranges. A mineral analysis of the Bonneville Salt Flats and Great Salt Lake Desert shows a large quantity of clay and calcite and a number of salts: .66% calcium, .89% magnesium, 1.67% potassium, 2.74% sulfur and, the prime components, 35.65% sodium and 58.39% chlorine as given in weight percents (personal communication, Geology Department, University of Utah). The region of the Bonneville Salt Flats and Great Salt Lake Desert has a relatively level terrain and uniform composition characterized by a great deal of salt and clay.

Surface reflectances are difficult to characterize based on a knowledge of surface minerology alone. For this reason recent ground truth measurements were used in model calculations when possible. Figure 4.4 demonstrates three surface reflectance curves typical to sites B, C, D. Curve 1 is concurrent with EREP pass 5 for site B [NASA, JSC, (1972) - MSC-05531]. Curve 2 corresponds to the same site some months later (EREP pass 39) and demonstrates a "wet" desert reflectance [NASA, JSC, (1974) - MSC-05537]. Curve 3 is the spectral reflectance of an "inland water body" extracted from the literature (Krinov, 1947). These data will be used to evaluate model calculated synthetic EREP radiances.

4.2.2 Salton Sea-Sonoran Desert (Site No. 547119)

Figure 4.5 demonstrates location of the S192 data segment selected in the Salton Sea region. Since line straightened data was correlated with the left (L) pixel GMT, segments ordered on the basis of the non-straightened data (taking account of the instrument's circular scan mode) were effectively shifted back along the ground track. Therefore, our digital data for pass 43 did not reach the Salton Sea as expected. Site E was selected in a region of homogeneous alluvium as close to the originally intended area as possible. The base map was prepared to a scale of approximately 1:250,000 from an S190B frame (Pass 43, Roll 87, Frame 112). Digital data is selected from pass 43, output tape #932720. The GMT is approximately 258:18:05:02.7 with a solar elevation angle of 52.49°.

On the whole, the region of the Salton Trench is a homogeneous one of nonmarine sand, silt, and clay with a relatively level terrain.

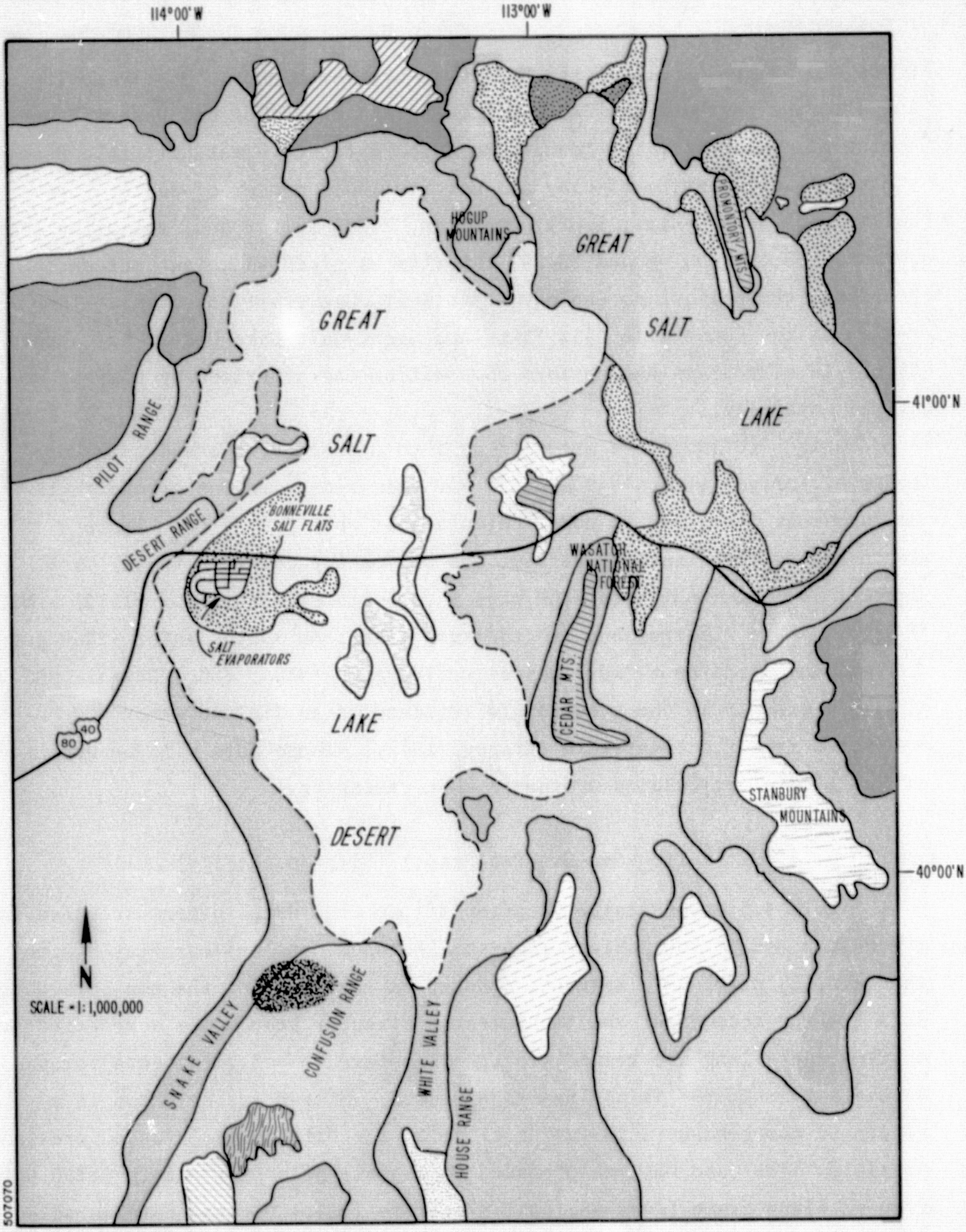

Figure 4.3 Mineralogy of the Great Salt Lake Target Area

Legend for Mineralogical Map of the Bonneville Salt Flats Area

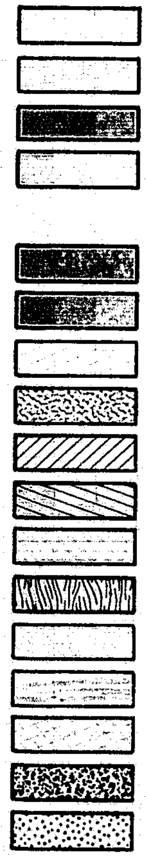

lake bed sediments, mostly clay, high salt content
dunes, colitic, silicious, gypsiferous
alluvial surfaces
lake bed sediments, enough salt to prohibit agriculture, clay or rust
marshland, mostly fresh water
colluvium and alluvium
rhyolite
quartzite, schist, dolomite
quartzite, schist, limestone
quartzite, limestone, dolomite, sandstone, shale
shaley limestone, dolomite, silty sandstone, gypsum
dolomite, silty dolomite, chert
dark grey limestone, shaley limestone
quartzite - relatively pure, sandstone, some conglomerate
lake shore features, gravelly and sandy
lava
salt flats

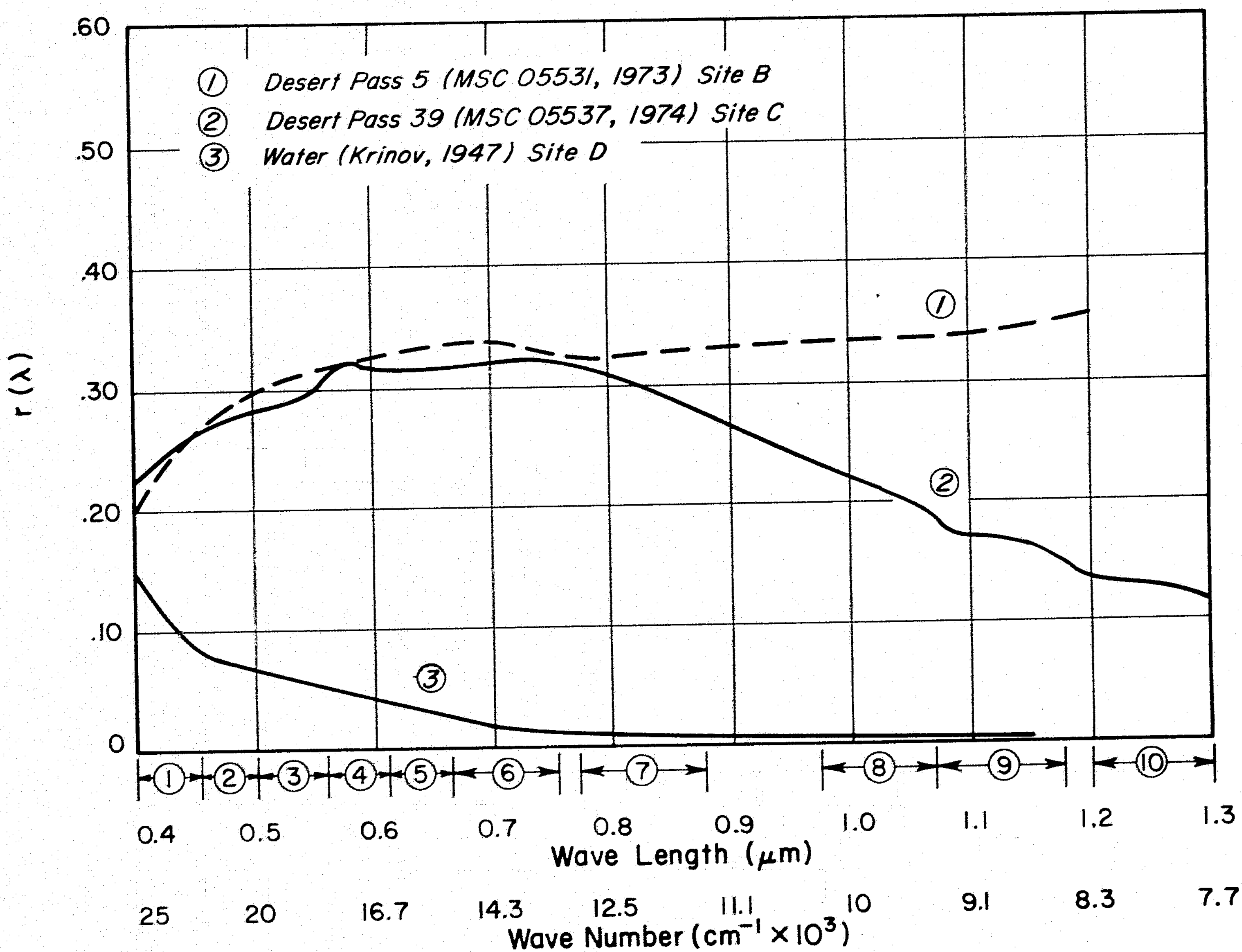

Figure 4.4 "Ground Truth", Surface Reflectance Curves Typical for Deserts and Water.

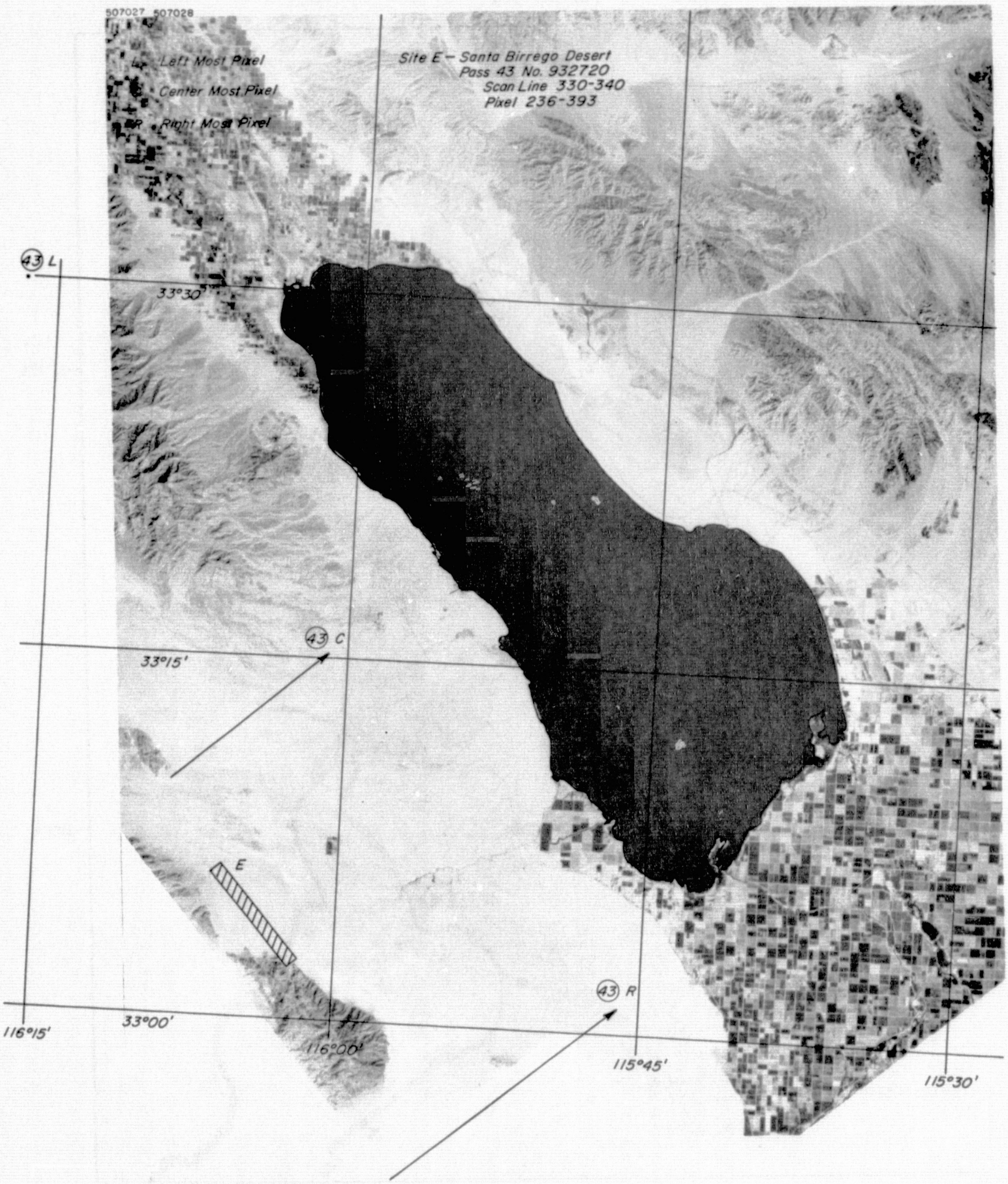

Figure 4.5 Location of the S192 Data Segement over the Salton Sea Region

ORIGINAL PAGE IS OF POOR QUALITY

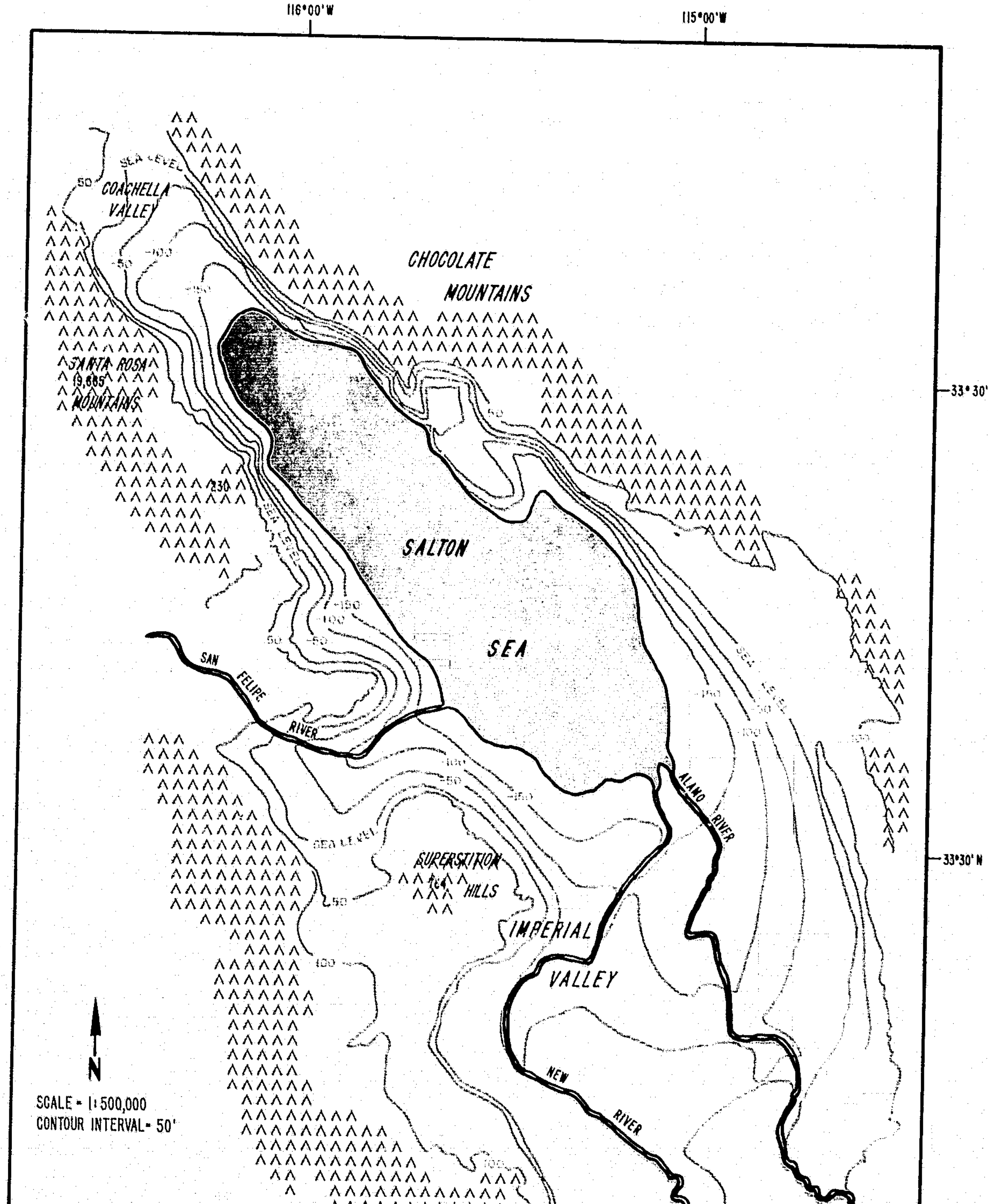

Figure 4.6 Topography of the Salton Sea Target Area

The 35-mile long Salton Sea, all that remains of a broader ancient lake, lies in Southern California's Imperial Coachella Valley which occupies the elongate Salton Trough that extends northwest from the Gulf of California. The trough is fairly uniform in elevation and composition (Figure 4.6).

Fairly uniform elevation of about 100 to 200 feet below sea level characterize the surface encircling the sea. The valley approaches sea level at the foot of the Chocolate Mountains and the Superstition Hills. Only here do the contour lines begin to become complex.

The major geological features in or around the valley (Figure 4.7) include cultivated fields of the southeast, the Superstition Hills in the south, the Santa Borrego Desert in the southwest, the Santa Rosa Mountains in the west. The cultivated fields are cut by two rivers: the Alamo and the New River. The Salton Creek flows from the northeast and the San Felipe from the southwest. A number of faults run through the area, notably the southern part of the San Andreas which is nearly lost beneath the sediments of the Salton Trench.

Immediately surrounding the almost kidney-shaped Salton Sea are quaternary lake deposits of claystone, sand and beach gravel, and silt on the west side. Proceeding further from the sea's banks, there is a great deal of alluvium including peat interbedding the alluvial sand, silt, and clay on the west side.

4.3 Technique for Handling EREP S192 Digital Data

It was desired to formulate an efficient method to ground-correlate selected EREP S192 data segments from within the instrument's gross field-of-view. S192 data was supplied in the form of channel counts accompanied by corresponding calibration equations to convert to engineering units. In handling computer compatible tapes (CCT's), it was not economically feasible to perform digital-to-radiance conversions for entire ordered GMT segments (see Section 4.2) due to the high data rate of the instrument. Therefore, a pre-selection procedure based on analysis of channel counts was employed. For a given surface target site (Sites A-E above), calibrated radiances were obtained in the following manner:

(a) Digital counts were read from the appropriate CCT (listed by number for each site in Section 4.2) corresponding to the relevant GMT time interval which includes the desired test site pixels for a preselected S192

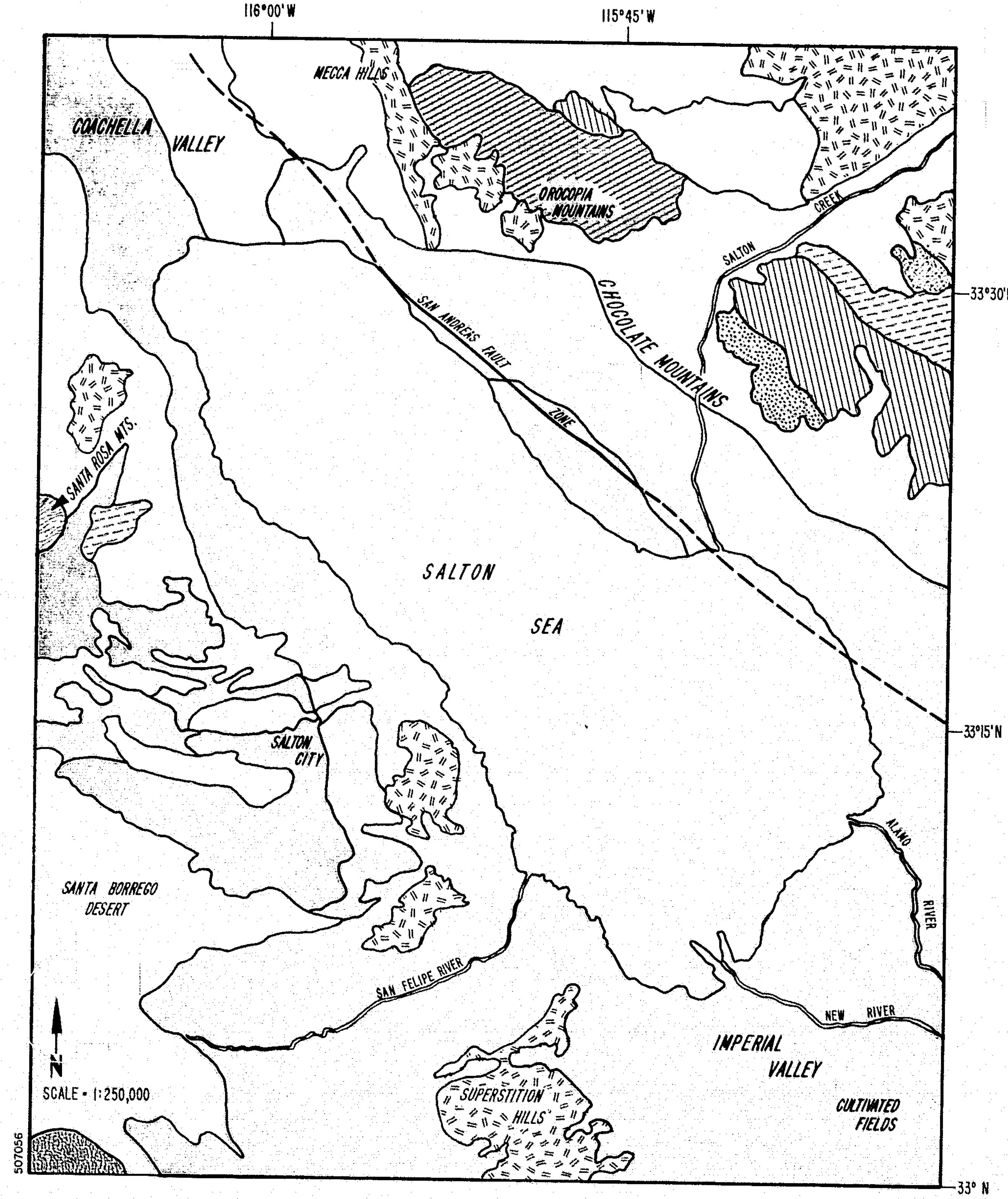

Figure 4.7 Mineralogy of the Salton Sea Target Area

Legend for Mineralogical Map of the Salton Sea Area

recent alluvium-alluvial sand, silt, clay, and gravel, including interbedded peat on west side, some older alluvium, recent flood plain silt and clay of the Colorado River

quaternary lake deposits-claystone, sand and beach gravel, silt on west side

quaternary nonmarine terrace deposits-local stream terrace deposits

tertiary lake deposits - tan gray clay, shales, and low grade sandstone, interbedded siltstone on west side

tertiary volcanic-rhyolite, andesite, basalt, pyroclasts

pleistocene nonmarine sedimentary deposits - older alluvium and fanglomerate, red gray clay, sandstone, and pebble gravel, some boulder gravel on west side

pliocene pleistocene nonmarine - conglomerate, schist, breccia, arkose, siltstone, sandstone and red claystone on west side

undivided pliocene nonmarine sedimentary rocks - pink gray laminated sandstone, and red clay on west side, grayish red to yellowish brown basal conglomerate, overlain by yellowish gray arkose and arkose conglomerate, shale on west side

undivided miocene nonmarine - reddish brown arkose sandstone, conglomerate, and sedimentary breccia

oligocene nonmarine sediment - conal sandstone, breccia, mudstone, evaporate rocks, siltstone and claystone on west side

mesozoic granitic - undifferentiated granite

precenozoic granite and metamorphic - foliated migmatites, including schist and quartz diorite bodies

precretaceous metasedimentary - quartzite schist with thick beds of gypsum and anhydrite

igneous metamorphic complex

andesitic basalt intrusive

channel (SDO). The choice of SDO (1-22) was subjectively based on S190A multispectral imagery and/or S192 screening film products to correspond to that spectral interval which provided the required image contrast to delineate surface features with which to ground correlate the digital data. This choice will in general depend on surface type.

(b) A threshold value, D_t, was selected within the interval $0 \leq D_t \leq 255$ to facilitate a binary slicing of the individual raw data counts, $D_{p,s}(i)$, to form an image of the field-of-view, $I_{p,s}(i)$, according to the condition:

$$\begin{aligned} D_{p,s}(i) \leq D_t, \quad I_{p,s}(i) = 0 \\ D_{p,s}(i) > D_t, \quad I_{p,s}(i) = 1 \end{aligned} \qquad (4.1)$$

where $D_{p,s}(i)$ is the digital value at scan line s and pixel p and $I_{p,s}(i)$ is the reconstructed image matrix for the chosen SDO. Operationally, a hard copy image is printed by assigning a decimal point to all non-zero image elements.

(c) The scan line-pixel correlated image produces a means of locating specific surface target pixels within the instrument field-of-view by recognition of available readily identifiable surface features. Once accomplished, calibrated radiances for each of the required channels can be computed using the appropriate conversion equation of the form:

$$R_{p,s}(n) = A_{o,n} + D_{p,s}(n)A_{1,n} \qquad (4.2)$$

where R(n) is the radiance (engineering units) in the n^{th} S192 channel, D(n) is the raw digital count, and $A_{o,n}, A_{1,n}$ are calibration constants provided on each CCT.

The procedure outlined above has been found to be extremely efficient. Typically a GMT time segment of $\sim$ 7 seconds yields $\sim 10^7$ raw digital values. By employing the intermediary binary slicing technique for one SDO, conversion calculations need be performed for only $\sim 10^2$-10^3 pixels. This represents a considerable savings in computation time.

Table 4.1 below summarizes the parameters used in retrieving S192 radiances for the selected sites (the figure number refers to the image matrix corresponding to each site).

Table 4.1 EREP S192 Digital Data Segments for Selected Surface Target Sites

Site	EREP Pass #	S192 Output Tape #	Figure #	SDO/Band	D_t	Scan lines (s field)	Pixels (p field)
A	5	920042	4.7	19/8	250	533/547	235/734
B	5	921006	4.12	19/8	150	360/390	770/829
C	39	934829	4.16	4/4	100	80/100	582/602
D	39	934829	4.16	4/4	100	400/403	375/610
E	43	932720	4.21	19/8	100	330/340	236/393

Examples of S192 digital data products are given in the Appendix. For each selected site, the following are given:

(a) an image matrix for the appropriate GMT correlated CCT using parameters given in Table 4.1.

(b) ephemeris data as a function of scan line within the instrument field-of-view given by the image matrix.

(c) conversion equations for each site by SDO provided on the appropriate CCT.

(d) a sample of radiance data in engineering units (watts cm^{-2} μm^{-1} str^{-1}) corresponding to the selected site for each S192 band. (Table 4.2 provides an SDO/Band conversion chart. Output is generated by SDO, but results are plotted by band.)

Table 4.2 Channel/SDO-Band

$R_{p,s}(i)$	$R_{p,s}(n)$
i = 1	n = 22
2	18
3	1, 2
4	3, 4
5	5, 6
6	7, 8
7	9, 10
8	19
9	20
10	17
11	11, 12
12	13, 14

In plotting S192 radiances in the following sections, data will be referenced to site, scan line, and pixel. These data elements may be located within the field-of-view by referring to the appropriate figure designated in Table 4.1 and/or utilizing the given ephemeris data.

5. COMPARISION OF DATA WITH MODEL CALCULATIONS

Calibrated radiances for the twelve SKYLAB EREP S192 bands have been extracted from available data tapes using the technique described above (Section 4.3) for the cited test site areas (Section 4.2). These measurements are compared with simulated EREP radiances calculated using the model described in Section 3. For each test site a mean value is determined for each EREP S192 band by a simple averaging of the calibrated pixel radiances corresponding to the given surface target. Additionally, high and low values within each site are selected to characterized the variability of the data. Thus, for each site, the plotted radiances for the i^{th} band are:

$$R_{max}(i) = \max[R_{p,s}(i)]$$

$$\overline{R}\ (i) = [(p_2 - p_1 + 1)(s_2 - s_1 + 1)]^{-1} \sum_{p=p_1}^{p_2} \sum_{s=s_1}^{s_2} R_{p,s}(i)$$

$$R_{min}(i) = \min[R_{p,s}(i)] \qquad (5.1)$$

where $R\ p,s\ (i)$ = calibrated radiance for the i^{th} EREP S192 band for pixel p and scanline s (given by image matrix coordinates).

(p_1, p_2) = initial and final pixels in target surface.

(s_1, s_2) = initial and final scan lines in target surface.

max, (min) = operation of taking maximum (minimum) absolute value.

Radiances are plotted at the response weighted mean wave number (centroid) for each band [see Equation 2.1] and upper and lower band limits as defined in Figure 2.1 are indicated.

Model calculations are performed using Equation (3.4) to produce monochromatic reflected radiances. In each case, atmospheric temperatures and humidity profiles from nearby radiosonde ascents and solar elevation angle are input to the atmospheric transmittance programs. Path radiance is approximated as described in Section 3.2. The necessary surface reflectance spectrum is available only for site B. For other cases, calculations are performed for a set of surfaces with constant reflectance characterizing the site target surface as given in Figure 4.4. Since only a finite variety of surface types (i.e. desert or water) were examined, this generalization is deemed acceptable. The results of these comparisons are summarized in Figures 5.1-5.4.

In Figure 5.1 EREP S192 digital data for bands 3, 7, 8, 9, 10, 11, and 12 are compared with a model calculation based on (Eq. 3.4). Bands 1, 2, 4, 5, and 6 were saturated during this GMT interval, and so, no data is available. However, the respective saturation levels in these bands fall below the radiances predicted by the model, indicating a degree of consistency. Since the ground truth surface reflectance spectrum was not measured beyond 1.3 μm (7700 cm^{-1}), meaningful comparisons are not possible using bands 11 and 12. Examining the fit of the simulated spectrum to the remaining EREP bands indicates the following:

(a) Mean pixel values lie within $\pm$ 3.5% of the calculated model values in bands 8 and 10 consistent with model accuracy.

(b) If data variability is considered, bands 3 and 7 will be within 10% of the calculated value consistent with model accuracy.

(c) In band 9, the mean pixel radiance is overestimated by the model (~ 28%), however, the $\pm$ 10% error bars on the calculation bring it to within 3% of the data value.

Based on this comparison it may be concluded that the data is generally consistent with the adopted model to within the accuracies inherent in the model and in the data analysis. The correlation between model and data is certainly very good.

Although simultaneous ground truth is not available for other test sites, the general trends indicated by the site B comparison are confirmed. Characteristic surface spectra (see Fig. 4.4) may be used to compare the model calculations to data in other sites.

Figure 5.2 examines site C, a desert region near the Great Salt Lake (see Fig. 4.1). Data was collected for EREP pass 39. Curve 2 in Figure 4.4 indicates that calculations at r = 0.2, 0.4 should bracket the data points. This behavior is satisfied. Qualitatively, we expect the reflectances manifested by the data to increase from bands 1 through 4 and then decrease into the rear IR. Although this behavior is indicated, the magnitude of the effect in bands 1, 2, and 3 is questionable, where data values appear to be low for consistency with the surface reflectance curves in Fig. 4.4.

This discrepancy is confirmed in Figure 5.3 for test site D over the Great Salt Lake. This site provides a test of the model over a low response target where earlier studies (Fraser, 1973) have suggested that atmospheric effect will be most pronounced. The true surface reflectance curve will

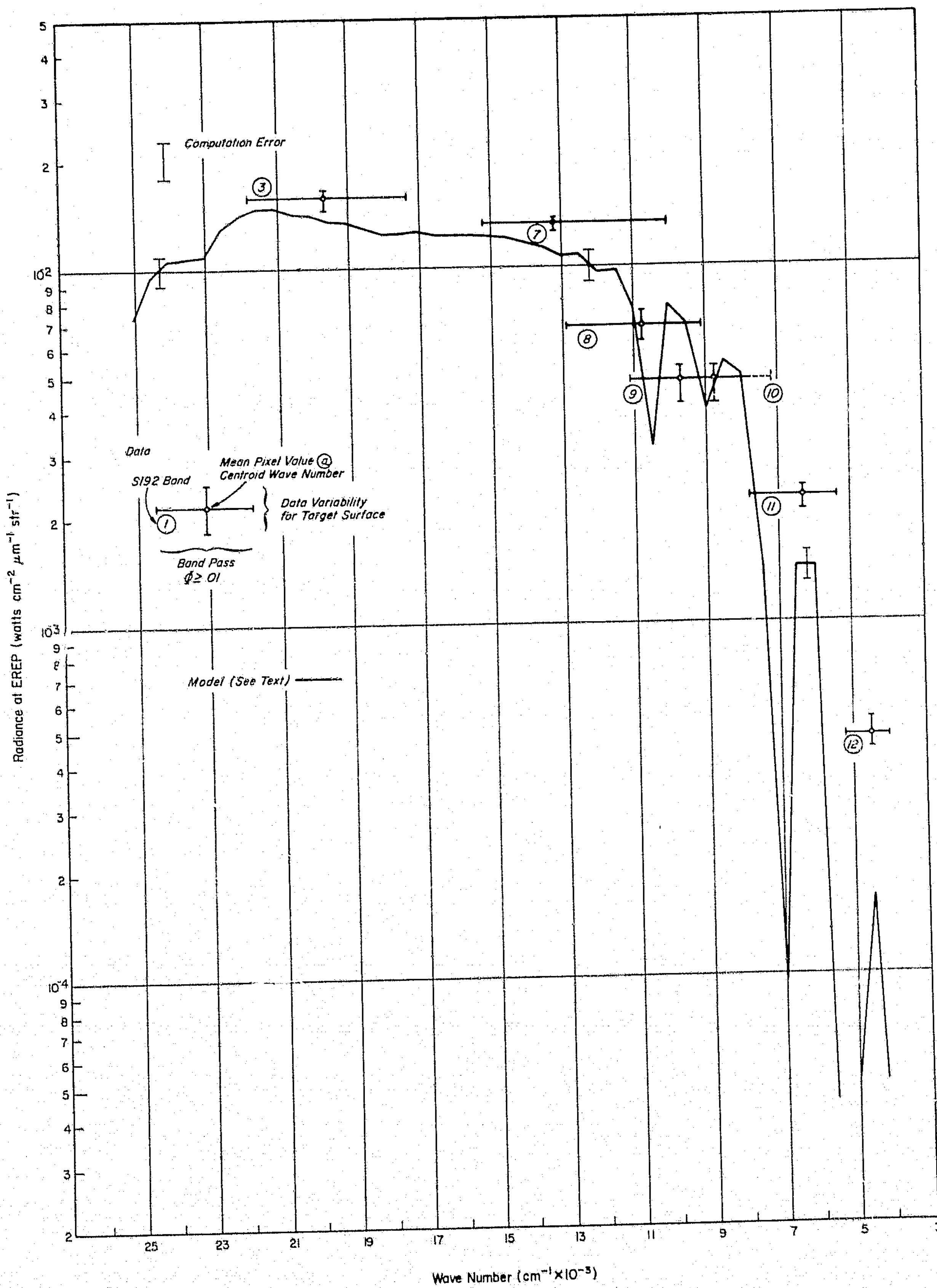

Figure 5.1 Model Computations Comparison with EREP Bands at Site B

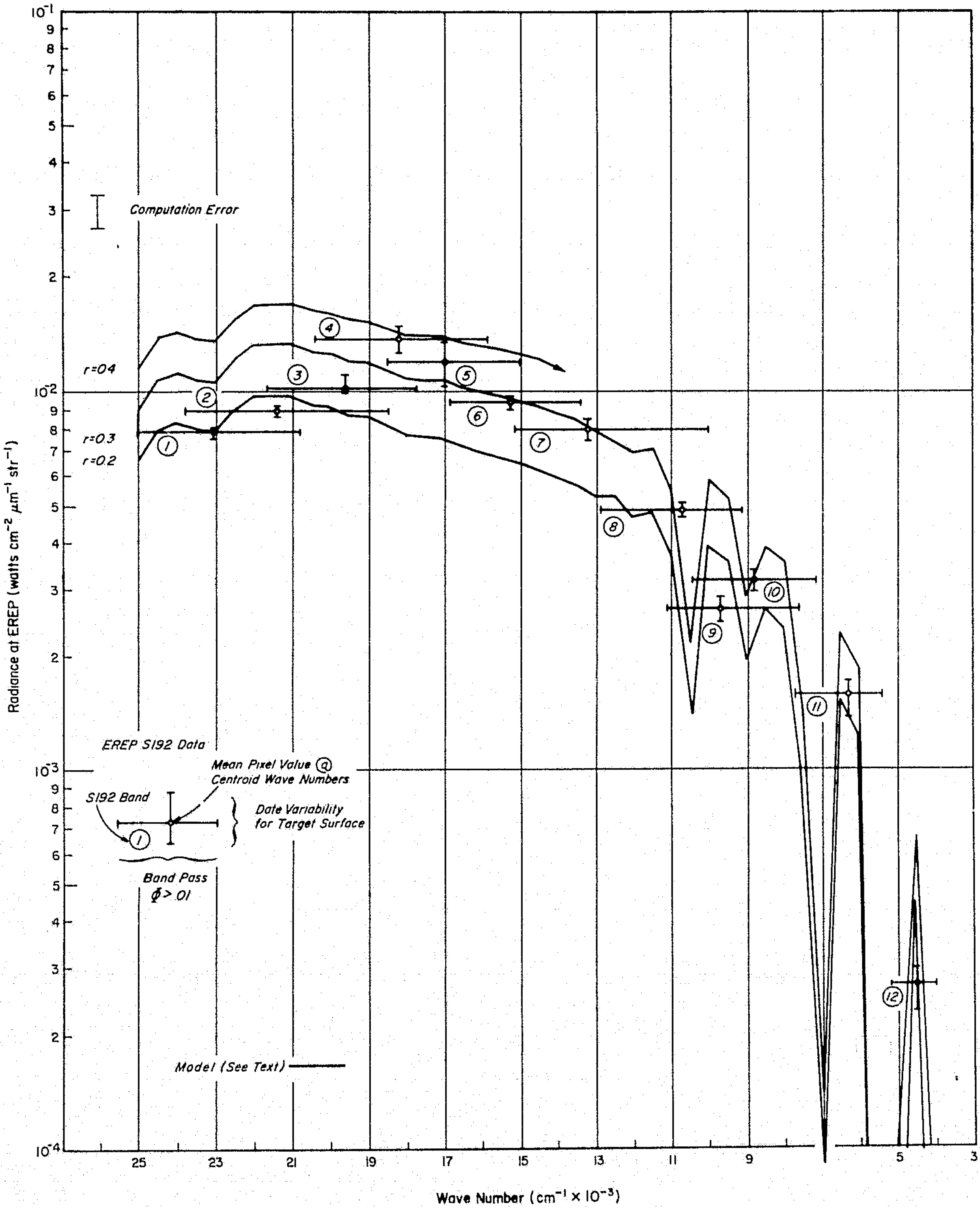

Figure 5.2 Comparisons for Site "C" near the Great Salt Lake

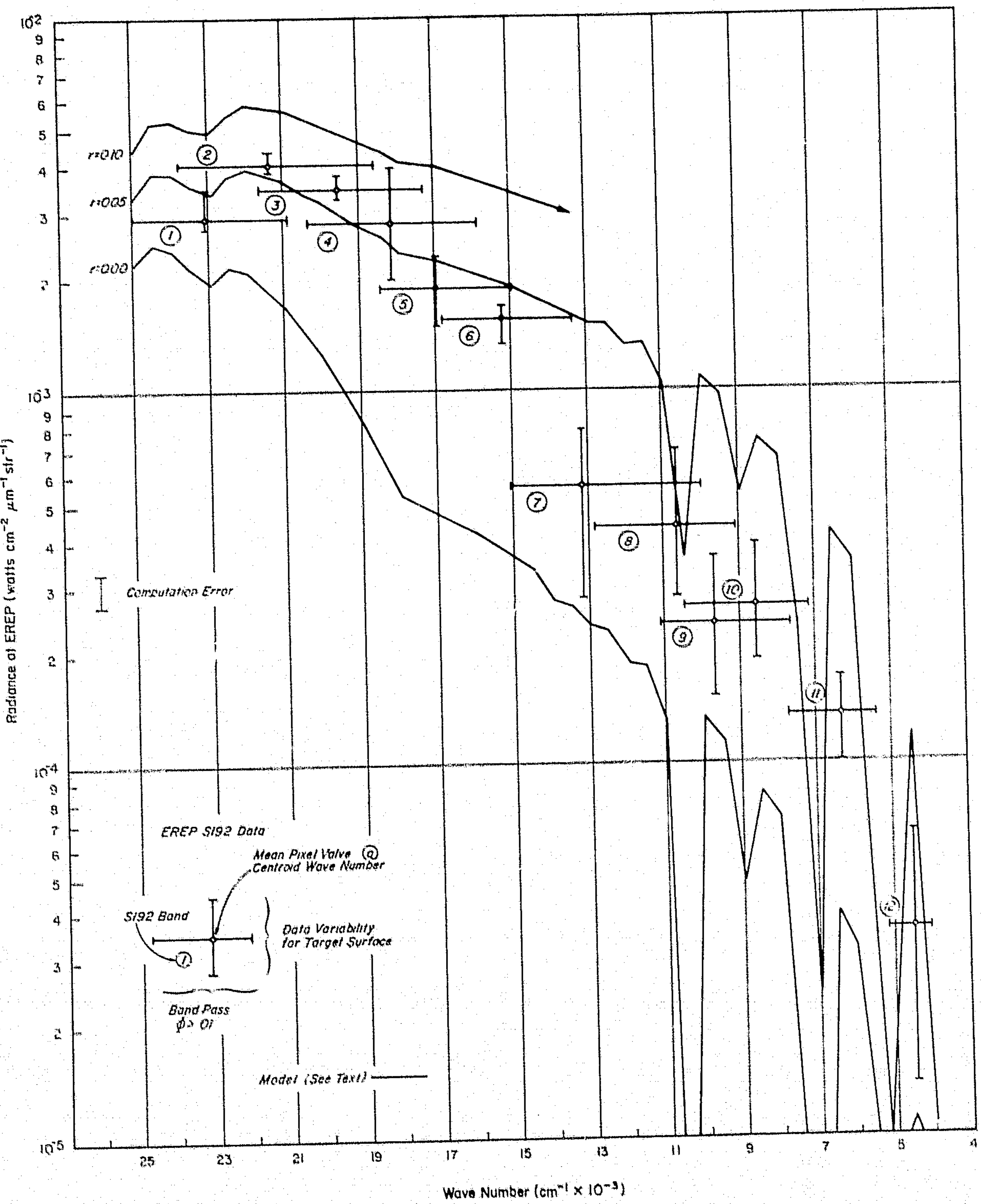

Figure 5.3   Comparisons for Site "D" over the Great Salt Lake

approximate that given by Krinov (1947)) (See Fig. 4.4) for an inland water body. Surface reflectance will be less than 0.05 for bands 4-12 and near the 0.00 curve for the near IR where water absorbs significantly. Reflectances greater than 0.05 are expected only in bands 1, 2, and 3. Again, these bands fall below the expected radiance levels while the others are consistent with the model as allowed by calculation error and data variability.

The essential features discussed are confirmed in Fig. 5.4. Bands 1, 2, and 3 values appear to anomolous compared with 4-12. These latter values are at least consistent with the desert surface reflectance spectra typified in 6.4, although it appears to be generally brighter. Based on examination of the set of figures 5.1 - 5.4, the ability of the model to simulate EREP S192 band radiances may be summarized in the following way:

(1) Radiances are seriously overestimated in bands 1, 2, and 3 if the calibrated radiances are valid. However, "EREP Sensor Performance Report Vol. III, S192" [NASA - JSC, 1974] indicates that prelaunch lamp values in these bands are lower than those derived from lunar and ground truth calibrations. This is confirmed in these comparisons. Therefore, the calibrated radiance data should be larger in magnitude in these bands and more consistent with the model.

(2) Fit for the low response target (site D) appears satisfactory. However, the variability of the data may mask inaccuracies. Examining the set of figures 5.1-4 further, it is noted that the variability of the data is an important factor in determining the fit of the model, particularly for the low response target. In

(3) Although simultaneous ground truth is available only for site B, EREP pass 5, Figures 5.1-5.4 indicate a healthy comparison between EREP S192 calibrated digital radiance values and model simulated spectra calculated as described in Section 3 of this report.

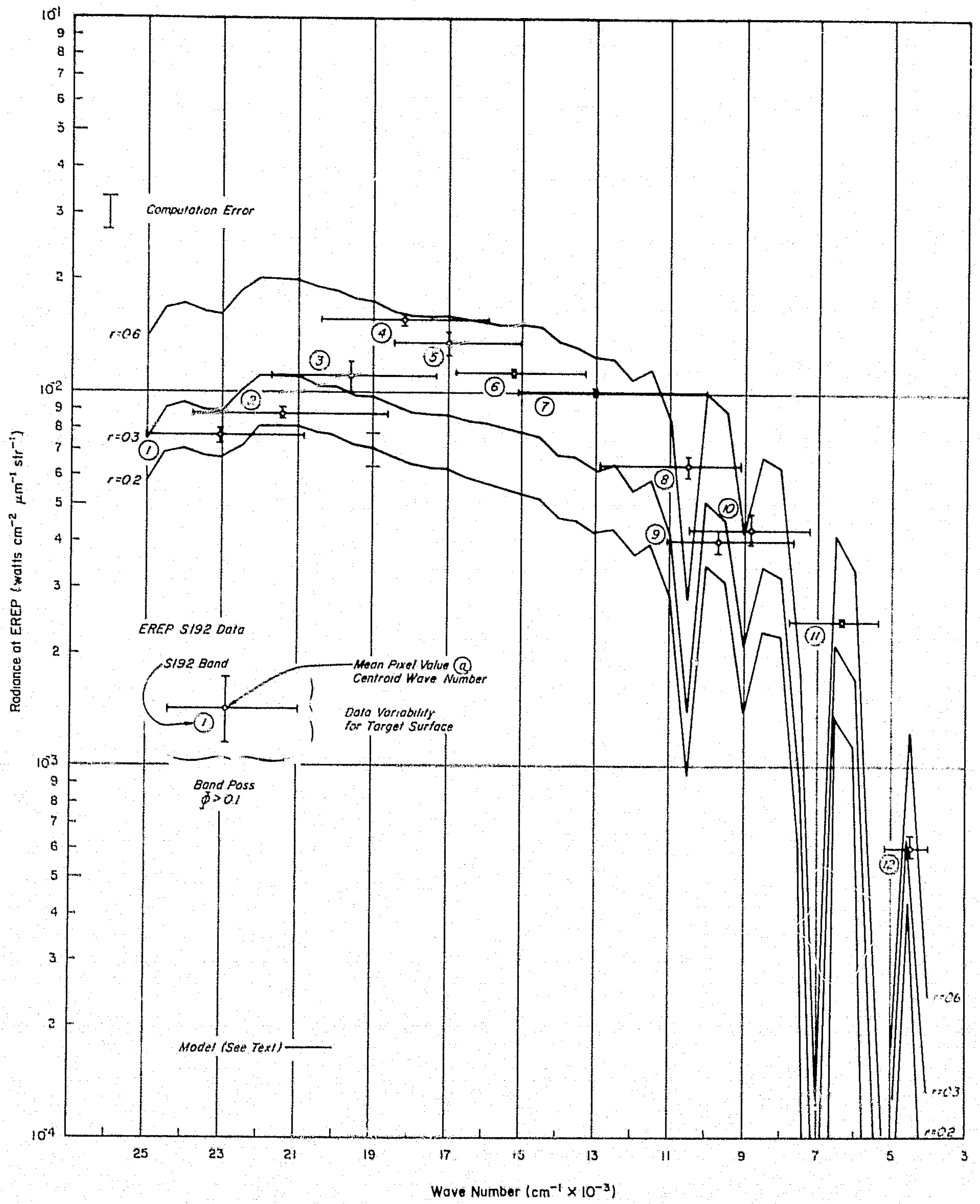

Figure 5.4 Comparisons for Site "E" Near Salton Sea

6. ATMOSPHERIC ATTENUATION IN SKYLAB DATA

The model described in Section 3 and examined experimentally in Section 5 may be used to simulate EREP S192 band radiances for various model atmospheres and surface reflectance types. A primary objective of this study is to quantitatively define the magnitude of possible atmospheric attenuation effects in remote sensing of earth resources using this sensor and therefore, a suitable definition of atmospheric effect is required.

Monitoring of earth resources requires that an inherent property of the surface be identifiable in a one-to-one manner from the reflected solar radiation in a particular MSS band. The physics of the problem indicates that this property should be the surface spectral reflectivity, $r(\lambda)$, but as Eq. 3.4 indicates, a space-based radiance measurement will not be simply proportional to the surface reflectance. The space-based sensor responds not only to the radiant energy reflected by the target surface, but also to the radiative processes of the atmosphere within its field-of-view. Not only will the magnitude of the surface reflectance determined from a radiance measurement in a single MSS band differ considerably from the true value, but ratioing radiances between adjacent bands will not remove the effects since atmospheric gases absorb, emit, and scatter solar radiation in a spectrally structured manner. This discussion of atmospheric effects will define three fundamental parameters: (a) the equivalent change in surface reflectance, Δr_*; (b) the contrast modification ratio, ΔC; and (c) the band ratio modification, $\Delta_q(i, j)$. The first two effects are definable with a given band, i, while the last pertains to interband (i vs. j) effects.

6.1 "Atmosphereless" Calculations

Fundamentally, simulation of space-sensor incident aperture radiances will not provide an indication of the effect of the atmosphere unless a suitable calibration radiance spectrum is introduced. This calibration continuum should be characteristic of available reflected intensities from the target surface without the modifying effect of the intervening atmosphere. Once defined, the difference between the simulated measured spectrum and the hypothetical atmosphereless spectrum will provide a quantitative determination of the atmospheric effect at a given wavelength or within a particular MSS band.

5-8

5-8

Examining Eq. 3.4, as the atmosphere becomes more spectrally transparent (i.e. $\tau^* \to 0.0$), the total measured radiance approaches the limit:

$$R_*(\lambda) = \lim_{\tau^* \to 0.0} R_T(\lambda) \to \frac{r(\lambda)\sin\theta o I(\lambda)}{\pi} \tag{6.1}$$

This defines the "atmosphereless" radiance which is simply proportional to the available solar radiation and the surface reflectance. Integrated over MSS band i, this quantity is (in analogy to Eq. 3.5):

$$R_*(i) = \frac{\int_{\Delta\lambda i} R_*(\lambda)\phi_i(\lambda)d\lambda}{\int_{\Delta\lambda i}\phi_i(\lambda)d\lambda} \tag{6.2}$$

6.2 Equivalent Change in Surface Reflectance, Δr_*

Although it may be desirable to determine the magnitude of the surface reflectivity $r(\lambda)$ from a space-based sensor, the atmosphere will in general alter the emergent beam as indicated in Section 2. A quantitative measure of this effect is given by the difference between the simulated measured radiance, R_T, and the atmosphereless radiance defined above:

$$\Delta R_*(\lambda) = R_T(\lambda) - R_*(\lambda) = \tag{6.3}$$

$$\frac{I(\lambda)}{\pi}\left[r(\lambda)\sin\theta o(T_z T_{\theta o} - 1.0) + J(\lambda, \theta o, r, \tau^*)\right]$$

Depending upon the particular properties of the atmosphere, this quantity may assume positive, negative, or zero values as a function of wavelength. Since by definition $T_z T_\theta \leq 1.0$, the first term within the brackets is at most zero and usually negative. In absorbing regions, where transmissivities are small, the atmosphereless radiance may be larger than the measured radiance, $\Delta R_* < 0.0$. Conversely, since J is positive definite, in scattering regions and/or where surface reflectivity is low, path radiance may be the dominant contribution (i.e. $\Delta R_* > 0.0$). In spectral regions where scattering is the primary extinction mechanism, a decrease in transmissivity may be compensated for by a like increase in path radiance so that the atmospheric effect is minimal (i.e. $\Delta R_* \sim 0.0$).

A particularly useful parameter is the equivalent change in surface reflectance corresponding to the radiance change defined by Eq. 6.2. The equivalent reflectance, r_T, corresponding to a simulated radiance, R_T will be given by:

$$r_T(\lambda) = \frac{\pi R_T}{I(\lambda)\sin\theta o} \qquad (6.4)$$

By Eqs. 6.1 and 6.3 above this reduces to:

$$r_T(\lambda) = r(\lambda) + \frac{\pi \Delta R^*}{I(\lambda)\sin\theta o} = r(\lambda) + \Delta r_*(\lambda) \qquad (6.5)$$

This expression defines the equivalent change of surface reflectance, $\Delta r_*(\lambda)$. This quantity is the increase (decrease) in surface reflectivity necessary with no atmosphere present to yield a radiance value equivalent to that measured. A positive (negative) value of Δr_* corresponds to a measured radiance of greater (lesser) magnitude than would be measured if no atmosphere were present. In analogy to Eq. 3.5, the equivalent change in surface reflectance may be averaged for the i^{th} S192 EREP band.

6.3 Contrast Modification Ratio, ΔC.

The inherent contrast between two surface types with different reflectance properties within a given spectral region may be altered by the atmosphere. The inherent contrast between surface reflectivities r_1 and r_2 in band i is given by:

$$C_*(i, r_1, r_2) = \frac{R_*(i, r_1) - R_*(i, r_2)}{R_*(i, r_2)} = \frac{r_1 - r_2}{r_2} \qquad (6.6)$$

The apparent contrast from space will be given by the corresponding radiance ratio:

$$C_T(i, r_1, r_2) = \frac{R_T(i, r_1) - R_T(i, r_2)}{R_T(i, r_2)} \qquad (6.7)$$

A normalized measure of the atmospheric effect in altering scene contrast is the contrast modification ratio:

$$\Delta C(i, r_1, r_2) = C_T(i, r_1, r_2)/C_*(i, r_1, r_2) \qquad (6.8)$$

As indicated by the expressions above, both absorption and scattering may modify the inherent contrast, as well as the individual surface type reflectivities.

6.4 Band Ratio Modification, Δq.

Ratioing MSS bands is a common means of differentiating between surface types. Indeed, if no atmosphere were present, the ratio of radiances in bands i and j would be directly proportional to the ratio of surface reflectances in these bands:

$$q_*(i, j) = \text{const}(i, j) \frac{r(i)}{r(j)} \tag{6.9}$$

where the constant is simple the ratio of available solar fluxes [= I(i)/ I(j)]. This quantity would provide a considerable amount of information regarding the surface spectral type.

However, the corresponding ratio of space-based radiances is in general modified by the atmosphere:

$$q_T(i, j) = \frac{R_T(i)}{R_T(j)} = \text{const}(i, j) \left\{\frac{r(i)\sin\theta o T_z(i)T_\theta(i) + J(i)}{r(j)\sin\theta o T_z(j)T_\theta(j) + J(j)}\right\} \tag{6.10}$$

A normalized measure of the modification of the interband ratio will be given by the quotient of these expressions:

$$\Delta q(i, j) = \frac{q_T(i, j)}{q_*(i, j)} = \frac{T_z(i)T_\theta(i) + J(i)/r(i)\sin\theta o}{T_z(j)T_\theta(j) + J(j)/r(j)\sin\theta o} \tag{6.11}$$

As the atmospheric effect approaches zero ($\tau_* \to 0.0$), the band ratio modification Δ approaches unity. Note that even target surfaces with constant surface spectral properties [i.e. r(i) = r(j)] will yield values of Δq differing from this limiting value due to the spectral nature of atmospheric transmissivity.

7. DISCUSSION OF COMPUTATION RESULTS

Calculations were performed for a set of atmospheric models corresponding to the test sites denoted in Section 4 in addition to standard models for summer and winter midlatitude atmospheres with respective integrated water vapor amounts of 2.40 gcm^{-2} and 0.90 gcm^{-2}. Each atmosphere contained an "average" amount of continental [Deirmendjian 1963] aerosol. Computations are valid for high solar elevation angles as is the case of most SKYLAB EREP passes. The atmospheric attenuation quantities defined in Section 6 were computed in addition to simulated EREP S192 radiances.

7.1 Magnitude of Atmospheric Effect

Figure 7-1 demonstrates simulated S192 radiance spectra computed by Equation 3.5 and atmosphereless radiances defined by Equation 6.2 for surfaces with constant reflectances of r = 0.1, 0.5, and 1.0 in each of the twelve EREP bands. Curves are piecewise connected between bands for clarity. The values of $R_T(i)$ calculated represent both spectral and magnitude modifications of the incident solar radiation. (For comparison, each of the R* curves is proportional to the weighted incident solar spectrum in each band.) Within a given band, i, the magnitude of the measured radiance is a strong function of the surface reflectance, r.

For these calculations, note that the simulated measured radiances are lower than the atmosphereless values, indicating negative values of equivalent surface reflectance (Equation 6.5). In comparing between bands, curvature modifications are introduced by selective, spectially dependent atmospheric effects. For example, there is a change of slope in bands 1, 2, and 3 due to enhanced scattering toward the blue (shorter wavelength) end of the spectrum. This is especially evident for the lowest surface reflectance value (r = 0.1) where path radiance is proportionally large. Large path radiance contributions (see Figure 3-2) increase the measured energy in these channels above the expected attenuated solar continuum. Similarly, the effect of atmospheric water vapor absorption is apparent in the near IR EREP S192 bands, particularly band 8, where a significant absorption feature can be seen, appreciably reducing the measured intensity.

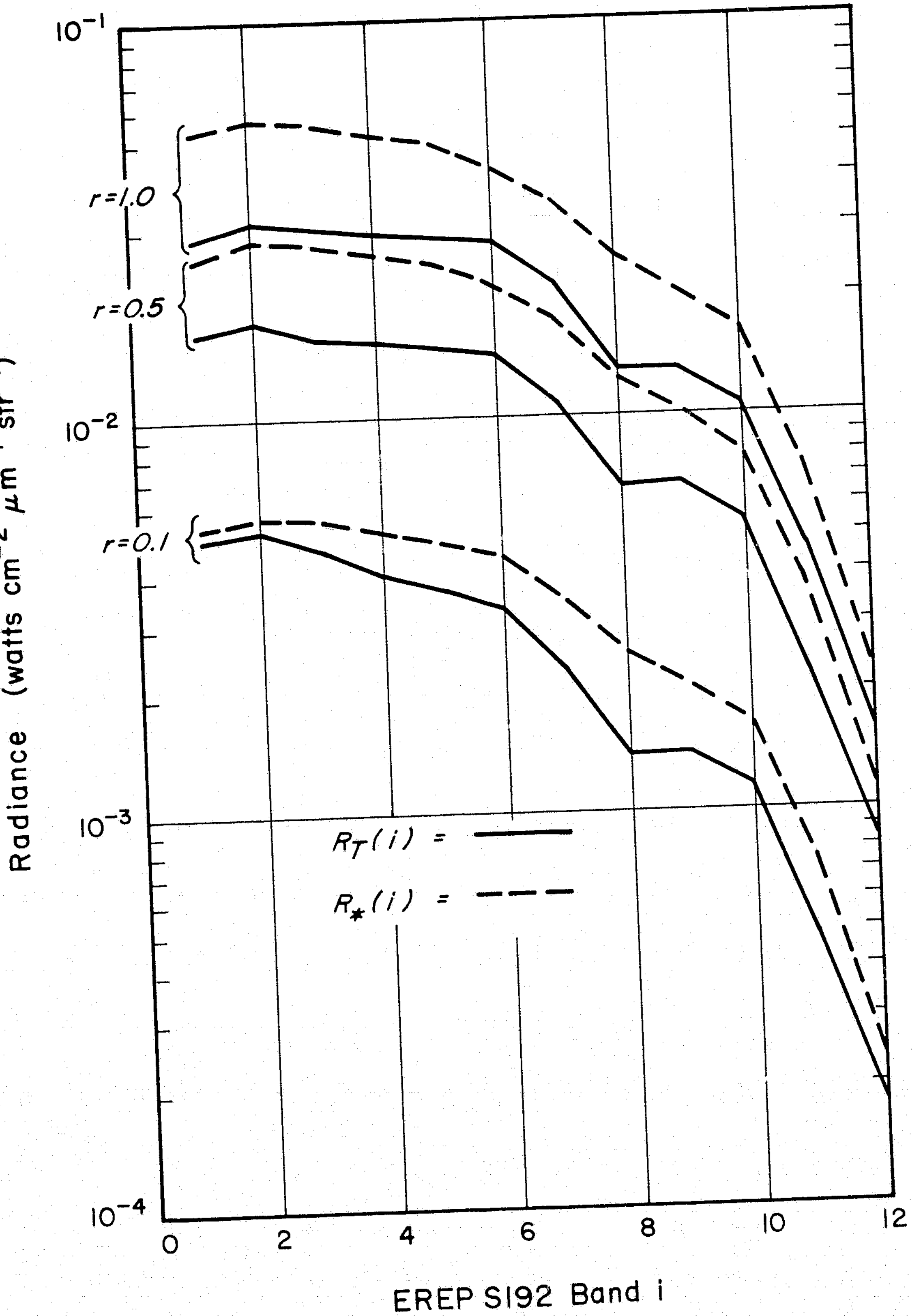

Figure 7.1 S192 Radiance Spectra for Absence of an Atmosphere

507045

Dependence of measured radiance on surface reflectance for selected EREP S192 bands is demonstrated in Figures 7-2 through 7-8. Calculations here are performed for the summer midlatitude atmosphere. Individual calculations are piecewise connected for clarity. Also indicated are the corresponding atmosphereless radiances $R_*(i)$. (Since a radiance which is identically zero cannot be plotted on these axes, the curve for $R_*(r \to 0.0)$ is extrapolated.) The general behavior indicated from comparison of the two curves (R_T and R_*) in each band denotes a variation of the simulated radiance dependence on surface reflectance from the direct proportionality predicted for the atmosphereless radiance [see Equation 6-1]. This is most pronounced in the visible bands (see Band 1, Figure 7-2) where the slope of the two curves differ considerably. In the near IR bands, although the curves in general differ in magnitude, the slopes are similar. The difference between these curves (i.e., Equation 6-3) is a fundamental measure of the atmospheric effect. Behavior of the atmospheric effect as the surface reflectance approaches zero is indicated by the limits:

$$\lim_{r \to 0.0} \quad R_*(i) \to 0.0$$

$$\phantom{\lim_{r \to 0.0}} \quad R_T(i) \to \frac{I(i)\ J(i,\ \theta_o,\ r = o,\ \tau^*)}{\pi}$$

or

$$\lim_{r \to 0.0} \Delta R_*(i) \to \frac{I(i)\ J(i,\ \theta_o,\ r = o,\ \tau^*)}{\pi}$$

Therefore, the atmospheric effect will always be positive in the limit of extremely low reflectance where the measured radiance is characteristic of the atmosphere only and the atmospheric effect is maximum.

Expressed in terms of the equivalent change in surface reflectance Δr_* (Equation 6-5), these results become most apparent. Figures 7-9 and 7-10 demonstrates the percent change in equivalent surface reflectance above the true surface reflectance, i.e., plotted is $[\Delta r_*(i)/r(i)] \times 100\%$ for each EREP S192 band. The level of zero atmospheric effect is denoted by the dotted line. (The absolute value of the equivalent change in surface reflectance is available by multiplying the plotted values by $r(i)/100$.) Confirming earlier conclusions, the effect is greatest in

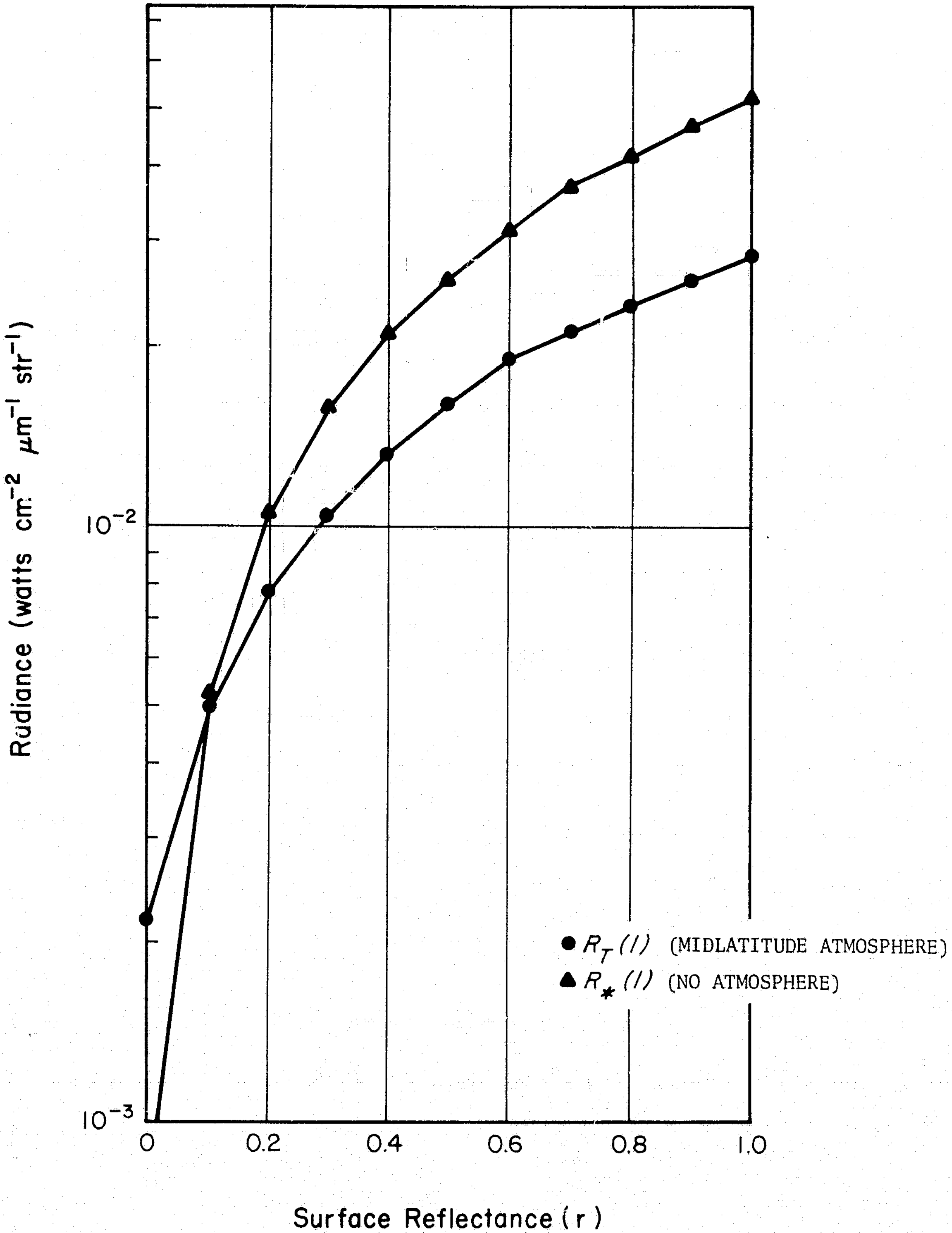

Figure 7.2 Effects of the Atmosphere on Band 1 Radiance Computed for a Midlatitude Atmosphere. Corresponding Radiance Computed for no Atmosphere is shown for Comparison.

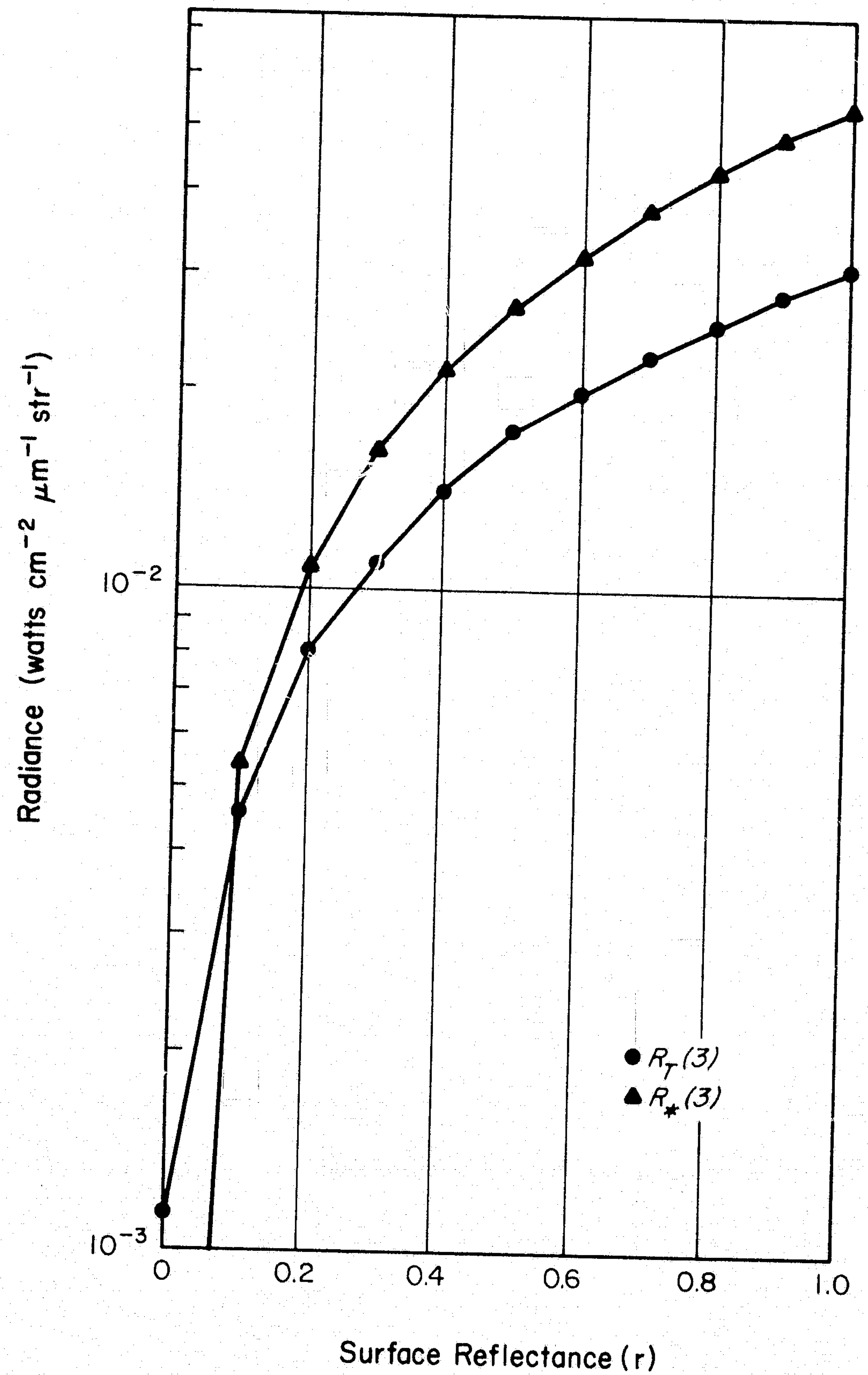

Figure 7.3 Effects of the Atmosphere on Band 3 Radiance Computed for a Midlatitude Atmosphere. Corresponding radiances Computed for no Atmosphere are shown for Comparision.

507033

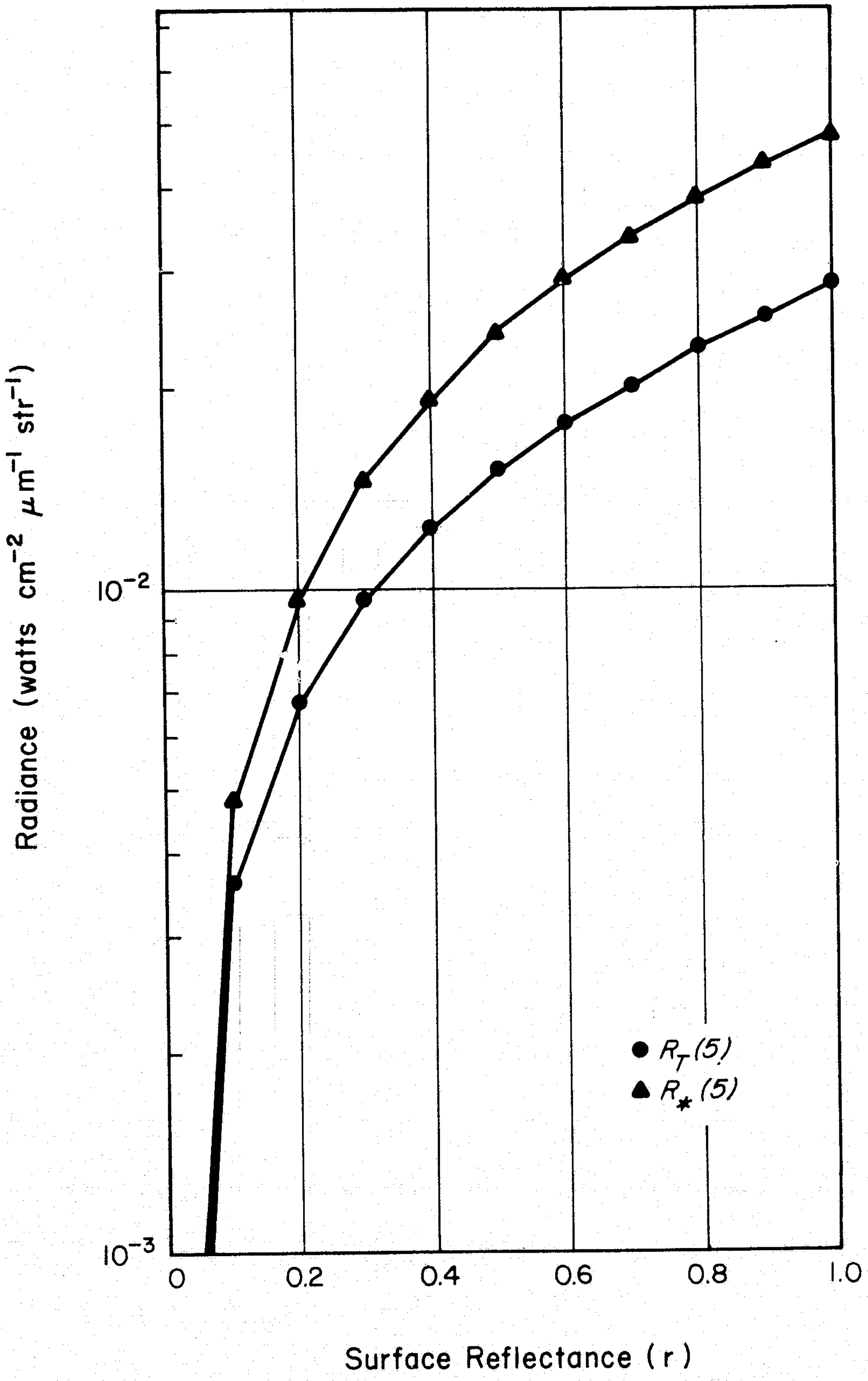

Figure 7.4 Effects of the Atmosphere on Band 5 Radiance Computed for a Midlatitude Atmosphere. Corresponding Radiances Computed for no Atmosphere are shown for Comparision.

507034

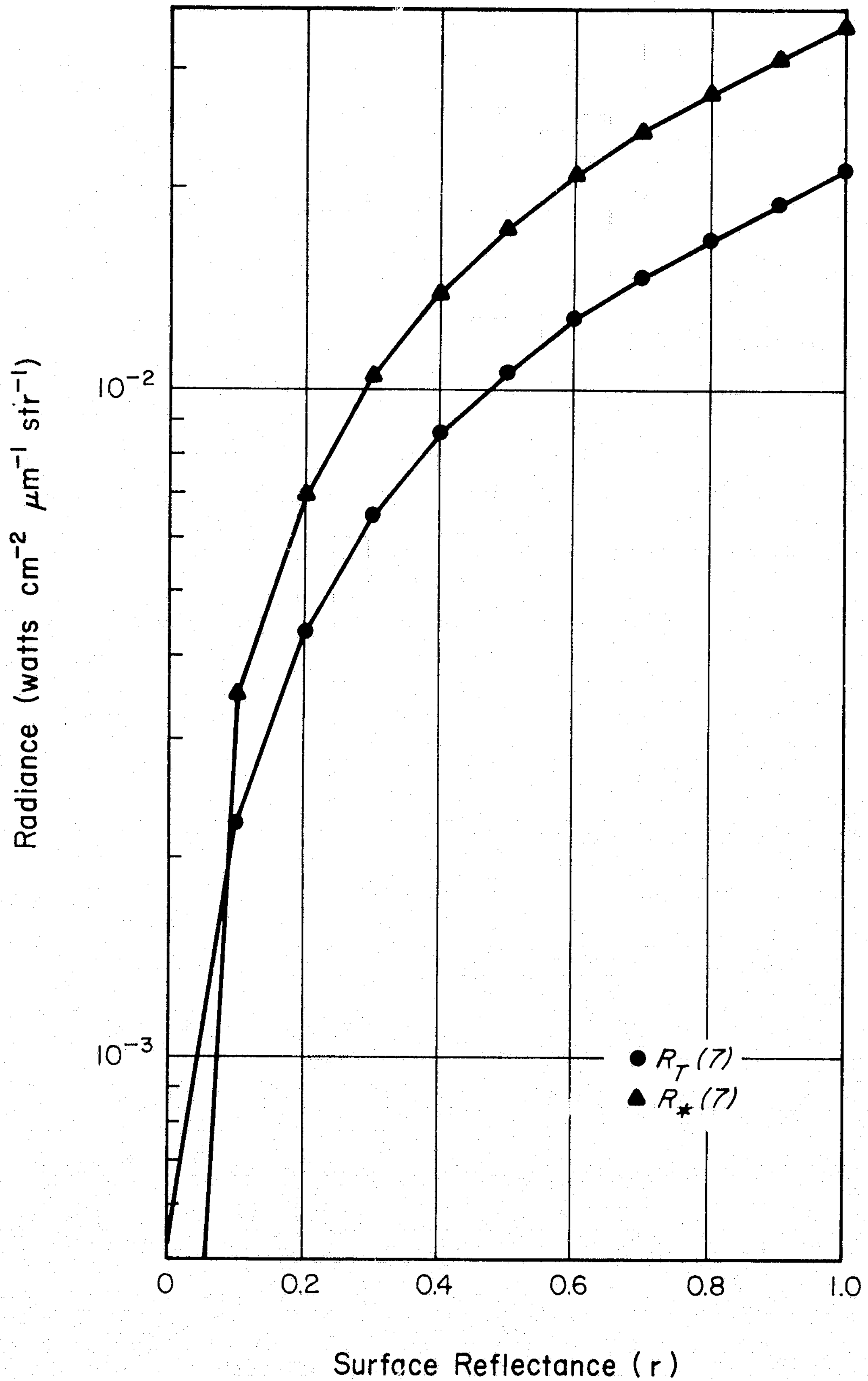

507032

Figure 7.5 Effects of the Atmosphere on Band 7 Radiance Computed for a Midlatitude Atmosphere. Corresponding Radiances Computed for no Atmosphere are shown for Comparison.

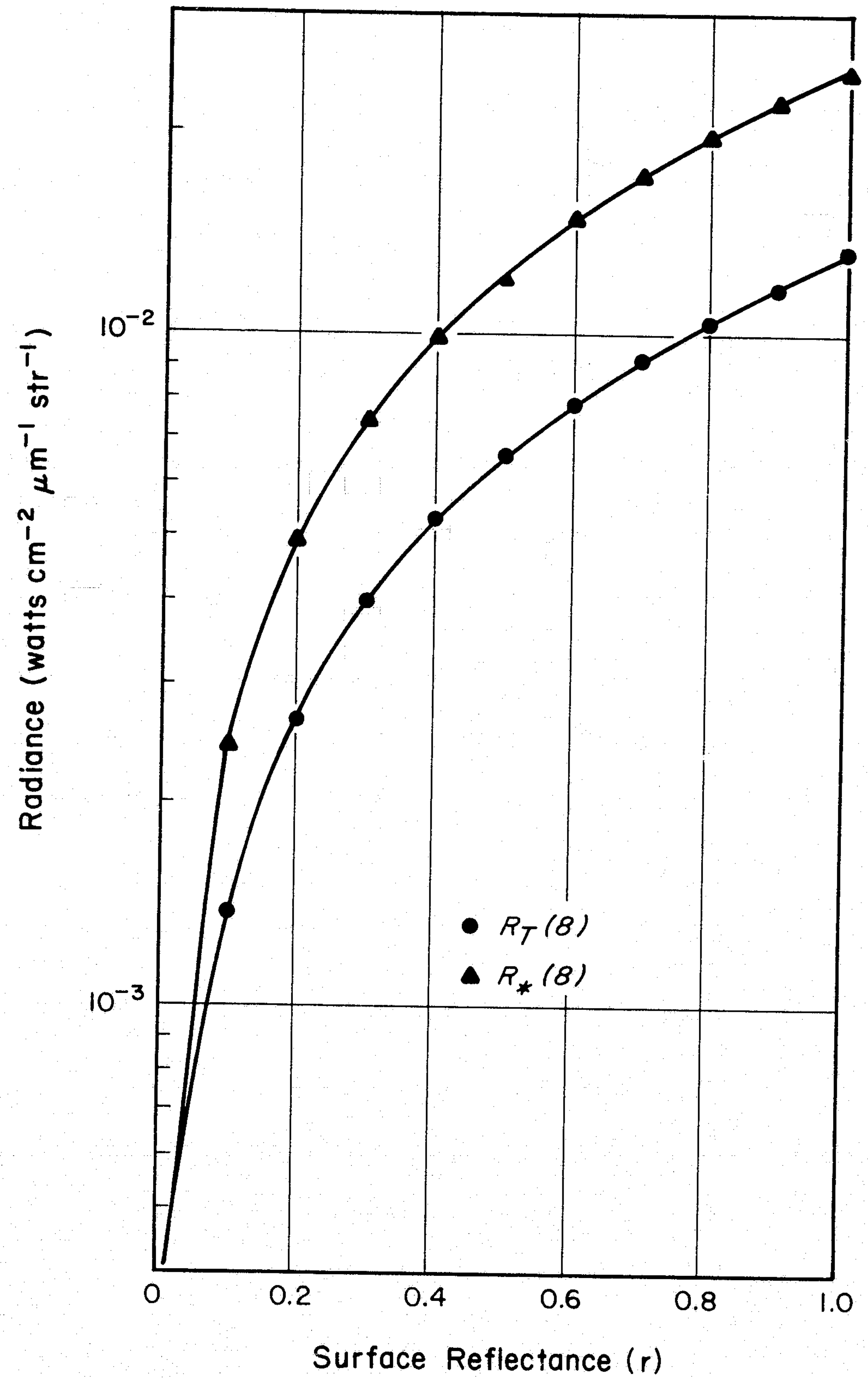

Figure 7.6 Effects of the Atmosphere on Band 8 Radiance Computed for a Midlatitude Atmosphere. Corresponding Radiances Computed for no Atmosphere are shown for Comparison.

507042

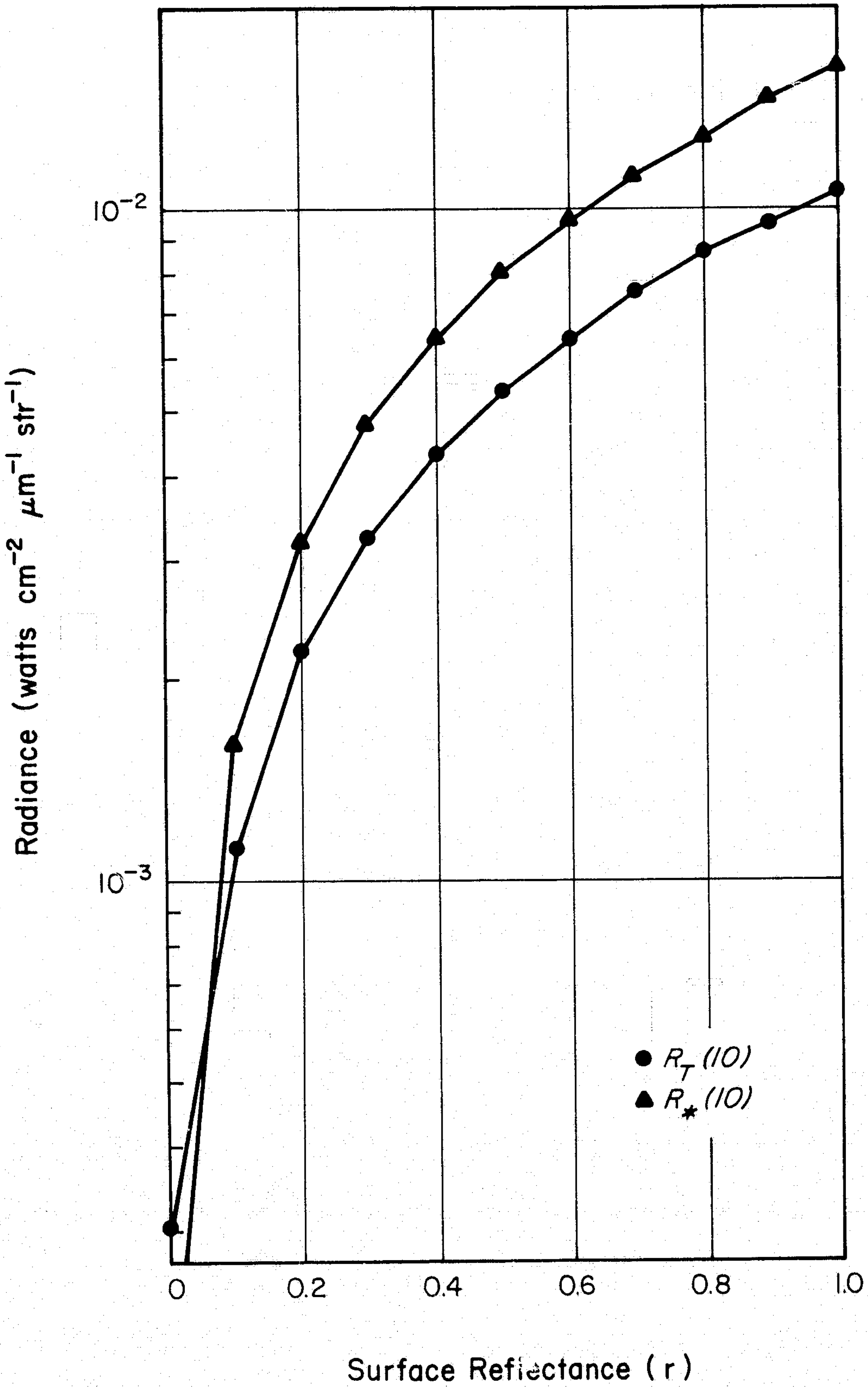

Figure 7.7 Effects of the Atmosphere on Band 10 Radiance Computed for a Midlatitude Atmosphere. Corresponding Radiances Computed for no Atmosphere are shown for Comparison.

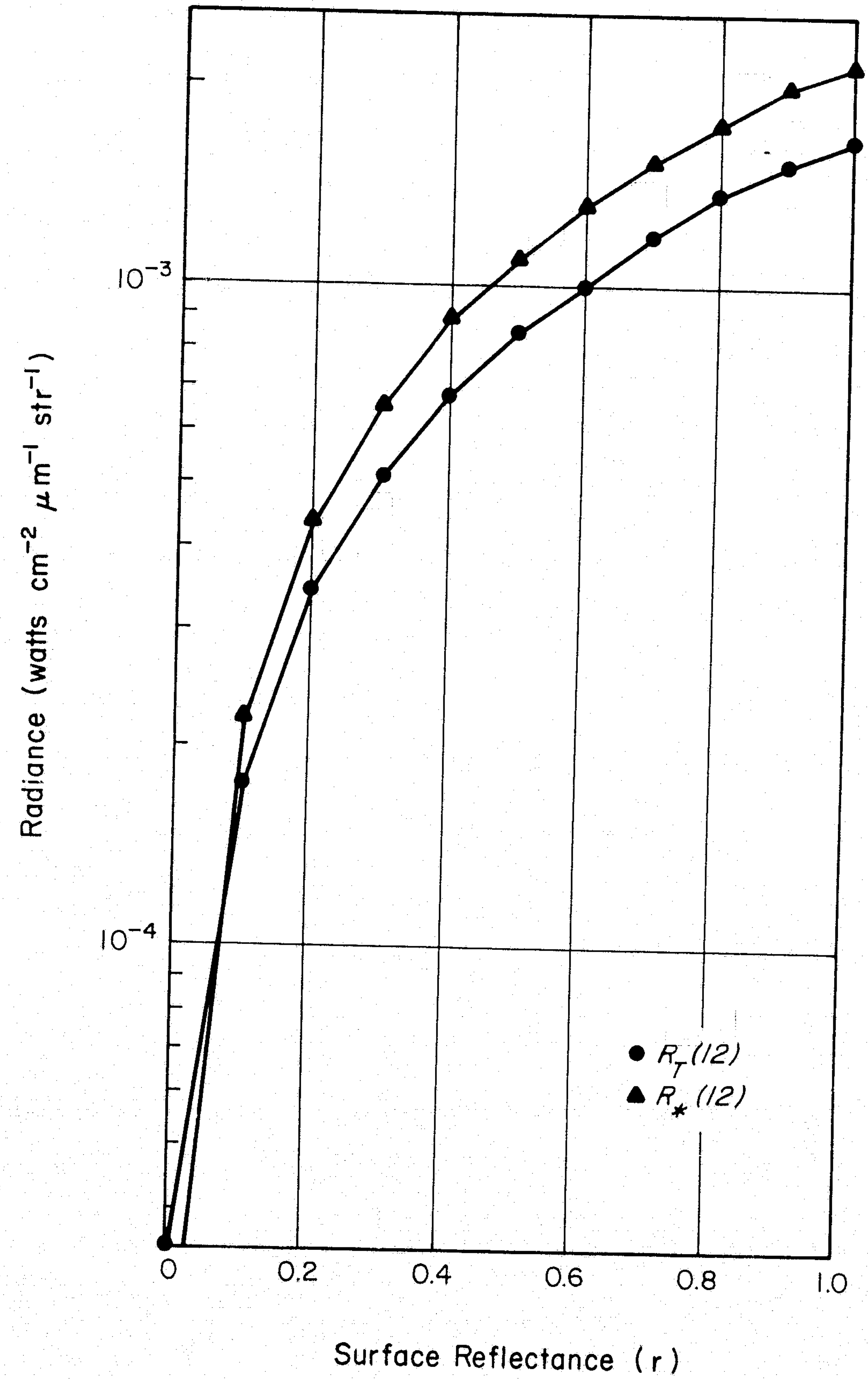

Figure 7.8 Effects of the Atmosphere on Band 12 Radiance Computed for a Midlatitude Atmosphere. Corresponding Radiances Computed for no Atmosphere are shown for Comparison.

507040

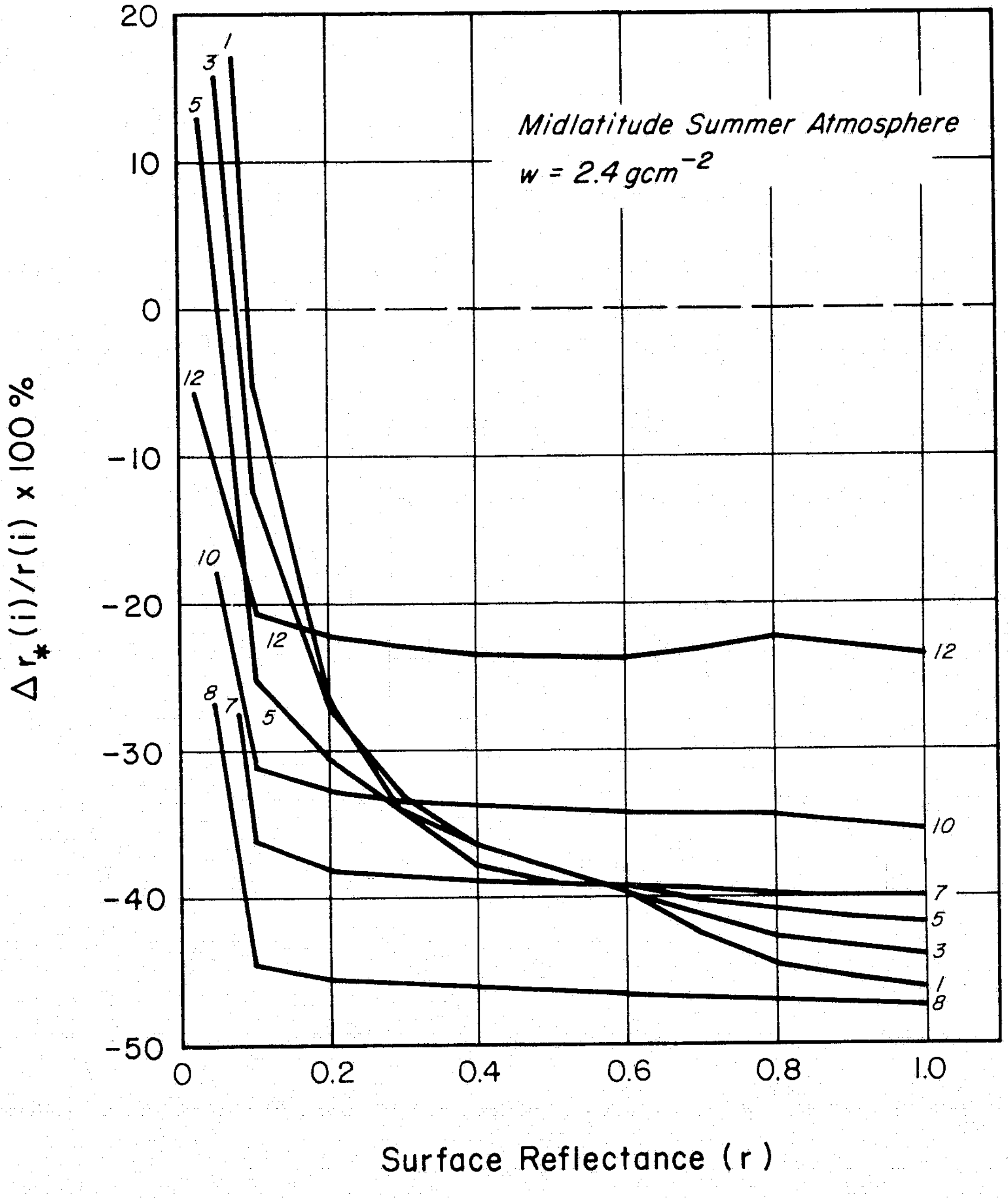

Figure 7.9 Effects of the Atmosphere on Surface Reflectance Computed for a Midlatitude Summer Atmosphere.

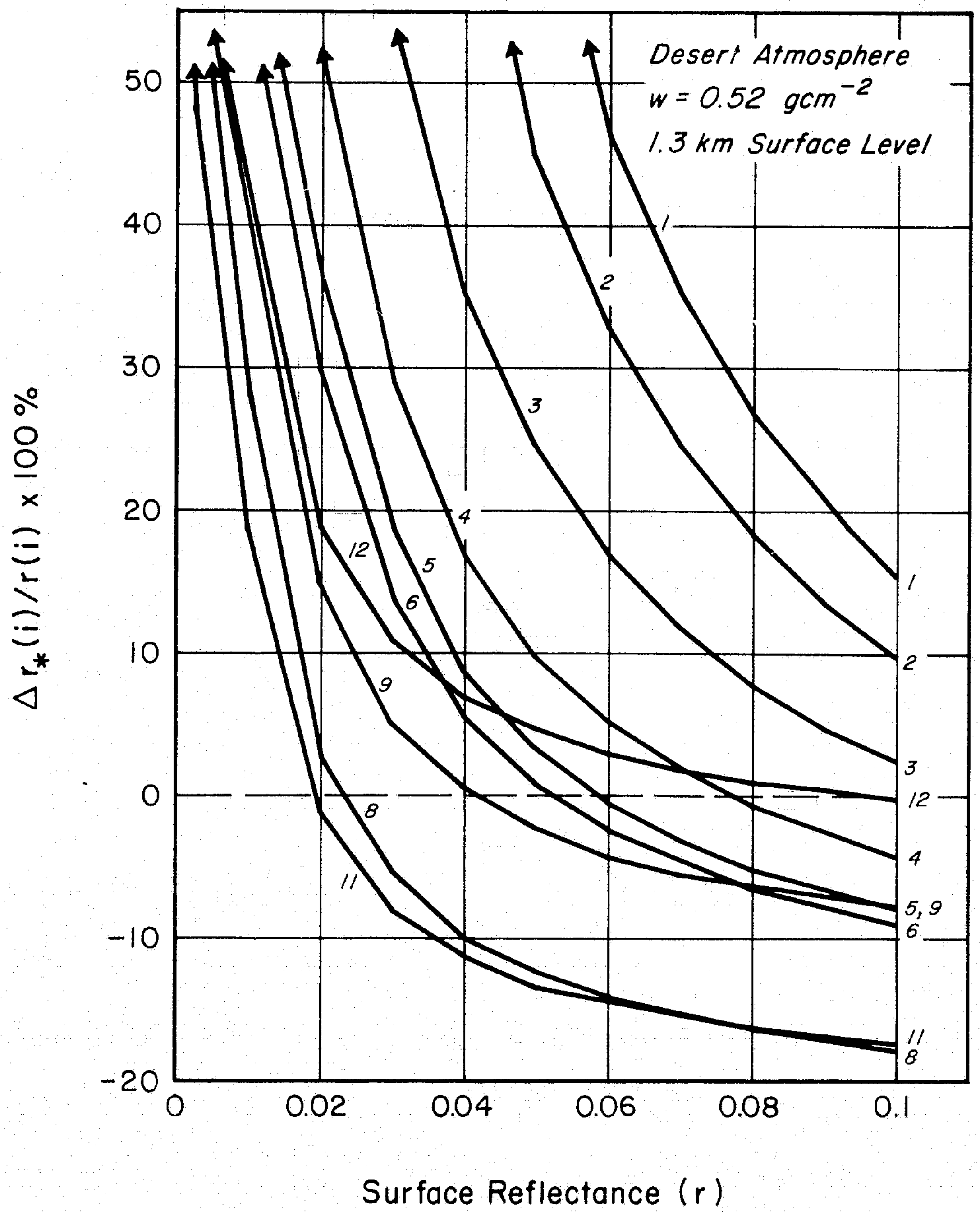

Figure 7.10 Effects of the Atmosphere on Surface Reflectance Computed for a Desert Atmosphere.

all bands at low surface reflectances where the percent error in determining surface spectral properties becomes considerable. At higher surface reflectance values, there is a fundamental difference between the behavior of the visible bands and near infrared bands. Most interesting is the differing dependence of the visible (1,3,5) and near IR (7,8,10,12) bands on surface reflectance. While the latter bands are almost constant at all but the lowest (< 0.1) surface reflectances, the visible bands possess a distinct curvature approximating an r^{-1} dependence which becomes stronger as wavelength decreases. This suggests an effect due to scattering which can be verified by the theoretical expression:

$$\frac{\Delta r_*}{r} = (T_z T_\theta - 1.0) + J/r \sin \theta_o \qquad (7\text{-}1)$$

The first term above is independent of surface reflectance and will dominate where path radiance is small (i.e., the near IR at moderate surface reflectances). However, where path radiance is a significant fraction of the measured radiance (visible and at low surface reflectances), a distinct r^{-1} behavior will be evident whose magnitude is determined by the leading constant term in the expression for J (see Equation 3-2). This term is largest in the lowest visible EREP S192 bands and decreases into the near IR. Behavior at the lower surface reflectance values ($r \leq 0.1$) is verified in Figure 7-10 calculated for the desert atmosphere corresponding to site D (Section 4.2.1) with integrated water vapor of ~ 0.5 gcm^{-2}. Again, as the surface reflectance approaches zero, the percent error in determining the magnitude of the surface reflectance approaches large positive values. In this low reflectance region where path radiance is important, the largest positive atmospheric effects are in the shortest wavelength visible bands decreasing into the near IR. The least affected bands are adjacent to water vapor absorption features in the near IR (e.g., 8 and 11).

7.2 Surface Reflection Correction Curves

The results of the previous section may be expressed in a practical manner by plotting curves of equivalent reflectance (Equation 6-4) which are directly proportional to band radiances vs. the true surface reflectance. These surface reflectance correction curves would have unit slope if there were no atmospheric effect, but differ substantially from unity due to attenuation by atmospheric gases and particulates.

Figure 7-11 is drawn from calculations for the summer midlatitude atmosphere. Plotted are selected EREP bands (1,3,5,7,8,9,10,11,12). For a given solar evevation angle, the vertical axis of this figures is directly proportional to the raw S192 band digital counts (0-255) with unique scales for each respective band. As an example of the utility of these curves, consider the following. If atmospheric conditions coinci-dent with an EREP pass were characterized by the midlatitude summer atmosphere described and a reflectance value of 0.50 was determined from a radiance measurement in band 7, the true surface reflectance would be 0.83, i.e., we would significantly underestimate based on the uncorrected radiance alone. (Note in Figure 7-9 that the predicted error is $\sim$ -40% in band 7 at $\sim r = 0.80$. From above, the error is (0.50 - 0.83)/(0.83) x 100% = 39.75%). In a like manner, the reflectance spectrum determined from space can be reduced to a corrected spectrum by applying a similar procedure in each EREP S192 band. The magnitude of the correction applied may be quantified by the variation of each correction curve from the "no atmosphere" curve. The least correction for this atmospheric model need be applied in band 12, and the greatest in band 8 (which is particularly sensitive to water vapor). Intermediate corrections are necessary in bands 1,2,3,4,5,6,7,9,10, and 11, the most severe being in the short wavelength visible and decreasing in magnitude into the near IR. Note that all curves intersect the no atmosphere curve at low reflectances where the sign of the correction changes due to path radiance effects (i.e., surface reflectances are over determined due to scattering enhancement.

Similar results for a midlatitude winter atmosphere are demon-strated in Figure 7-12. The basic change is a decrease in the inte-grated water vapor amount to 0.9 gcm^{-2}. Note particularly the shift in all IR bands toward smaller correction values. Band 8 in particular becomes less affected by atmospheric effects than most of the visible bands when water vapor is diminished. This result indicates that although the near IR band filters were chosen to be in spectrally

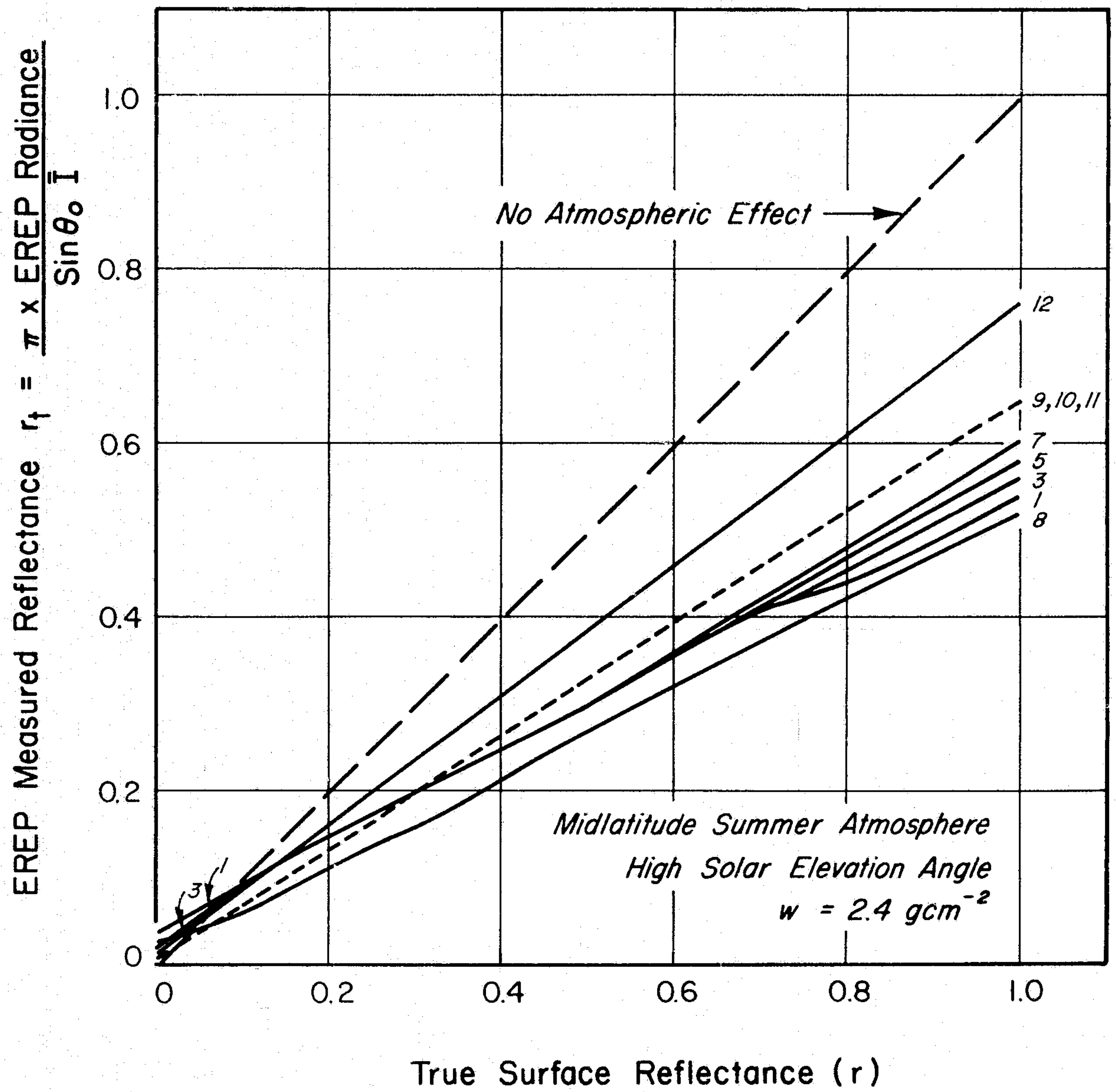

Figure 7.11 Surface Reflectance Correction Curves-Midlatitude Summer Atmosphere

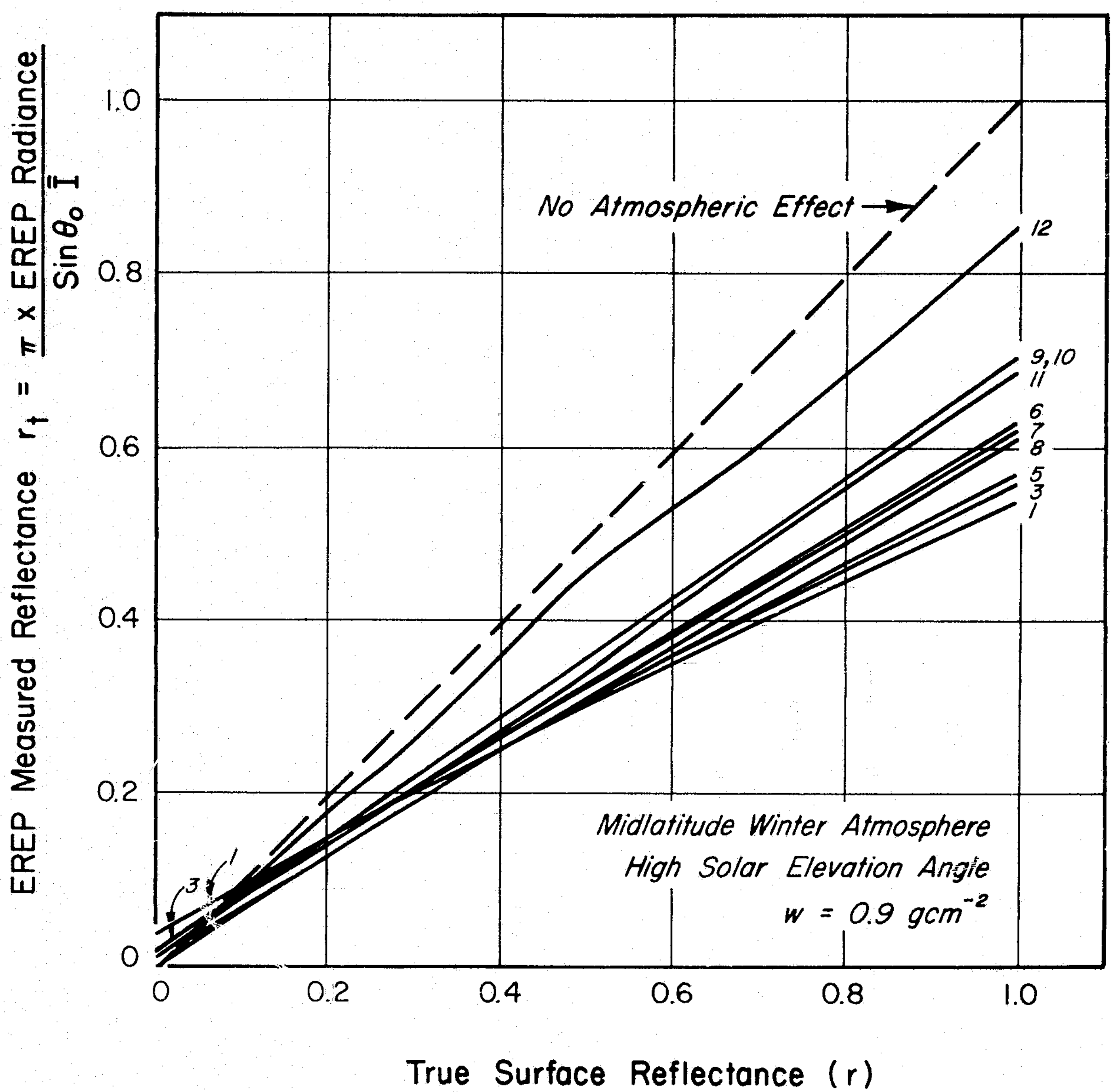

Figure 7.12 Surface Reflectence Correction Curves-Midlatitude Winter

transparent windows, there remains a marked residual dependence of radiance response to atmospheric water vapor. No doubt these effects are due to the wings of the water vapor rotational bands described in Section 2. It must, therefore, be concluded that in this sensor configuration careful note must be taken of the atmospheric water vapor to interpret results in the near IR bands. Returning to the figure, note that the visible bands are not responsive to the change in atmosphere at all.

As an example of a particularly "clean" atmosphere, Figure 7-13 illustrates analogous results corresponding to the desert atmosphere of site B (Section 4.2.1) with a still lower value of the integrated water vapor ($\sim 0.5\ gcm^{-2}$). The essential difference between this case and the earlier two, however, is the surface altitude. Here, the surface is located at 1.3 km, contrasting with previous sea level atmospheres. As a consequence, integrated absorber amounts are smaller for all atmospheric constituents, including the integrated density itself which determines the magnitude of the scattering effect in the visible bands. Note in the figure that the corrections in the visible region are markedly decreased, as are all other bands.

Corrections at lower reflectances are considerably different than those at moderate levels as earlier results indicate. In Figure 7-14, sample correction curves are illustrated for the site D atmosphere (Section 4.2.1). Note that for the most part, reflectances based on EREP radiances must be adjusted down in magnitude to account for atmospheric back-scattering. Even when the actual surface is completely absorbing (i.e., water in near IR), there is a finite determinable equivalent surface reflectance due to scattering, whose magnitude decreases with increased wavelength (see Section 7.1 for this limit).

Consequences of these results are summarized in Figure 7-15 where the slope of each curve in Figures (7-11 through 7-14) is plotted. The following conclusions may be drawn:

1) The visible bands (1,2,3,4,5,6,7) are generally insensitive to absorption by atmospheric water vapor. However, since scattering is significant in these spectral regions, corrections to be applied to radiance data will be sensitive to integrated density (i.e., surface altitude).

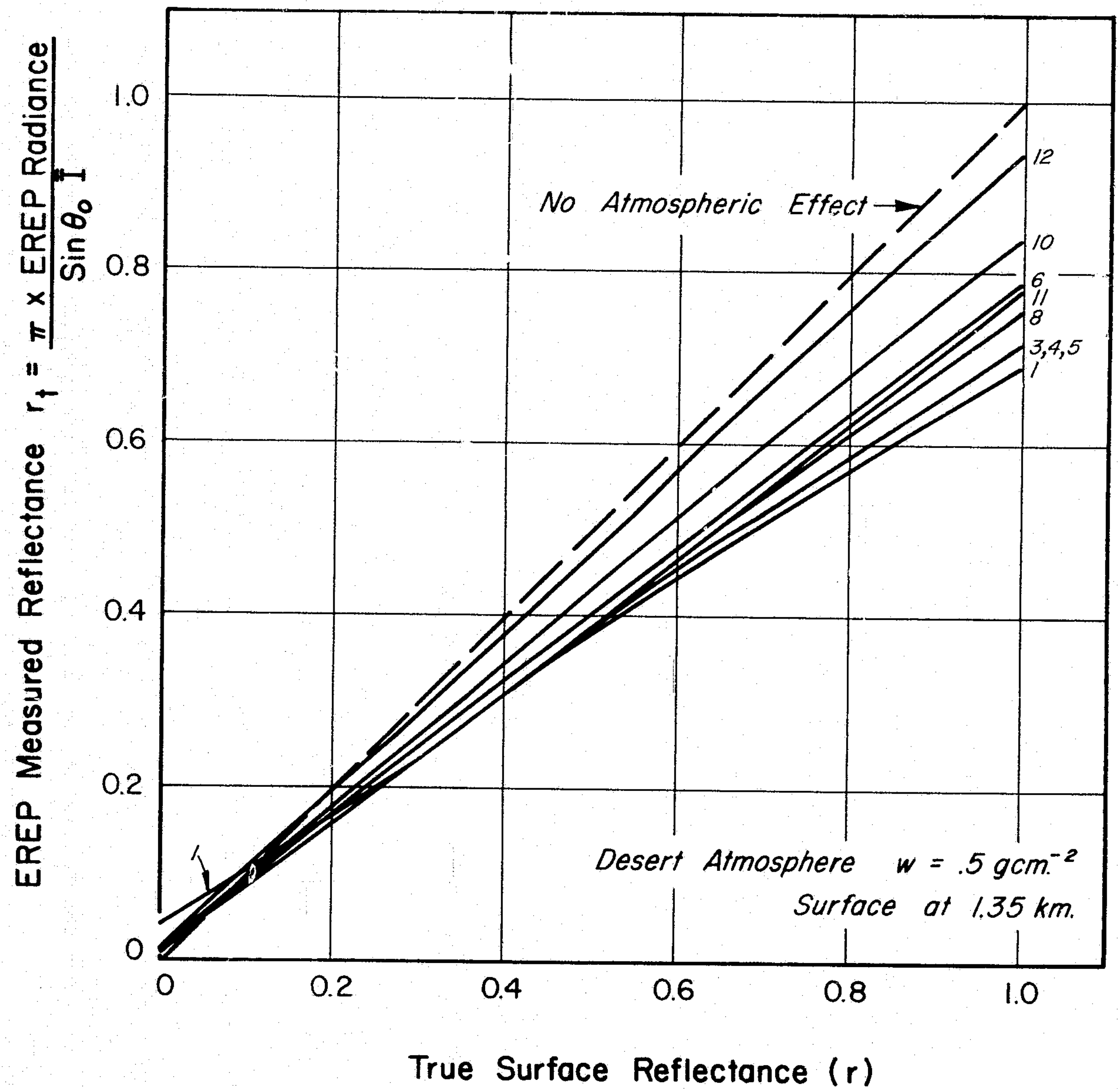

Figure 7.13 Surface Reflectence Correction Curves-Desert Atmosphere

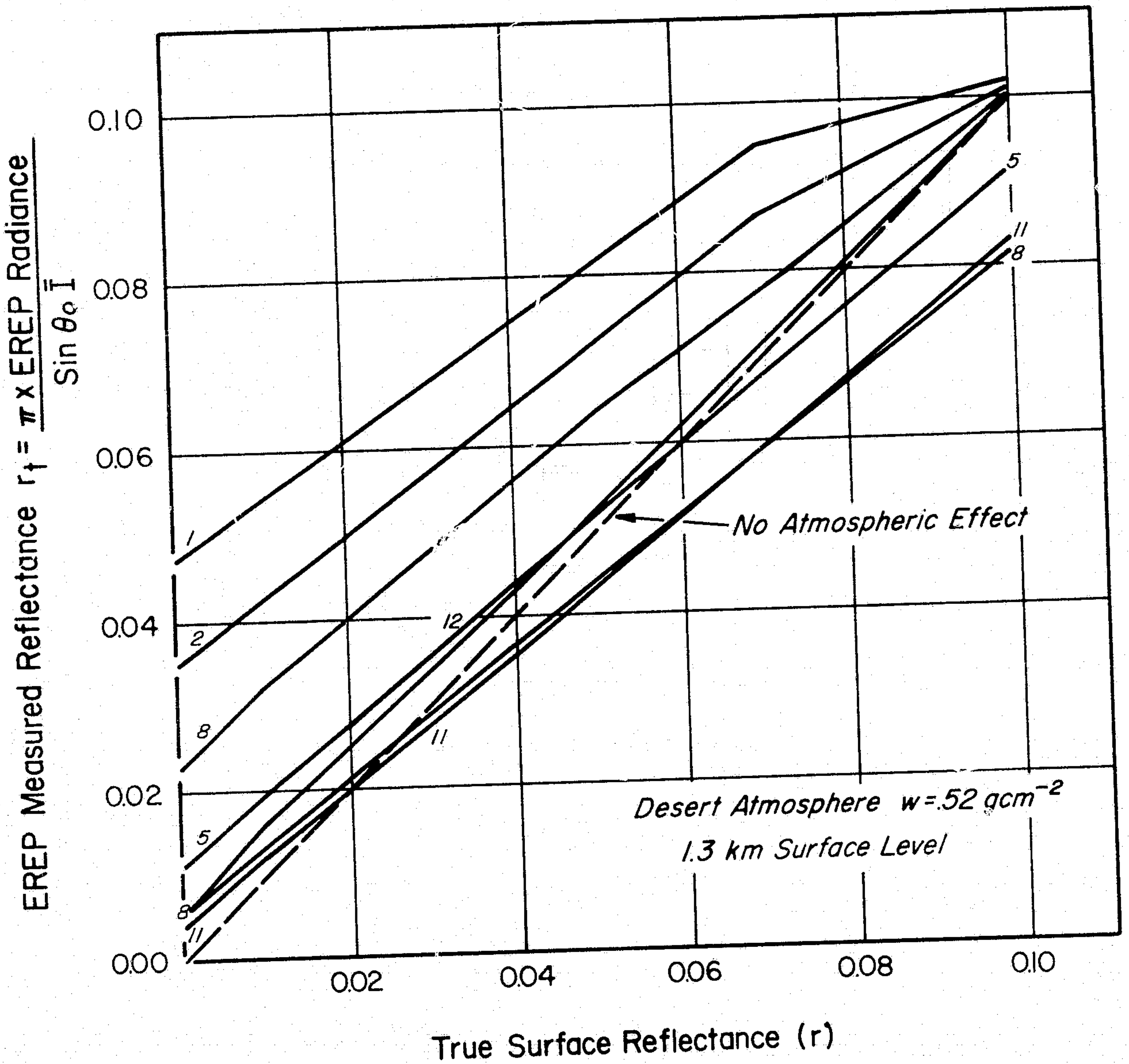

Figure 7.14 Surface Reflectence Correction Curves for Site "D"

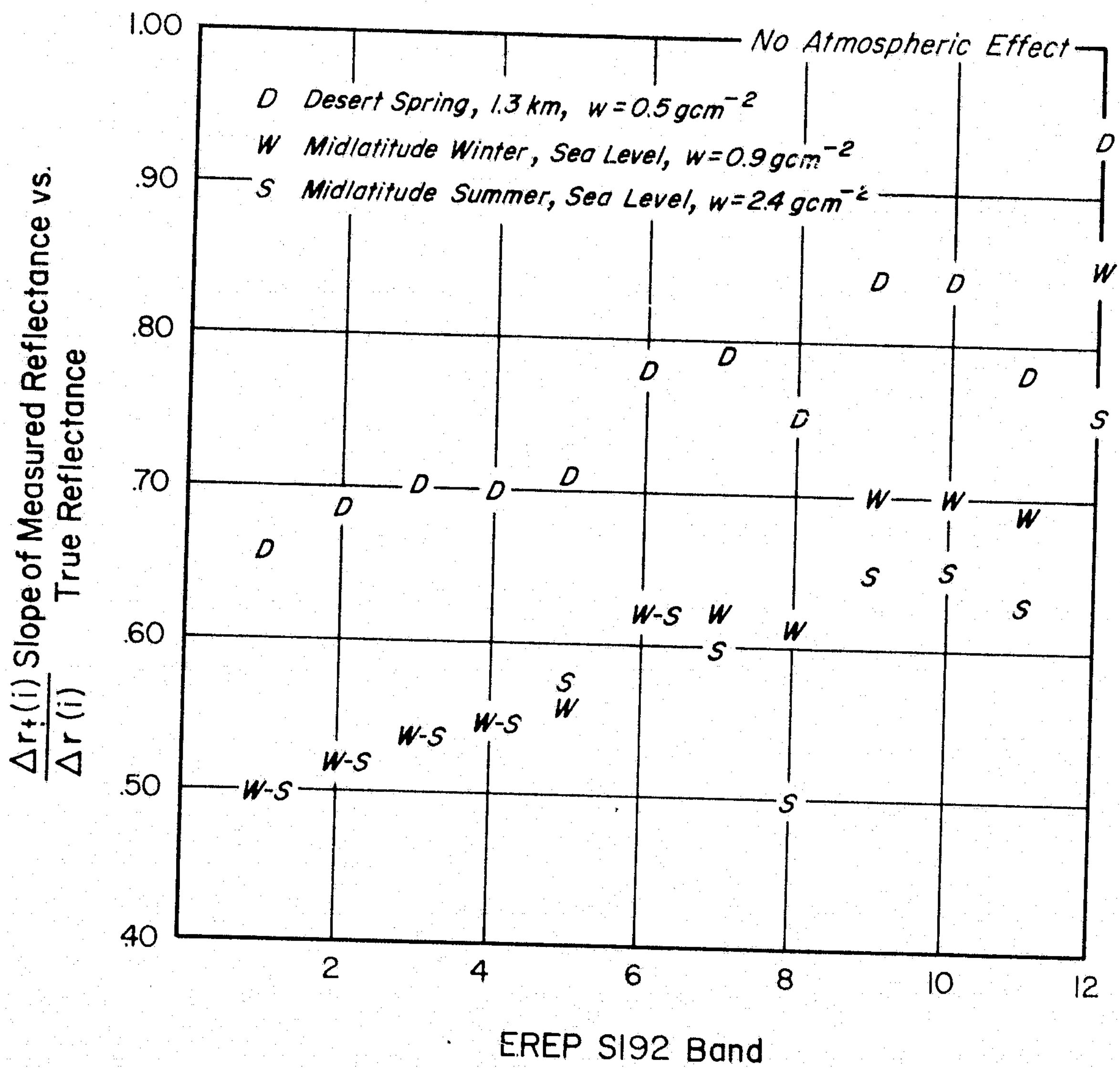

Figure 7.15 Summary of Reflectence Correction Expressed as Slope Values

2) All of the near IR bands (8,9,10,11,12) are sensitive to atmospheric water vapor absorption with band 8 most affected. Since the continuum absorption in this region is largely due to scattering, these bands will also be affected by the surface altitude.

3) In general, corrections applied to EREP S192 radiance data will be extremely sensitive to the atmospheric conditions concurrent with the measurement as the diversity of points in Figure 7-15 indicates. As a minimum, the integrated water vapor and surface height above sea level should be known.

7.3 Atmospheric Modification of Scene Contrast

Neighboring surface area elements with distinctly different spectral reflectance properties within a given band will be distinguishable by their inherent contrast. Viewed from a space-based platform, the nature of this contrast may be modified as atmospheric effects alter the apparent measured surface reflectivities as discussed in the previous section. Calculations based on the definitions of inherent contrast, C_*, apparent contrast, C_T, and the contrast modification ratio ΔC (see Section 6.3) were performed for the summer midlatitude atmosphere. Results are illustrated in Figure 7-16 where apparent contrasts are plotted as a function of EREP S192 band for three values of the inherent contrast $C_* = 2,4,8$. These correspond to neighboring surface area elements, which are three, five, and nine times more reflective than each other, respectively. Two apparent contrast curves are plotted for the $C_* = 2$ case, one for neighboring low reflectance surfaces (0.1 and 0.3) and one for neighboring high reflectance surfaces (0.3 and 0.9). The shape of each apparent contrast curve, $C_T(i,r_1,r_2)$ is similar. Contrast is most altered in the visible bands with the magnitude of the effect decreasing with increasing wavelength. In the near infrared, contrast modification appears to be minimal in all bands. Based on the spectral dependence of the effect, it is expected that scattering is the primary cause. It is expected, therefore, that contrast modification will be a function of surface reflectance itself and most pronounced at low reflectances. This is confirmed comparing the $C_T(i,.9,.3)$ and

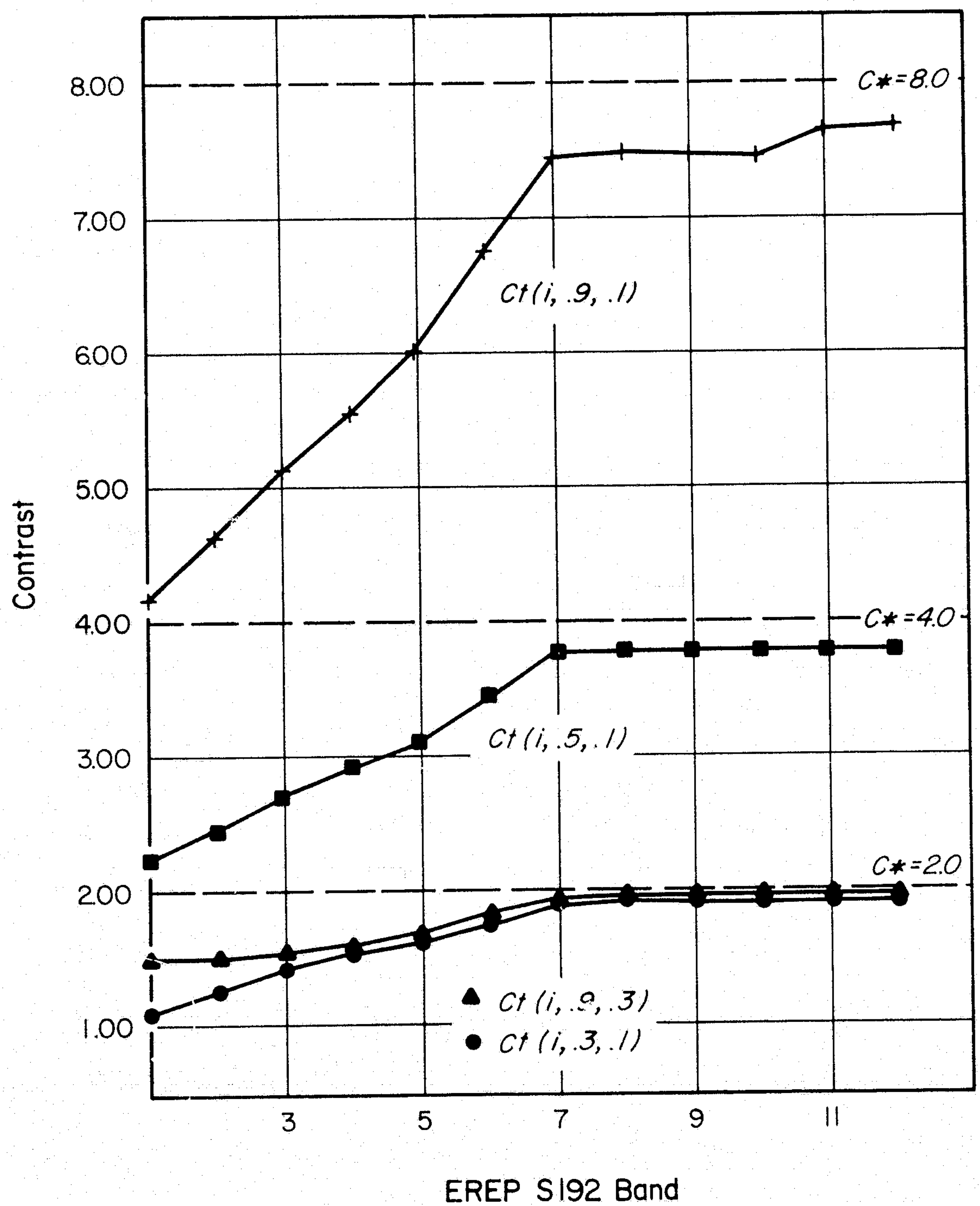

Figure 7.16 Effects of the Atmosphere on Surface Contrast, Expressed as Apparent Contrast CT, for selected selected surface pairs, e.g. C_T(i, .9, .3) is the Apparent Contrast for Surface Pair with Surface Reflectances r_1=.9 and r_2=.3. Computations are Based on Midlatitude Summer Atmosphere as viewed in the i^{th} band.

507017

$C_T(i,.3,.1)$ curves. Note that the effect is more pronounced in the latter curve, especially in the visible region.

These results are made most apparent by examining the contrast mosification ratio for the cases described above. In Figure 7-17, the ratios of the respective curves for C_T and C_* depicted in Figure 7-16, are plotted on the same axes. A characteristic curve for the case $r_1 = 0.5$, $r_2 = 0.1$ is drawn by piecewise connecting the computed value in each band. In the near IR (bands 7,8,9,10,11,12) most points cluster closely. Here the contrast reduction is negligible (∿ 5%) for the cases calculated. In the visible, however, the degree of contrast modification is a strong function of band ranging from ∿ 15% in band 6 to a maximum value of ∿ 48% in band 1 when surface reflectances are low ($r_1 = 0.3$, $r_2 = 0.1$). Contrast reduction in these bands will be weakly dependent on surface reflectance and the maximum effect in band 1 can be reduced to ∿ 25% when both surfaces are moderately high reflectances ($r_1 = 0.9$, $r_2 = 0.3$).

7.4 Effects on Band Radiance Ratios

The ratio of radiances in different spectral bands is often used in earth resources remote sensing investigations to make quantitative assessments regarding surface target properties. If there is no atmospheric effect, band ratios will be proportional to the ratio of target spectral reflectances and a constant defining the solar continuum ratio (Equation 6-9). Band ratios using space based measurements will be modified by the atmosphere yielding values either higher or lower than the corresponding atmosphereless quantities depending on both surface reflectance, atmospheric properties, and the particular bands utilized. Figure 7-18 plots calculated values of the band ratio modification $\Delta q(i,j)$ given by Equation 6-11 for surfaces with constant reflectances in each band [i.e., $r(i) = r(j)$]. These values are representative of a midlatitude summer atmosphere. Values are given for (i,j) pairs (1,3), (3,5), (5,7), (7,9), (9,11) and (3,8). These particular band ratios were chosen to include bands in spectral regions with similar atmospheric extinction properties [e.g., (1,3) the visible and (9,11) in the near IR] and diverse properties [e.g., (3,8)]. The level of zero atmospheric effect is indicated.

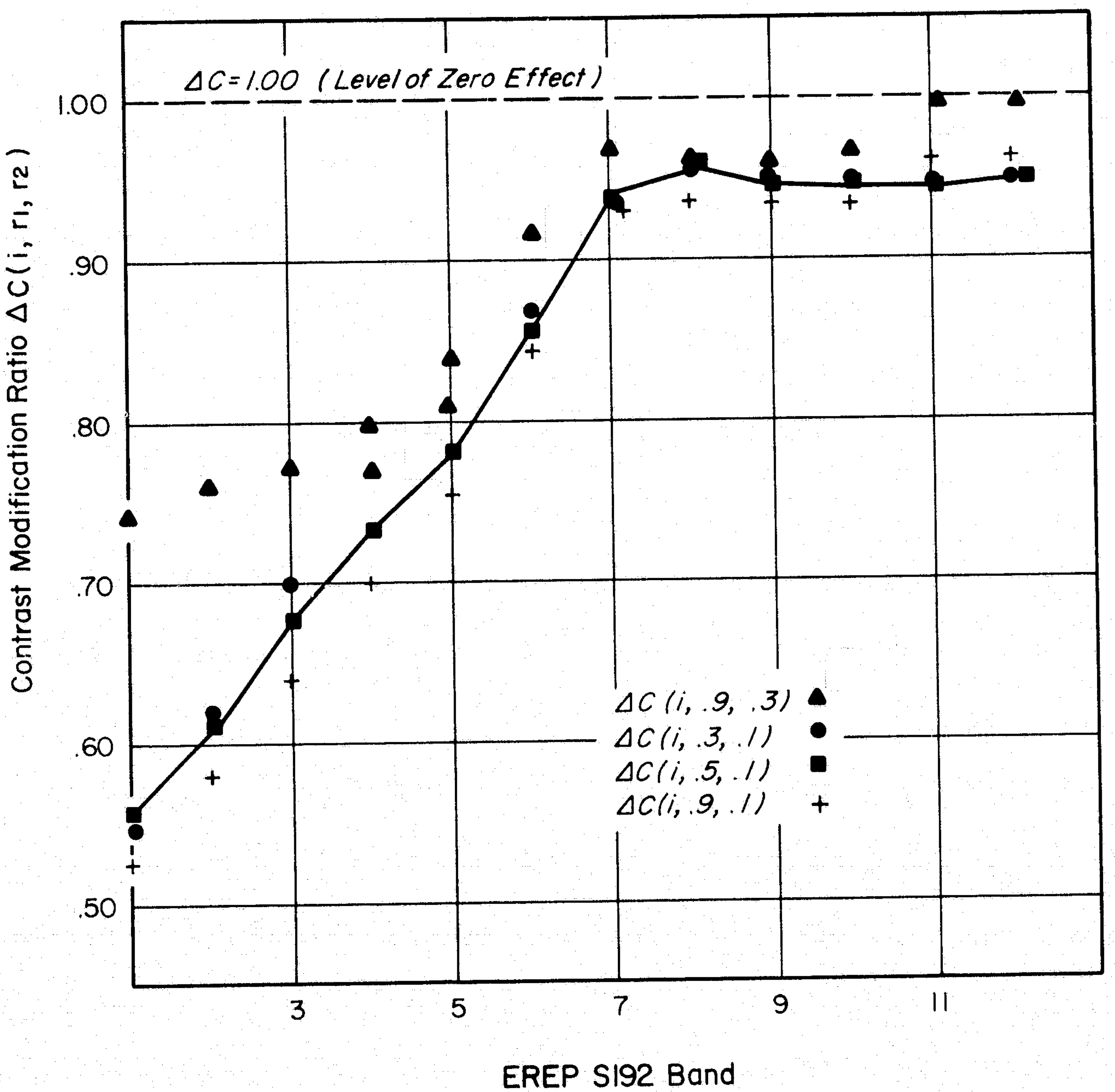

Figure 7.17 Surface Reflectance Contrast Modification for Selected Surface Reflectance Pairs computed using Midlatitude Summer Atmosphere, where C(i, .9, .3) is the Contrast Modification Ratio for Surface Pair with reflectances r_1=.9 and r_2=.3 as viewed in the i^{th} Band.

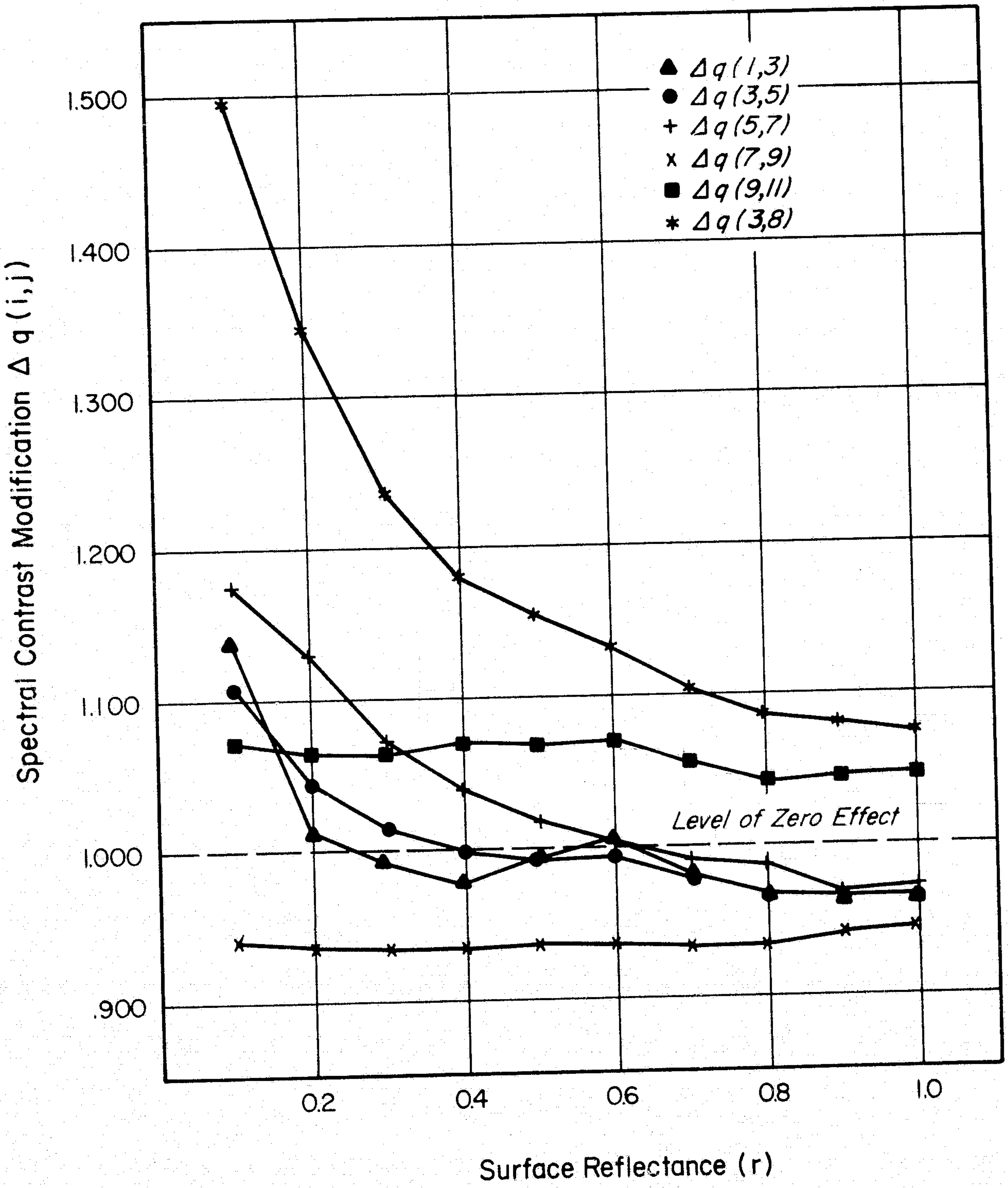

Figure 7.18 Spectral Contrast modification Computed for Selected Band Pairs using a Midlatitude Atmosphere Assuming that the Inherent Contrast between the Band Pairs i,j, is unity.

507019

As might be expected, ratio modification is greatest when surface reflectance is low. In the visible bands where the sloping continuum of molecular and aerosol scattering determine atmospheric extinction, band ratio modification is a strong function of surface reflectance. Values range from greater than unity ($r \lesssim 0.6$) to less than unity $r \gtrsim 0.6$. In general this is due to the larger proportional path radiance contribution at lower surface reflectances for the shorter wavelength visible bands. In the near IR where absorption dominates, the band ratio modification tends to be independent of surface reflectance [e.g., $\Delta q(7,9)$, $\Delta q(9,10)$] depending only on the fundamental transmissivity differences between bands. Whether this "constant" value is greater than or less than one will depend on the relative transparence of the particular bands. For example in the figure, since band 9 is more spectially transparent than either 7 or 11, the "constant" value of $\Delta q(i,j)$ changes sense depending on whether band 9 is in the numerator or demoninator.

[e.g., in the near IR $\Delta q(i,j) \approx \frac{T(i)}{T(j)}$ (see Equation 6-11)

since path radiance is small. Since

$$T(9) > T(7) \text{ and } T(9) > T(11),$$

$$\Delta q(7,9) = \frac{T(7)}{T(9)} < 1.0$$

but

$$\Delta q(9,11) = \frac{T(9)}{T(11)} > 1.0$$]

In general, the ratio of two MSS bands will be modified by an intervening atmosphere unless the right hand side of Equation 6-11 is identically unity. Since the information required to compute this term is dependent upon the atmospheric parameters describing fundamental absorption and scattering, it will not be possible to specify MSS band locations beforehand to insure no atmospheric effect. However, it may be possible particularly in the near IR to specify band locations in such a manner so as to minimize modifications of band ratios by insuring that extinction properties in each band are similar. This can be done by appropriately adjusting band filters between window and absorption areas to yield similar integrated extinction properties.

8. REFERENCES

Deirmendjian, D. (1963): Scattering and Polarization Properties of Polydispersed Suspensions with Partial Absorption, Proc. of the Interdisciplinary Conf. on Electromagnetic Scattering, Potsdam, New York, Milton Kerker, Ed., Pergamm on Press.

Elterman, L. (1968): UV, Visible, and IR Attenuation for Altitudes Up to 50 km, 1968, AFCRL, Environmental Res. Paper No. 285, AFCRL-68-0153.

Elterman, L. (1970): Vertical-Attenuation Model with Eight Surface Meteorological Ranger 1-13 Kilometers, 1970, AFCRL Environmental Res. Paper No. 310, AFCRL-70-0200.

Fraser, R., (1973): Computed Atmospheric Effects on ERTS Observations. NASA ERTS Symposium, Washington, D.C.

Fraser, R. (1973): "Computed Atmospheric Effects on ERTS Observations", Symposium on Significant Results Obtained from the Earth Resources Technology Satellite, Vol. 1, Sec. B, NASA SP-327.

Goody, R. M. (1964): Atmospheric Radiation, Clarendon Press, London.

Griggs, M., (1973): Determination of Aerosol Content of the Atmosphere. NASA ERTS Symposium, Washington, D.C.

Hunt, G. R., J. W. Salisbury, C. J. Lenhoff, (1970-1974): Visible and Near Infrared Spectra of Minerals and Rocks. I-IX. Modern Geology.

Krinov, E. L. (1947): "Spectral Reflectance Properties of Natural Formations" Laboratoriia Aerometodov, Akad. Nauk SSSR Moscow.

Malila, W. A. and R. F. Nalepka (1973): "Atmospheric Effects in ERTS-1 Data and Advanced Information Extraction Techniques", Symposium on Significant Results Obtained from the Earth Resources Technology Satellite, Vol. 1, Sec. B, NASA SP-327.

Murray, W. L. and J. G. Jurica (1970): "The Atmospheric Effect in the Remote Sensing of Earth Reflectivities" LARS Information Note 110273 Purdue Univ.

NASA-JSC (1972): Ground Truth Data for Test Sites SL-2. MSC-05531 L. B. Johnson Space Center, Houston, Texas.

NASA-JSC. (1973): Skylab Instrumentation Calibration Data. MSC-07744 Johnson Space Center, Houston, Texas.

NASA-JSC (1974): "Sensor Performance Report Vol. III (S192) Engineering Baseline, SL2 and 3 Evaluation" MSC-05528, L. B. Johnson Space Center Houston, Texas.

NASA-JSC (1974): Ground Truth Data for Test Sites (SL-3), MSC-05537, L. B. Johnson Space Center, Houston, Texas.

Plass, G. N. and G. W. Kattawar, (1968): Calculations of Reflected and Transmitted Radiance for Earth's Atmosphere. Ap. Op. 7.6.

Selby, J. E. A. and R. A. McClatchey, (1972): Atmospheric Transmittance from 0.25 to 28.5 μm: Computer Code LOWTRAN 2. AFCRL Environmental Research Papers, No. 427, AFCRL 72-0745.

State of California, The Resources Agency, Geologic Map of California Areas Sheet, SM Salton Sea Sheet, 1:250,000, Compilation by Charles W. Jennings, 1967.

State of California, SM Santa Anna Sheet, 1:250,000, Compilation by Thomas H. Rogers, 1965, United States Geological Survey, Salton Sink, California, 1:500,000, reprinted 1921, California State Conservation Service.

Thekaekara, M. P. (ed), (1970): The Solar Constant and the Solar Spectrum Measured from a Research Aircraft. NASA TR R-351, Goddard Space Flight Center, Greenbelt, Maryland.

United States Geological Survey, NK 12-Great Salt Lake, NK11-Owhee River, NJ12-Grand Canyon, 1:1,000,000, 1959.

University of Utah, College of Mines and Mineral Industry, Northwestern Utah, 1:250,000, Compiled by W. L. Stokes.

University of Utah, Geology Department.

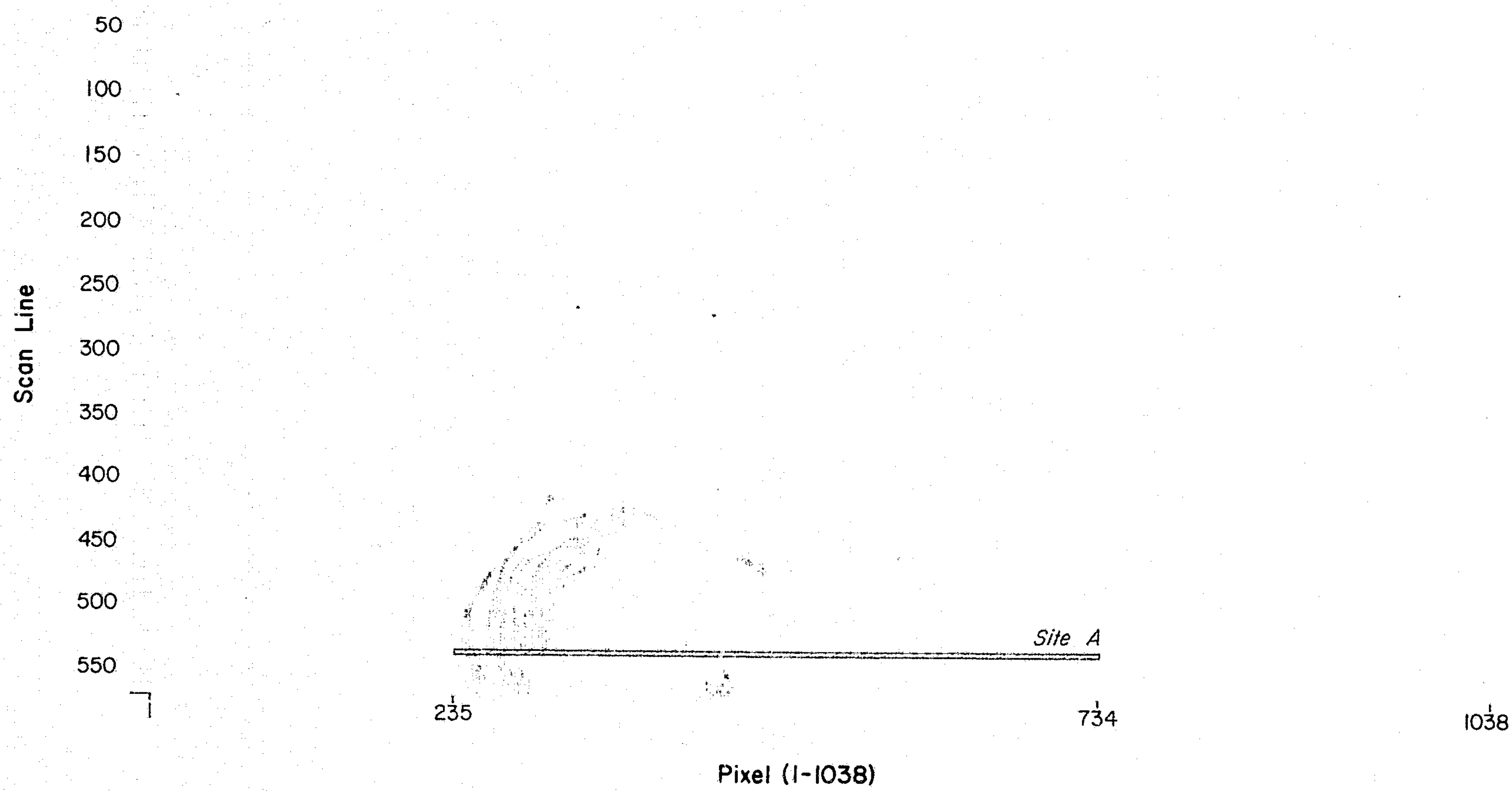

Figure A.1 Processed Image Matrix for Site A (See Text)

ORIGINAL PAGE IS OF POOR QUALITY

****

SCAN LINE	IHOUR	IMIN	SECONDS	SUBSAT LAT		SUB SAT LONG				SUN ANGLE			FIRST PIXEL LAT			LONG
10	17	57	35.2062	41	0	66	-114	20	223	62	20	88	41	13	35 -114	0 80
20	17	57	35.3118	41	0	14	-114	20	120	62	20	186	41	12	221 -113	59 213
30	17	57	35.4176	40	59	203	-114	20	16	62	21	43	41	12	168 -113	59 105
40	17	57	35.5233	40	59	146	-114	19	143	62	21	151	41	12	109 -113	58 228
50	17	57	35.6287	40	59	94	-114	19	39	62	22	8	41	12	55 -113	58 121
60	17	57	35.7336	40	59	47	-114	18	187	62	22	96	41	12	7 -113	58 26
70	17	57	35.8392	40	58	236	-114	18	83	62	22	193	41	11	194 -113	57 159
80	17	57	35.9449	40	58	184	-114	17	220	62	23	51	41	11	140 -113	57 53
90	17	57	36.0506	40	58	127	-114	17	106	62	23	158	41	11	81 -113	56 176
100	17	57	36.1561	40	58	75	-114	17	3	62	24	16	41	11	28 -113	56 70
110	17	57	36.2615	40	58	23	-114	16	140	62	24	113	41	10	215 -113	55 205
120	17	57	36.3674	40	57	217	-114	16	47	62	24	201	41	10	167 -113	55 110
130	17	57	36.4720	40	57	165	-114	15	184	62	25	58	41	10	114 -113	55 5
140	17	57	36.5777	40	57	113	-114	15	81	62	25	155	41	10	61 -113	54 140
150	17	57	36.6834	40	57	56	-114	14	208	62	26	23	41	10	3 -113	54 24
160	17	57	36.7889	40	57	4	-114	14	105	62	26	120	41	9	190 -113	53 160
170	17	57	36.8947	40	56	198	-114	14	12	62	26	208	41	9	142 -113	53 66
180	17	57	37.0003	40	56	146	-114	13	149	62	27	65	41	9	89 -113	52 202
190	17	57	37.1051	40	56	94	-114	13	46	62	27	163	41	9	37 -113	52 98
200	17	57	37.2108	40	56	37	-114	12	172	62	28	30	41	8	219 -113	51 224
210	17	57	37.3162	40	55	225	-114	12	69	62	28	120	41	8	166 -113	51 120
220	17	57	37.4110	40	55	170	-114	11	217	62	28	215	41	8	118 -113	51 27
230	17	57	37.5272	40	55	122	-114	11	103	62	29	83	41	8	57 -113	50 146
240	17	57	37.6326	40	55	70	-114	11	0	62	29	180	41	8	1 -113	50 36
250	17	57	37.7381	40	55	18	-114	10	137	62	30	38	41	7	185 -113	49 167
260	17	57	37.8439	40	54	211	-114	10	44	62	30	126	41	7	134 -113	49 67
270	17	57	37.9495	40	54	159	-114	9	181	62	30	223	41	7	79 -113	48 198
280	17	57	38.0552	40	54	107	-114	9	78	62	31	81	41	7	24 -113	48 89
290	17	57	38.1600	40	54	50	-114	8	205	62	31	187	41	6	203 -113	47 211
300	17	57	38.2664	40	53	238	-114	8	101	62	32	46	41	6	148 -113	47 101
310	17	57	38.3713	40	53	191	-114	8	9	62	32	133	41	6	99 -113	47 4
320	17	57	38.4769	40	53	140	-114	7	146	62	32	231	41	6	44 -113	46 136
330	17	57	38.5819	40	53	83	-114	7	33	62	33	97	41	5	224 -113	46 18
340	17	57	38.6877	40	53	36	-114	6	180	62	33	186	41	5	175 -113	45 160
350	17	57	38.7933	40	52	224	-114	6	77	62	34	43	41	5	121 -113	45 53
360	17	57	38.8990	40	52	172	-114	5	214	62	34	141	41	5	67 -113	44 186
370	17	57	39.0047	40	52	115	-114	5	101	62	35	8	41	5	7 -113	44 68
380	17	57	39.1102	40	52	63	-114	4	238	62	35	106	41	4	193 -113	43 201
390	17	57	39.2156	40	52	11	-114	4	135	62	35	203	41	4	139 -113	43 94
400	17	57	39.3205	40	51	204	-114	4	43	62	36	51	41	4	91 -113	42 238
410	17	57	39.4261	40	51	152	-114	3	180	62	36	148	41	4	37 -113	42 132
420	17	57	39.5318	40	51	100	-114	3	77	62	37	6	41	3	224 -113	42 25
430	17	57	39.6375	40	51	43	-114	2	204	62	37	113	41	3	165 -113	41 148
440	17	57	39.7430	40	50	231	-114	2	101	62	37	211	41	3	112 -113	41 42
450	17	57	39.8478	40	50	184	-114	2	9	62	38	58	41	3	64 -113	40 187
460	17	57	39.9534	.40	50	132	-114	1	146	62	38	156	41	3	10 -113	40 81
470	17	57	40.0592	40	50	80	-114	1	43	62	39	13	41	2	197 -113	39 215
480	17	57	40.1649	40	50	23	-114	0	170	62	39	121	41	2	139 -113	39 99
490	17	57	40.2703	40	49	211	-114	0	67	62	39	218	41	2	86 -113	38 233
500	17	57	40.3758	40	49	159	-113	59	205	62	40	75	41	2	33 -113	38 127
510	17	57	40.4816	40	49	112	-113	59	112	62	40	163	41	1	225 -113	38 33
520	17	57	40.5863	40	49	60	-113	59	10	62	41	20	41	1	172 -113	37 167
530	17	57	40.6920	40	49	8	-113	58	147	62	41	118	41	1	119 -113	37 62
540	17	57	40.7977	40	48	190	-113	58	34	62	41	225	41	1	61 -113	36 186
550	17	57	40.9031	40	48	138	-113	57	171	62	42	83	41	1	8 -113	36 81

Table A.1 Ephemeris Data for Site A

DATA FOR SCAN LINE NUMBER 535

PIXEL /DATA FOR SDO(S) NUMBER/	1	3	5	7	9	11	13	17	18	19	20	22
285	2.130E -2	7.504E -3	1.171E -2	1.406E -2	1.757E -2	1.655E -3	2.920E -4	5.527E -3	1.244E -2	1.037E -2	7.012E -3	9.361E -3
286	2.130E -2	7.504E -3	1.171E -2	1.406E -2	1.767E -2	1.880E -3	3.272E -4	6.002E -3	1.244E -2	1.037E -2	7.012E -3	9.361E -3
287	2.130E -2	7.504E -3	1.171E -2	1.406E -2	1.767E -2	1.794E -3	3.272E -4	6.192E -3	1.244E -2	1.037E -2	7.012E -3	9.361E -3
288	2.130E -2	7.504E -3	1.171E -2	1.406E -2	1.767E -2	1.643E -3	3.121E -4	5.749E -3	1.244E -2	1.037E -2	7.012E -3	9.361E -3
289	1.911E -2	7.504E -3	1.171E -2	1.406E -2	1.767E -2	6.746E -4	1.714E -4	5.052E -3	1.244E -2	1.037E -2	5.545E -3	9.361E -3
290	1.894E -2	7.504E -3	1.171E -2	1.406E -2	1.767E -2	5.024E -4	1.714E -4	3.849E -3	1.244E -2	1.037E -2	4.521E -3	9.361E -3
291	1.600E -2	7.504E -3	1.171E -2	1.406E -2	1.767E -2	8.898E -4	2.066E -4	2.645E -3	1.244E -2	6.644E -3	3.691E -3	9.361E -3
292	1.659E -2	7.504E -3	1.171E -2	1.406E -2	1.418E -2	1.127E -3	2.066E -4	3.405E -3	1.244E -2	7.585E -3	4.162E -3	9.361E -3
293	2.054E -2	7.504E -3	1.171E -2	1.406E -2	1.767E -2	1.708E -3	2.569E -4	3.088E -3	1.244E -2	6.235E -3	4.245E -3	9.361E -3
294	2.130E -2	7.504E -3	1.171E -2	1.406E -2	1.767E -2	1.729E -3	2.669E -4	3.912E -3	1.244E -2	6.563E -3	4.964E -3	9.361E -3
295	1.852E -2	7.504E -3	1.171E -2	1.406E -2	1.767E -2	2.009E -3	3.021E -4	5.369E -3	1.244E -2	1.037E -2	7.012E -3	9.361E -3
296	1.869E -2	7.504E -3	1.171E -2	1.406E -2	1.767E -2	2.009E -3	3.674E -4	5.876E -3	1.244E -2	1.037E -2	7.012E -3	9.361E -3
297	1.424E -2	7.504E -3	1.171E -2	1.406E -2	1.767E -2	1.751E -3	3.523E -4	6.287E -3	1.244E -2	1.037E -2	4.964E -3	9.361E -3
298	1.441E -2	7.504E -3	1.171E -2	1.406E -2	1.028E -2	9.759E -4	2.770E -4	6.319E -3	1.244E -2	1.037E -2	5.767E -3	9.361E -3
299	1.600E -2	7.504E -3	1.171E -2	1.406E -2	8.329E -3	5.239E -4	2.016E -4	5.559E -3	1.244E -2	1.037E -2	3.553E -3	9.361E -3
300	1.264E -2	7.504E -3	1.171E -2	1.406E -2	1.425E -2	1.579E -3	3.071E -4	5.401E -3	1.244E -2	1.037E -2	4.162E -3	9.361E -3
301	1.390E -2	7.504E -3	1.171E -2	1.251E -2	9.166E -3	8.683E -4	2.569E -4	3.373E -3	1.058E -2	6.358E -3	2.114E -3	9.361E -3
302	1.617E -2	7.504E -3	1.171E -2	1.406E -2	7.981E -3	3.517E -4	1.915E -4	1.695E -3	1.244E -2	3.495E -3	1.284E -3	9.361E -3
303	1.701E -2	7.504E -3	1.171E -2	1.406E -2	8.190E -3	1.795E -4	1.765E -4	2.106E -3	1.156E -2	3.781E -3	1.311E -3	9.361E -3
304	1.491E -2	7.504E -3	1.171E -2	1.406E -2	8.050E -3	7.192E -5	1.212E -4	1.124E -3	1.244E -2	2.268E -3	9.516E -4	9.361E -3
305	1.684E -2	7.504E -3	1.171E -2	1.406E -2	7.981E -3	3.087E -4	1.765E -4	6.493E -4	1.244E -2	1.695E -3	8.133E -4	9.361E -3
306	1.743E -2	7.504E -3	1.171E -2	1.406E -2	7.562E -3	1.150E -4	1.363E -4	1.283E -3	1.244E -2	2.718E -3	1.118E -3	9.361E -3
307	1.642E -2	7.504E -3	1.171E -2	1.406E -2	7.423E -3	1.150E -4	1.162E -4	7.444E -4	1.244E -2	1.573E -3	1.118E -3	9.361E -3
308	1.710E -2	7.504E -3	1.171E -2	1.406E -2	7.632E -3	2.872E -4	1.262E -4	5.226E -4	1.244E -2	1.123E -3	1.062E -3	9.361E -3
309	1.701E -2	7.504E -3	1.171E -2	1.406E -2	6.796E -3	1.795E -4	1.011E -4	1.156E -3	1.244E -2	2.227E -3	1.201E -3	9.361E -3
310	1.659E -2	7.504E -3	1.171E -2	1.196E -2	6.377E -3	1.795E -4	8.604E -5	6.810E -4	1.244E -2	1.532E -3	1.118E -3	9.361E -3
311	1.542E -2	7.504E -3	1.171E -2	1.218E -2	6.377E -3	1.580E -4	1.363E -4	6.493E -4	1.244E -2	1.286E -3	1.062E -3	9.361E -3
312	1.550E -2	7.504E -3	1.171E -2	1.179E -2	5.680E -3	1.150E -4	1.162E -4	8.711E -4	1.244E -2	1.818E -3	1.035E -3	9.361E -3
313	1.449E -2	7.504E -3	1.171E -2	1.107E -2	5.610E -3	1.795E -4	9.609E -5	7.760E -4	1.244E -2	1.532E -3	1.201E -3	9.361E -3
314	1.415E -2	7.504E -3	1.171E -2	1.118E -2	5.262E -3	9.344E -5	9.609E -5	9.344E -4	1.244E -2	1.409E -3	1.145E -3	9.361E -3
315	1.474E -2	7.504E -3	1.171E -2	1.074E -2	5.123E -3	1.150E -4	8.101E -5	8.394E -4	1.107E -2	1.327E -3	8.963E -4	9.361E -3
316	1.449E -2	7.504E -3	1.171E -2	1.046E -2	4.844E -3	1.365E -4	8.101E -5	7.127E -4	1.097E -2	1.082E -3	1.062E -3	9.361E -3
317	1.390E -2	7.504E -3	1.171E -2	1.057E -2	4.704E -3	1.150E -4	1.162E -4	8.394E -4	1.063E -2	1.164E -3	1.035E -3	9.361E -3
318	1.407E -2	7.504E -3	1.171E -2	1.057E -2	4.356E -3	1.580E -4	1.112E -4	6.810E -4	1.072E -2	1.164E -3	1.145E -3	9.361E -3
319	1.357E -2	7.504E -3	1.171E -2	1.040E -2	4.147E -3	1.580E -4	9.106E -5	6.810E -4	1.077E -2	1.205E -3	1.062E -3	9.361E -3
320	1.382E -2	7.504E -3	1.171E -2	9.848E -3	4.356E -3	7.192E -5	1.162E -4	7.127E -4	1.058E -2	1.164E -3	1.090E -3	9.361E -3
321	1.390E -2	7.504E -3	1.171E -2	1.029E -2	4.565E -3	9.344E -5	1.011E -4	5.226E -4	1.033E -2	1.164E -3	1.118E -3	9.361E -3
322	1.506E -2	7.504E -3	1.171E -2	9.903E -3	4.565E -3	1.365E -4	8.101E -5	7.127E -4	1.056E -2	1.327E -3	1.201E -3	9.361E -3
323	1.483E -2	7.504E -3	1.171E -2	1.018E -2	4.983E -3	5.040E -5	7.097E -5	4.910E -4	1.058E -2	1.327E -3	1.228E -3	9.361E -3
324	1.457E -2	7.504E -3	1.171E -2	1.007E -2	4.983E -3	5.040E -5	7.599E -5	6.493E -4	1.058E -2	1.368E -3	1.118E -3	9.361E -3
325	1.533E -2	7.504E -3	1.171E -2	1.051E -2	5.123E -3	9.344E -5	8.604E -5	6.493E -4	1.068E -2	1.450E -3	1.145E -3	9.361E -3
326	1.575E -2	7.504E -3	1.171E -2	1.062E -2	5.053E -3	9.344E -5	8.604E -5	8.394E -4	1.097E -2	1.491E -3	1.145E -3	9.361E -3
327	1.609E -2	7.504E -3	1.171E -2	1.101E -2	5.401E -3	1.150E -4	7.599E -5	7.444E -4	1.244E -2	1.532E -3	1.062E -3	9.361E -3
328	1.684E -2	7.504E -3	1.171E -2	1.140E -2	5.401E -3	1.795E -4	9.106E -5	6.810E -4	1.244E -2	1.286E -3	1.173E -3	9.361E -3
329	1.567E -2	7.504E -3	1.171E -2	1.140E -2	5.959E -3	1.365E -4	8.604E -5	5.226E -4	1.244E -2	1.409E -3	1.256E -3	9.361E -3
330	1.609E -2	7.504E -3	1.171E -2	1.129E -2	5.192E -3	1.580E -4	9.609E -5	5.226E -4	1.244E -2	1.368E -3	1.173E -3	9.361E -3
331	1.600E -2	7.504E -3	1.171E -2	1.096E -2	5.192E -3	1.580E -4	8.604E -5	8.711E -4	1.244E -2	1.450E -3	1.090E -3	9.361E -3
332	1.642E -2	7.504E -3	1.171E -2	1.101E -2	5.192E -3	1.795E -4	7.599E -5	8.711E -4	1.244E -2	1.532E -3	1.062E -3	9.361E -3
333	1.668E -2	7.504E -3	1.171E -2	1.146E -2	5.680E -3	2.226E -4	8.101E -5	6.177E -4	1.244E -2	1.532E -3	1.062E -3	9.361E -3
334	1.634E -2	7.504E -3	1.171E -2	1.135E -2	5.680E -3	2.441E -4	8.101E -5	7.760E -4	1.244E -2	1.491E -3	1.173E -3	9.361E -3
335	1.432E -2	7.504E -3	1.171E -2	1.179E -2	5.680E -3	2.441E -4	7.599E -5	6.810E -4	1.244E -2	1.409E -3	1.118E -3	9.361E -3

ORIGINAL PAGE IS OF POOR QUALITY

Table A.2 Calibrated S192 Radiances for Site A (Southern Salt Flats)

DATA FOR SCAN LINE NUMBER 535

PIXEL NUMBER/ DATA FOR SDO(S) 1	3	5	7	9	11	13	17	18	19	20	22
642 2.121E -2	7.504E -3	1.171E -2	1.406E -2	1.767E -2	1.234E -3	1.765E -4	4.387E -3	1.244E -2	8.076E -3	5.269E -3	9.361E -3
643 2.079E -2	7.504E -3	1.171E -2	1.406E -2	1.767E -2	1.234E -3	1.865E -4	4.355E -3	1.244E -2	8.117E -3	5.352E -3	9.361E -3
644 2.105E -2	7.504E -3	1.171E -2	1.406E -2	1.767E -2	1.277E -3	1.664E -4	4.355E -3	1.244E -2	8.239E -3	5.158E -3	9.361E -3
645 2.054E -2	7.504E -3	1.171E -2	1.406E -2	1.767E -2	1.234E -3	1.865E -4	4.514E -3	1.244E -2	8.403E -3	5.186E -3	9.361E -3
646 1.970E -2	7.504E [illegible]	1.171E -2	1.406E -2	1.767E -2	1.148E -3	1.765E -4	4.419E -3	1.244E -2	8.485E -3	5.020E -3	9.361E -3
647 2.079E -2	7.504E -3	1.171E -2	1.406E -2	1.767E -2	1.170E -3	1.915E -4	4.229E -3	1.244E -2	8.321E -3	5.047E -3	9.361E -3
648 2.037E -2	7.504E -3	1.171E -2	1.406E -2	1.767E -2	1.127E -3	1.614E -4	4.387E -3	1.244E -2	8.280E -3	5.213E -3	9.361E -3
649 2.029E -2	7.504E -3	1.171E -2	1.406E -2	1.767E -2	1.191E -3	1.865E -4	4.197E -3	1.244E -2	7.994E -3	5.158E -3	9.361E -3
650 2.130E -2	7.504E -3	1.171E -2	1.406E -2	1.767E -2	1.277E -3	1.614E -4	4.039E -3	1.244E -2	8.117E -3	5.407E -3	9.361E -3
651 2.037E -2	7.504E -3	1.171E -2	1.406E -2	1.767E -2	1.213E -3	1.765E -4	4.229E -3	1.244E -2	8.199E -3	5.324E -3	9.361E -3
652 2.071E -2	7.504E -3	1.171E -2	1.406E -2	1.767E -2	1.191E -3	1.765E -4	4.609E -3	1.244E -2	8.362E -3	5.296E -3	9.361E -3
653 2.113E -2	7.504E -3	1.171E -2	1.406E -2	1.767E -2	1.170E -3	2.217E -4	4.197E -3	1.244E -2	8.199E -3	5.158E -3	9.361E -3
654 2.071E -2	7.504E -3	1.171E -2	1.406E -2	1.767E -2	1.170E -3	2.066E -4	4.229E -3	1.244E -2	8.403E -3	5.130E -3	9.361E -3
655 1.869E -2	7.504E -3	1.171E -2	1.406E -2	1.767E -2	1.213E -3	2.167E -4	4.355E -3	1.244E -2	8.239E -3	5.186E -3	9.361E -3
656 1.911E -2	7.504E -3	1.171E -2	1.406E -2	1.767E -2	1.234E -3	2.116E -4	4.387E -3	1.244E -2	8.526E -3	5.352E -3	9.361E -3
657 1.869E -2	7.504E -3	1.171E -2	1.406E -2	1.767E -2	1.170E -3	2.016E -4	4.450E -3	1.244E -2	1.037E -2	5.186E -3	9.361E -3
658 1.911E -2	7.504E -3	1.171E -2	1.406E -2	1.767E -2	1.148E -3	2.016E -4	4.292E -3	1.244E -2	8.158E -3	5.130E -3	9.361E -3
659 2.029E -2	7.504E -3	1.171E -2	1.406E -2	1.767E -2	1.148E -3	2.167E -4	4.229E -3	1.244E -2	8.158E -3	4.992E -3	9.361E -3
660 1.987E -2	7.504E -3	1.171E -2	1.406E -2	1.767E -2	1.234E -3	2.016E -4	4.229E -3	1.244E -2	8.199E -3	4.881E -3	9.361E -3
661 2.071E -2	7.504E -3	1.171E -2	1.406E -2	1.767E -2	1.234E -3	2.267E -4	4.514E -3	1.244E -2	7.667E -3	5.020E -3	9.361E -3
662 2.079E -2	7.504E -3	1.171E -2	1.406E -2	1.767E -2	1.234E -3	1.865E -4	4.419E -3	1.244E -2	7.912E -3	5.075E -3	9.361E -3
663 2.130E -2	7.504E -3	1.171E -2	1.406E -2	1.767E -2	1.191E -3	1.765E -4	4.292E -3	1.244E -2	8.321E -3	5.047E -3	9.361E -3
664 2.105E -2	7.504E -3	1.171E -2	1.406E -2	1.767E -2	1.363E -3	1.765E -4	4.292E -3	1.244E -2	8.239E -3	5.075E -3	9.361E -3
665 2.020E -2	7.504E -3	1.171E -2	1.406E -2	1.767E -2	1.299E -3	1.865E -4	4.355E -3	1.244E -2	7.994E -3	5.324E -3	9.361E -3
666 2.130E -2	7.504E -3	1.171E -2	1.406E -2	1.767E -2	1.256E -3	1.714E -4	4.355E -3	1.244E -2	8.076E -3	5.352E -3	9.361E -3
667 2.063E -2	7.504E -3	1.171E -2	1.406E -2	1.767E -2	1.299E -3	1.865E -4	4.545E -3	1.244E -2	8.239E -3	5.435E -3	9.361E -3
668 2.012E -2	7.504E -3	1.171E -2	1.406E -2	1.767E -2	1.363E -3	1.915E -4	4.799E -3	1.244E -2	8.158E -3	5.601E -3	9.361E -3
669 1.978E -2	7.504E -3	1.171E -2	1.406E -2	1.767E -2	1.320E -3	2.167E -4	4.830E -3	1.244E -2	8.362E -3	5.269E -3	9.361E -3
670 1.936E -2	7.504E -3	1.171E -2	1.406E -2	1.767E -2	1.342E -3	2.066E -4	4.609E -3	1.244E -2	1.037E -2	5.241E -3	9.361E -3
671 1.936E -2	7.504E -3	1.171E -2	1.406E -2	1.767E -2	1.385E -3	2.167E -4	4.482E -3	1.244E -2	8.444E -3	5.213E -3	9.361E -3
672 1.903E -2	7.504E -3	1.171E -2	1.406E -2	1.767E -2	1.363E -3	1.865E -4	4.482E -3	1.244E -2	8.035E -3	5.269E -3	9.361E -3
673 1.970E -2	7.504E -3	1.171E -2	1.406E -2	1.767E -2	1.342E -3	1.664E -4	4.514E -3	1.244E -2	7.871E -3	5.186E -3	9.361E -3
674 1.852E -2	7.504E -3	1.171E -2	1.406E -2	1.767E -2	1.320E -3	1.865E -4	4.450E -3	1.244E -2	7.912E -3	5.324E -3	9.361E -3
675 1.894E -2	7.504E -3	1.171E -2	1.406E -2	1.767E -2	1.234E -3	1.614E -4	4.767E -3	1.244E -2	7.790E -3	5.186E -3	9.361E -3
676 1.920E -2	7.504E -3	1.171E -2	1.406E -2	1.767E -2	1.277E -3	1.915E -4	4.292E -3	1.244E -2	7.667E -3	5.186E -3	9.361E -3
677 1.886E -2	7.504E -3	1.171E -2	1.406E -2	1.767E -2	1.385E -3	1.915E -4	4.419E -3	1.244E -2	7.871E -3	5.047E -3	9.361E -3
678 1.936E -2	7.504E -3	1.171E -2	1.406E -2	1.767E -2	1.256E -3	1.765E -4	4.387E -3	1.244E -2	7.708E -3	4.992E -3	9.361E -3
679 1.962E -2	7.504E -3	1.171E -2	1.406E -2	1.767E -2	1.277E -3	1.915E -4	4.419E -3	1.244E -2	7.994E -3	5.020E -3	9.361E -3
680 1.995E -2	7.504E -3	1.171E -2	1.406E -2	1.767E -2	1.385E -3	1.915E -4	4.514E -3	1.244E -2	7.953E -3	4.964E -3	9.361E -3
681 1.911E -2	7.504E -3	1.171E -2	1.406E -2	1.767E -2	1.299E -3	1.815E -4	4.260E -3	1.244E -2	8.239E -3	5.158E -3	9.361E -3
682 1.777E -2	7.504E -3	1.171E -2	1.406E -2	1.767E -2	1.320E -3	1.714E -4	4.197E -3	1.244E -2	7.953E -3	5.047E -3	9.361E -3
683 1.894E -2	7.504E -3	1.171E -2	1.406E -2	1.767E -2	1.256E -3	1.815E -4	4.102E -3	1.244E -2	7.912E -3	5.103E -3	9.361E -3
684 1.952E -2	7.504E -3	1.171E -2	1.406E -2	1.767E -2	1.148E -3	1.915E -4	4.134E -3	1.244E -2	7.790E -3	4.771E -3	9.361E -3
685 1.952E -2	7.504E -3	1.171E -2	1.406E -2	1.767E -2	1.213E -3	1.966E -4	4.197E -3	1.244E -2	7.871E -3	4.771E -3	9.361E -3
686 1.970E -2	7.504E -3	1.171E -2	1.406E -2	1.767E -2	1.256E -3	2.066E -4	4.197E -3	1.244E -2	7.749E -3	4.826E -3	9.361E -3
687 1.970E -2	7.504E -3	1.171E -2	1.406E -2	1.767E -2	1.385E -3	1.765E -4	4.039E -3	1.244E -2	7.708E -3	4.854E -3	9.361E -3
688 1.886E -2	7.504E -3	1.171E -2	1.406E -2	1.767E -2	[illegible]99E -3	1.664E -4	4.355E -3	1.244E -2	7.749E -3	4.937E -3	9.361E -3
689 1.886E -2	7.504E -3	1.171E -2	1.406E -2	1.767E -2	1.127E -3	1.514E -4	4.134E -3	1.244E -2	7.585E -3	4.964E -3	9.361E -3
690 1.920E -2	7.504E -3	1.171E -2	1.406E -2	1.767E -2	1.170E -3	1.815E -4	4.134E -3	1.244E -2	7.462E -3	4.937E -3	9.361E -3
691 1.869E -2	7.504E -3	1.171E -2	1.406E -2	1.767E -2	1.191E -3	1.915E -4	3.944E -3	1.244E -2	7.994E -3	4.854E -3	9.361E -3
692 1.878E -2	7.504E -3	1.171E -2	1.406E -2	1.767E -2	1.170E -3	2.066E -4	3.912E -3	1.244E -2	7.830E -3	4.964E -3	9.361E -3

Table A.3 Calibrated S192 Radiances for Site A (Northern Salt Flats)

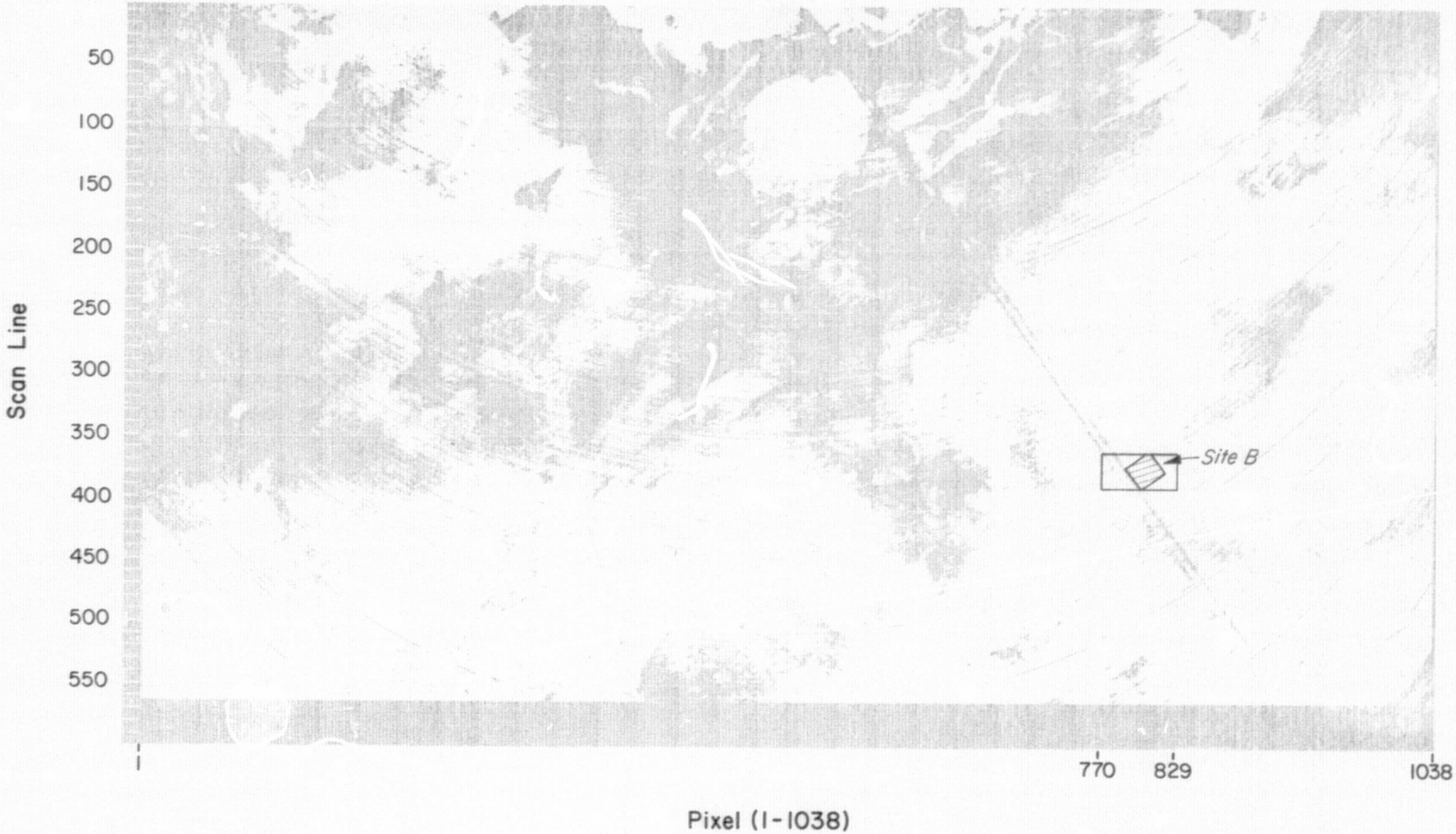

Figure A.2 Processed Image Matrix for Site B (See Text)

ORIGINAL PAGE IS OF POOR QUALITY

0 0 VERSION 0.0 ( ) 0/ 0/ 0 PAGE 2

SCAN LINE	IHOUR	IMIN	SECONDS	SUBSAT LAT			SUB SAT LONG			SUN ANGLE			FIRST PIXEL LAT			LONG		
10	17	57	41.2093	40	47	232	-113	56	123	62	43	116	41	0	99	-113	35	26
20	17	57	41.3150	40	47	190	-113	56	21	62	43	214	41	0	46	-113	34	160
30	17	57	41.4197	40	47	123	-113	55	149	62	44	80	40	59	229	-113	34	46
40	17	57	41.5252	40	47	71	-113	55	46	62	44	178	40	59	176	-113	33	180
50	17	57	41.6307	40	47	19	-113	54	183	62	45	35	40	59	123	-113	33	75
60	17	57	41.7366	40	46	211	-113	54	91	62	45	124	40	59	75	-113	32	220
70	17	57	41.8424	40	46	159	-113	53	228	62	45	221	40	59	21	-113	32	115
80	17	57	41.9481	40	46	102	-113	53	115	62	46	83	40	58	203	-113	31	239
90	17	57	42.0535	40	46	50	-113	53	12	62	46	186	40	58	150	-113	31	134
100	17	57	42.1590	40	45	238	-113	52	150	62	47	43	40	58	97	-113	31	29
110	17	57	42.2638	40	45	191	-113	52	58	62	47	131	40	58	49	-113	30	174
120	17	57	42.3699	40	45	133	-113	51	185	62	47	238	40	57	230	-113	30	59
130	17	57	42.4754	40	45	81	-113	51	82	62	49	96	40	57	177	-113	29	193
140	17	57	42.5803	40	45	34	-113	50	231	62	48	183	40	57	129	-113	29	88
150	17	57	42.6859	40	44	222	-113	50	128	62	49	41	40	57	75	-113	28	233
160	17	57	42.7916	40	44	170	-113	50	26	62	49	138	40	57	21	-113	28	127
170	17	57	42.8973	40	44	112	-113	49	153	62	50	6	40	56	202	-113	28	10
180	17	57	43.0028	40	44	60	-113	49	50	62	50	103	40	56	149	-113	27	145
190	17	57	43.1082	40	44	8	-113	48	188	62	50	201	40	56	94	-113	27	39
200	17	57	43.2132	40	43	201	-113	48	96	62	51	48	40	56	46	-113	26	184
210	17	57	43.3189	40	43	149	-113	47	234	62	51	145	40	55	232	-113	26	78
220	17	57	42.4246	40	43	91	-113	47	121	62	52	13	40	55	172	-113	25	201
230	17	57	43.5301	40	43	39	-113	47	18	62	52	110	40	55	118	-113	25	94
240	17	57	43.6356	40	42	226	-113	46	156	62	52	208	40	55	63	-113	24	228
250	17	57	43.7414	40	42	180	-113	46	64	62	53	56	40	55	14	-113	24	132
260	17	57	43.8460	40	42	127	-113	45	202	62	53	153	40	54	159	-113	24	25
270	17	57	43.9517	40	42	75	-113	45	100	62	54	10	40	54	144	-113	23	159
280	17	57	44.0574	40	42	17	-113	44	227	62	54	118	40	54	83	-113	23	41
290	17	57	44.1629	40	41	205	-113	44	125	62	54	215	40	54	28	-113	22	174
300	17	57	44.2684	40	41	153	-113	44	22	62	55	73	40	53	212	-113	22	67
310	17	57	44.3742	40	41	106	-113	43	170	62	55	160	40	53	162	-113	21	210
320	17	57	44.4798	40	41	53	-113	43	68	62	56	18	40	53	107	-113	21	102
330	17	57	44.5945	40	41	1	-113	42	206	62	56	115	40	53	51	-113	20	235
340	17	57	44.6903	40	40	183	-113	42	93	62	56	223	40	52	228	-113	20	116
350	17	57	44.7957	40	40	131	-113	41	231	62	57	80	40	52	172	-113	20	8
360	17	57	44.9015	40	40	84	-113	41	139	62	57	169	40	52	124	-113	19	154
370	17	57	45.0072	40	40	31	-113	41	36	62	58	26	40	52	69	-113	19	50
380	17	57	45.1129	40	39	219	-113	40	174	62	59	124	40	52	15	-113	18	186
390	17	57	45.2176	40	39	162	-113	40	62	62	58	230	40	51	196	-113	18	73
400	17	57	45.3231	40	39	109	-113	39	200	62	59	83	40	51	142	-113	17	208
410	17	57	45.4285	40	39	57	-113	39	98	62	59	185	40	51	88	-113	17	104
420	17	57	45.5344	40	39	9	-113	39	6	63	0	33	40	51	39	-113	17	9
430	17	57	45.6400	40	38	197	-113	38	143	63	0	131	40	50	225	-113	16	145
440	17	57	45.7457	40	38	144	-113	38	41	63	0	228	40	50	171	-113	16	40
450	17	57	45.8514	40	38	87	-113	37	169	63	1	96	40	50	111	-113	15	165
460	17	57	45.9569	40	38	34	-113	37	67	63	1	193	40	50	57	-113	15	59
470	17	57	46.0617	40	37	227	-113	36	215	63	2	41	40	50	9	-113	14	205
480	17	57	46.1673	40	37	175	-113	36	113	63	2	138	40	49	194	-113	14	100
490	17	57	46.2730	40	37	122	-113	36	11	63	2	236	40	49	140	-113	13	235
500	17	57	46.3787	40	37	65	-113	35	139	63	3	103	40	49	80	-113	13	118
510	17	57	46.4842	40	37	12	-113	35	36	63	3	200	40	49	26	-113	13	12
520	17	57	46.5897	40	36	200	-113	34	174	63	4	53	40	48	212	-113	12	147
520	17	57	46.6945	40	36	152	-113	34	83	63	4	145	40	48	163	-113	12	52
540	17	57	46.8001	40	36	100	-113	33	221	63	5	3	40	48	109	-113	11	185
550	17	57	46.9058	40	36	48	-113	33	119	63	5	100	40	48	55	-113	11	80

Table A.4 Ephemeris Data for Site B

ORIGINAL PAGE IS
OF POOR QUALITY

DATA FOR SCAN LINE NUMBER 376

PIXEL /DATA FOR SDO(S)

NUMBER/	1	3	5	7	9	11	13	17	18	19	20	22
770	1.642E -2	7.504E -3	1.171E -2	-8.304E -5	1.314E -2	2.138E -3	5.181E -4	4.862E -3	1.244E -2	6.931E -3	4.632E -3	9.361E -3
771	1.642E -2	7.504E -3	1.171E -2	-8.304E -5	1.398E -2	2.246E -3	5.382E -4	5.147E -3	1.244E -2	7.012E -3	4.909E -3	9.361E -3
772	1.491E -2	7.504E -3	1.171E -2	-8.304E -5	1.321E -2	2.181E -3	4.930E -4	4.862E -3	1.244E -2	7.176E -3	4.537E -3	9.361E -3
773	1.457E -2	7.504E -3	1.171E -2	1.406E -2	1.342E -2	2.267E -3	4.930E -4	4.704E -3	1.244E -2	6.972E -3	4.771E -3	9.361E -3
774	1.491E -2	7.504E -3	1.171E -2	1.406E -2	1.286E -2	2.246E -3	4.980E -4	4.672E -3	1.244E -2	6.808E -3	4.771E -3	9.361E -3
775	1.508E -2	7.504E -3	1.171E -2	1.406E -2	1.307E -2	2.203E -3	4.980E -4	4.799E -3	1.244E -2	7.094E -3	4.937E -3	9.361E -3
776	1.449E -2	7.504E -3	1.171E -2	1.406E -2	1.342E -2	2.181E -3	4.980E -4	4.609E -3	1.244E -2	6.767E -3	4.909E -3	9.361E -3
777	1.407E -2	7.504E -3	1.171E -2	1.406E -2	1.300E -2	2.246E -3	4.930E -4	4.640E -3	1.122E -2	6.972E -3	4.909E -3	9.361E -3
778	1.310E -2	7.504E -3	1.171E -2	-8.304E -5	1.300E -2	2.095E -3	4.930E -4	4.419E -3	1.244E -2	2.718E -3	4.604E -3	9.361E -3
779	1.357E -2	7.504E -3	1.171E -2	-8.304E -5	1.258E -2	2.074E -3	4.628E -4	4.609E -3	1.112E -2	6.563E -3	4.383E -3	9.361E -3
780	1.256E -2	7.504E -3	1.171E -2	-8.304E -5	1.223E -2	2.074E -3	4.578E -4	4.672E -3	1.244E -2	6.235E -3	4.411E -3	9.361E -3
781	1.305E -2	7.504E -3	1.171E -2	-8.304E -5	1.181E -2	1.945E -3	4.578E -4	4.197E -3	1.014E -2	6.031E -3	4.383E -3	9.361E -3
782	1.390E -2	7.504E -3	1.171E -2	1.262E -2	1.112E -2	1.923E -3	4.679E -4	4.292E -3	1.102E -2	6.563E -3	4.328E -3	9.361E -3
783	1.449E -2	7.504E -3	1.171E -2	1.273E -2	1.133E -2	2.009E -3	4.528E -4	4.229E -3	1.126E -2	6.317E -3	4.300E -3	9.361E -3
784	1.491E -2	7.504E -3	1.171E -2	1.406E -2	1.258E -2	2.074E -3	4.377E -4	4.545E -3	1.126E -2	6.154E -3	4.355E -3	9.361E -3
785	1.516E -2	7.504E -3	1.171E -2	1.406E -2	1.279E -2	2.160E -3	4.478E -4	4.482E -3	1.244E -2	6.522E -3	4.660E -3	9.361E -3
786	1.424E -2	7.504E -3	1.171E -2	1.312E -2	1.342E -2	2.138E -3	4.578E -4	4.704E -3	1.244E -2	6.685E -3	4.604E -3	9.361E -3
787	1.525E -2	7.504E -3	1.171E -2	-8.304E -5	1.258E -2	1.988E -3	4.478E -4	4.514E -3	1.244E -2	6.603E -3	4.549E -3	9.361E -3
788	1.525E -2	7.504E -3	1.171E -2	1.406E -2	1.230E -2	2.181E -3	4.930E -4	4.419E -3	1.244E -2	6.358E -3	4.743E -3	9.361E -3
789	1.298E -2	7.504E -3	1.171E -2	1.334E -2	1.237E -2	2.117E -3	4.930E -4	4.450E -3	1.244E -2	6.399E -3	4.632E -3	9.361E -3
790	1.239E -2	7.504E -3	1.171E -2	-8.304E -5	1.038E -2	1.988E -3	4.277E -4	4.229E -3	1.038E -2	6.113E -3	4.134E -3	9.361E -3
791	1.365E -2	7.504E -3	1.171E -2	1.223E -2	1.181E -2	1.901E -3	4.427E -4	4.229E -3	1.033E -2	5.745E -3	4.217E -3	9.361E -3
792	1.432E -2	7.504E -3	1.171E -2	-8.304E -5	1.126E -2	2.009E -3	3.975E -4	3.785E -3	1.069E -2	5.663E -3	4.383E -3	9.361E -3
793	1.457E -2	7.504E -3	1.171E -2	-8.304E -5	1.195E -2	2.052E -3	4.427E -4	3.975E -3	1.102E -2	6.031E -3	4.660E -3	9.361E -3
794	1.626E -2	7.504E -3	1.171E -2	1.406E -2	1.279E -2	1.988E -3	4.528E -4	4.609E -3	1.244E -2	6.644E -3	4.383E -3	9.361E -3
795	1.533E -2	7.504E -3	1.171E -2	-8.304E -5	1.286E -2	2.181E -3	4.679E -4	4.609E -3	1.244E -2	6.603E -3	4.494E -3	9.361E -3
796	1.525E -2	7.504E -3	1.171E -2	-8.304E -5	1.300E -2	2.224E -3	4.729E -4	4.514E -3	1.244E -2	6.522E -3	4.798E -3	9.361E -3
797	1.600E -2	7.504E -3	1.171E -2	-8.304E -5	1.286E -2	2.246E -3	4.578E -4	4.609E -3	1.244E -2	6.808E -3	4.632E -3	9.361E -3
798	1.600E -2	7.504E -3	1.171E -2	-8.304E -5	1.342E -2	2.246E -3	4.528E -4	4.672E -3	1.244E -2	7.012E -3	4.687E -3	9.361E -3
799	1.516E -2	7.504E -3	1.171E -2	1.406E -2	1.300E -2	2.267E -3	4.880E -4	4.577E -3	1.244E -2	6.972E -3	4.660E -3	9.361E -3
800	1.516E -2	7.504E -3	1.171E -2	1.406E -2	1.314E -2	2.160E -3	4.478E -4	4.482E -3	1.244E -2	6.644E -3	4.798E -3	9.361E -3
801	1.634E -2	7.504E -3	1.171E -2	1.406E -2	1.314E -2	2.267E -3	4.578E -4	4.545E -3	1.244E -2	6.563E -3	4.759E -3	9.361E -3
802	1.600E -2	7.504E -3	1.171E -2	-8.304E -5	1.321E -2	2.310E -3	4.779E -4	4.735E -3	1.244E -2	6.808E -3	4.964E -3	9.361E -3
803	1.642E -2	7.504E -3	1.171E -2	-8.304E -5	1.356E -2	2.267E -3	4.578E -4	4.799E -3	1.244E -2	7.135E -3	4.937E -3	9.361E -3
804	1.600E -2	7.504E -3	1.171E -2	-8.304E -5	1.321E -2	2.289E -3	4.779E -4	4.799E -3	1.244E -2	6.849E -3	4.854E -3	9.361E -3
805	1.592E -2	7.504E -3	1.171E -2	-8.304E -5	1.363E -2	2.181E -3	4.829E -4	4.640E -3	1.244E -2	7.421E -3	4.826E -3	9.361E -3
806	1.535E -2	7.504E -3	1.171E -2	1.406E -2	1.286E -2	2.181E -3	5.081E -4	4.767E -3	1.244E -2	7.462E -3	4.687E -3	9.361E -3
807	1.575E -2	7.504E -3	1.171E -2	1.406E -2	1.328E -2	2.246E -3	4.729E -4	4.767E -3	1.244E -2	7.176E -3	4.771E -3	9.361E -3
808	1.533E -2	7.504E -3	1.171E -2	1.406E -2	1.314E -2	2.246E -3	4.729E -4	4.799E -3	1.244E -2	7.012E -3	5.020E -3	9.361E -3
809	1.474E -2	7.504E -3	1.171E -2	-8.304E -5	1.384E -2	2.310E -3	4.930E -4	4.482E -3	1.244E -2	6.931E -3	4.932E -3	9.361E -3
810	1.592E -2	7.504E -3	1.171E -2	-8.304E -5	1.314E -2	2.310E -3	4.478E -4	4.672E -3	1.244E -2	7.299E -3	4.687E -3	9.361E -3
811	1.491E -2	7.504E -3	1.171E -2	-8.304E -5	1.335E -2	2.224E -3	4.779E -4	4.640E -3	1.244E -2	6.849E -3	4.909E -3	9.361E -3
812	1.407E -2	7.504E -3	1.171E -2	-8.304E -5	1.328E -2	2.246E -3	4.679E -4	4.830E -3	1.244E -2	6.767E -3	4.992E -3	9.361E -3
813	1.449E -2	7.504E -3	1.171E -2	1.406E -2	1.349E -2	2.117E -3	4.478E -4	4.830E -3	1.244E -2	6.808E -3	4.854E -3	9.361E -3
814	1.466E -2	7.504E -3	1.171E -2	1.368E -2	1.356E -2	2.203E -3	4.277E -4	4.609E -3	1.244E -2	6.808E -3	4.881E -3	9.361E -3
815	1.535E -2	7.504E -3	1.171E -2	1.406E -2	1.293E -2	2.203E -3	4.628E -4	4.514E -3	1.244E -2	6.603E -3	4.909E -3	9.361E -3
816	1.575E -2	7.504E -3	1.171E -2	-8.304E -5	1.293E -2	2.289E -3	5.131E -4	4.482E -3	1.244E -2	6.767E -3	4.964E -3	9.361E -3
817	1.558E -2	7.504E -3	1.171E -2	-8.304E -5	1.335E -2	2.353E -3	5.030E -4	4.862E -3	1.244E -2	7.094E -3	4.881E -3	9.361E -3
818	1.558E -2	7.504E -3	1.171E -2	1.406E -2	1.363E -2	2.310E -3	4.779E -4	4.862E -3	1.244E -2	7.012E -3	4.881E -3	9.361E -3
819	1.575E -2	7.504E -3	1.171E -2	1.406E -2	1.384E -2	2.375E -3	4.930E -4	4.925E -3	1.244E -2	7.135E -3	4.937E -3	9.361E -3

Table A.5 Calibrated S192 Radiances for Site B

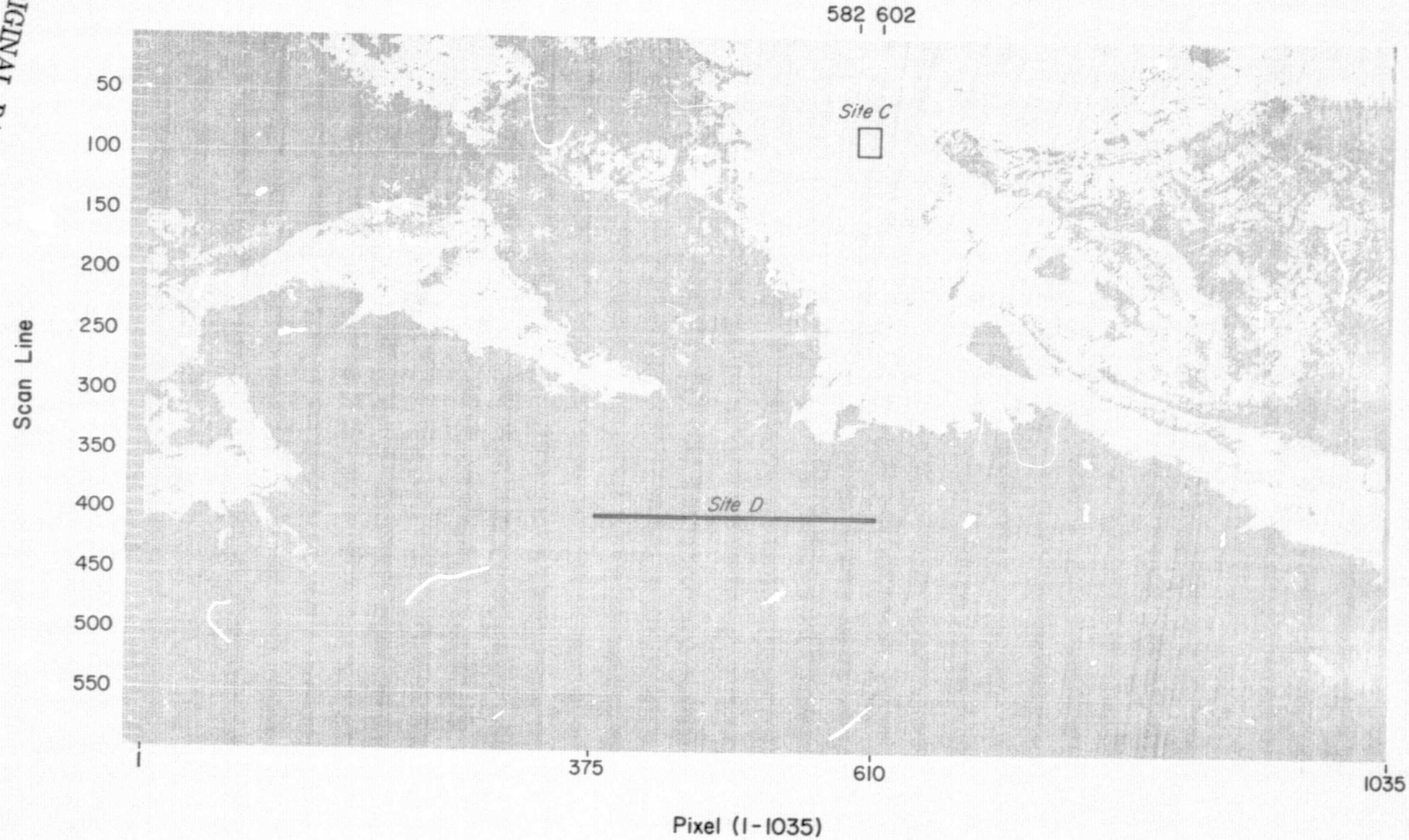

Figure A.3 Processed Image Matrix for Sites C and D (see Text)

0 0 VERSION 0.0 ( ) 0/ 0/ 0 PAGE 2

****

SCAN LINE	IHOUR	IMIN	SECONDS	SUBSAT LAT		SUB SAT LONG				SUN ANGLE			FIRST PIXEL LAT				LONG	
10	19	34	19.8389	40	59	81	-113	17	5	52	36	206	41	21	85	-113	14	124
20	19	34	19.9446	40	59	138	-113	16	130	52	36	145	41	21	142	-113	14	9
30	19	34	20.0501	40	59	190	-113	16	27	52	36	90	41	21	194	-113	13	145
40	19	34	20.1555	41	0	2	-113	15	163	52	36	35	41	22	6	-113	13	40
50	19	34	20.2613	41	0	49	-113	15	89	52	35	225	41	22	53	-113	12	186
60	19	34	20.3670	41	0	94	-113	14	221	52	35	178	41	22	97	-113	12	96
70	19	34	20.4727	41	0	153	-113	14	101	52	35	115	41	22	157	-113	11	217
80	19	34	20.5774	41	0	210	-113	13	228	52	35	55	41	22	213	-113	11	102
90	19	34	20.6829	41	1	22	-113	13	124	52	34	239	41	23	25	-113	10	237
100	19	34	20.7883	41	1	74	-113	13	21	52	34	184	41	23	77	-113	10	133
110	19	34	20.8942	41	1	121	-113	12	166	52	34	134	41	23	124	-113	10	37
120	19	34	20.9998	41	1	173	-113	12	62	52	34	79	41	23	176	-113	9	172
130	19	34	21.1055	41	1	224	-113	11	199	52	34	24	41	23	228	-113	9	67
140	19	34	21.2112	41	2	42	-113	11	84	52	33	203	41	24	45	-113	8	191
150	19	34	21.3167	41	2	93	-113	10	220	52	33	148	41	24	97	-113	8	86
160	19	34	21.4221	41	2	145	-113	10	117	52	33	92	41	24	149	-113	7	220
170	19	34	21.5271	41	2	192	-113	10	23	52	33	43	41	24	195	-113	7	125
180	19	34	21.6328	41	3	4	-113	9	159	52	32	227	41	25	7	-113	7	20
190	19	34	21.7383	41	3	55	-113	9	56	52	32	172	41	25	59	-113	6	154
200	19	34	21.8439	41	3	112	-113	8	181	52	32	111	41	25	116	-113	6	38
210	19	34	21.9495	41	3	164	-113	8	77	52	32	56	41	25	168	-113	5	173
220	19	34	22.0543	41	3	211	-113	7	224	52	32	6	41	25	215	-113	5	79
230	19	34	22.1599	41	4	23	-113	7	120	52	31	191	41	26	27	-113	4	215
240	19	34	22.2656	41	4	74	-113	7	16	52	31	136	41	26	79	-113	4	110
250	19	34	22.3713	41	4	131	-113	6	141	52	31	75	41	26	136	-113	3	234
260	19	34	22.4763	41	4	178	-113	6	48	52	31	25	41	26	183	-113	3	141
270	19	34	22.5820	41	4	230	-113	5	184	52	30	210	41	26	234	-113	3	36
280	19	34	22.6878	41	5	47	-113	5	69	52	30	148	41	27	52	-113	2	161
290	19	34	22.7932	41	5	98	-113	4	205	52	30	93	41	27	104	-113	2	57
300	19	34	22.8987	41	5	150	-113	4	101	52	30	38	41	27	155	-113	1	192
310	19	34	23.0044	41	5	197	-113	4	8	52	29	228	41	27	202	-113	1	98
320	19	34	23.1091	41	6	8	-113	3	144	52	29	172	41	28	14	-113	0	233
330	19	34	23.2149	41	6	60	-113	3	40	52	29	117	41	28	65	-113	0	128
340	19	34	23.3205	41	6	117	-113	2	165	52	29	56	41	28	122	-113	0	14
350	19	34	23.4260	41	6	169	-113	2	61	52	29	1	41	28	174	-112	59	149
360	19	34	23.5314	41	6	220	-113	1	197	52	28	185	41	29	226	-112	59	44
370	19	34	23.6375	41	7	27	-113	1	103	52	28	135	41	29	32	-112	58	190
380	19	34	23.7422	41	7	78	-113	0	239	52	28	80	41	29	84	-112	58	85
390	19	34	23.8479	41	7	135	-113	0	124	52	28	19	41	29	141	-112	57	210
400	19	34	23.9534	41	7	187	-113	0	20	52	27	203	41	29	192	-112	57	106
410	19	34	24.0588	41	7	239	-112	59	156	52	27	148	41	30	4	-112	57	1
420	19	34	24.1647	41	8	45	-112	59	63	52	27	98	41	30	50	-112	56	147
430	19	34	24.2703	41	8	97	-112	58	197	52	27	42	41	30	103	-112	56	41
440	19	34	24.3760	41	8	149	-112	58	93	52	26	226	41	30	154	-112	55	177
450	19	34	24.4807	41	8	205	-112	57	219	52	26	165	41	30	210	-112	55	62
460	19	34	24.5862	41	9	17	-112	57	115	52	26	110	41	31	22	-112	54	198
470	19	34	24.6917	41	9	68	-112	57	11	52	26	54	41	31	74	-112	54	93
480	19	34	24.7975	41	9	115	-112	56	156	52	26	4	41	31	120	-112	53	238
490	19	34	24.9031	41	9	167	-112	56	52	52	25	188	41	31	172	-112	53	133
500	19	34	25.0088	41	9	218	-112	55	188	52	25	133	41	31	224	-112	53	28
510	19	34	25.1145	41	10	35	-112	55	73	52	25	71	41	32	40	-112	52	153
520	19	34	25.2189	41	10	86	[illegible]	54	210	52	25	16	41	32	91	-112	52	49
530	19	34	25.3248	41	10	131	[illegible]	54	120	52	24	208	41	32	136	-112	51	199
540	19	34	25.4304	41	10	185	-112	54	11	52	24	150	41	32	190	-112	51	89
550	19	34	25.5361	41	10	236	-112	53	146	52	24	95	41	33	1	-112	50	224

ORIGINAL PAGE IS OF POOR QUALITY

Table A.6 Ephemeris Data for Sites C and D

ORIGINAL PAGE IS
OF POOR QUALITY

0 0 VERSION 0.0 ( ) 0/ 0/ 0 PAGE 13

DATA FOR SCAN LINE NUMBER 90

PIXEL /DATA FOR SDO(S)

NUMBER/	1	3	5	7	9	11	13	17	18	19	20	22
582	1.062E -2	1.332E -2	1.275E -2	9.322E -3	7.938E -3	1.605E -3	2.529E -4	3.307E -3	8.820E -3	4.798E -3	2.754E -3	7.750E -3
583	1.062E -2	1.311E -2	1.275E -2	9.610E -3	8.022E -3	1.681E -3	2.751E -4	3.250E -3	9.057E -3	4.889E -3	2.678E -3	7.600E -3
584	1.046E -2	1.385E -2	1.238E -2	9.726E -3	8.106E -3	1.624E -3	2.619E -4	3.279E -3	9.116E -3	4.889E -3	2.703E -3	7.787E -3
585	1.046E -2	1.405E -2	[illegible] -2	9.841E -3	8.106E -3	1.624E -3	2.618E -4	3.422E -3	8.424E -3	4.889E -3	2.728E -3	7.638E -3
586	1.054E -2	1.258E -2	1.224E -2	9.668E -3	[illegible] -3	1.662E -3	2.529E -4	3.680E -3	8.721E -3	4.798E -3	2.728E -3	7.899E -3
587	1.030E -2	1.364E -2	1.202E -2	9.668E -3	8.106E -3	1.624E -3	3.016E -4	3.651E -3	8.820E -3	4.980E -3	2.728E -3	7.824E -3
588	[illegible] -2	1.322E -2	1.202E -2	9.553E -3	8.190E -3	1.624E -3	2.529E -4	3.422E -3	8.671E -3	4.843E -3	2.804E -3	7.227E -3
589	[illegible] -2	1.291E -2	1.216E -2	9.553E -3	8.022E -3	1.587E -3	2.706E -4	3.250E -3	8.671E -3	4.843E -3	2.728E -3	7.767E -3
590	1.054E -2	1.343E -2	[illegible] -2	9.783E -3	8.274E -3	1.549E -3	2.706E -4	3.164E -3	8.968E -3	4.934E -3	2.653E -3	8.127E -3
591	1.078E -2	1.374E -2	1.297E -2	9.553E -3	8.190E -3	1.549E -3	2.706E -4	3.221E -3	8.671E -3	5.162E -3	2.653E -3	7.693E -3
592	1.038E -2	1.437E -2	1.311E -2	9.553E -3	7.685E -3	1.605E -3	2.485E -4	3.365E -3	8.671E -3	5.116E -3	2.754E -3	7.536E -3
593	1.054E -2	1.353E -2	1.311E -2	9.553E -3	7.770E -3	1.555E -3	2.395E -4	3.393E -3	8.770E -3	5.116E -3	2.804E -3	7.787E -3
594	1.056E -2	1.353E -2	1.275E -2	9.668E -3	8.022E -3	1.624E -3	2.618E -4	3.508E -3	9.017E -3	4.980E -3	2.779E -3	8.011E -3
595	1.048E -2	1.343E -2	1.253E -2	9.379E -3	7.938E -3	1.568E -3	2.751E -4	3.336E -3	9.116E -3	5.025E -3	2.678E -3	7.936E -3
596	1.014E -2	1.270E -2	1.275E -2	9.495E -3	7.685E -3	1.530E -3	2.529E -4	3.307E -3	8.671E -3	5.071E -3	2.804E -3	7.600E -3
597	1.046E -2	1.343E -2	1.253E -2	9.495E -3	7.770E -3	1.511E -3	2.618E -4	2.992E -3	8.721E -3	5.025E -3	2.829E -3	7.750E -3
598	1.078E -2	1.353E -2	1.238E -2	9.495E -3	7.854E -3	1.474E -3	2.396E -4	3.107E -3	8.820E -3	5.116E -3	2.829E -3	7.488E -3
599	1.070E -2	1.426E -2	1.173E -2	9.783E -3	7.601E -3	1.587E -3	2.662E -4	3.135E -3	8.671E -3	5.344E -3	2.804E -3	7.451E -3
600	1.070E -2	1.322E -2	1.187E -2	9.495E -3	8.022E -3	1.643E -3	2.751E -4	3.193E -3	8.820E -3	5.116E -3	2.804E -3	7.750E -3
601	1.062E -2	1.374E -2	1.195E -2	9.553E -3	8.527E -3	1.699E -3	3.061E -4	3.250E -3	8.622E -3	5.299E -3	2.829E -3	7.526E -3
602	1.046E -2	1.291E -2	1.246E -2	9.610E -3	8.022E -3	1.624E -3	2.618E -4	3.479E -3	8.622E -3	5.344E -3	2.804E -3	7.376E -3

Table A.7 Calibrated S192 Radiances for Site C

0 0 VERSION 0.0 (/ 0/ 0/ 0 PAGE 9

DATA FOR SCAN LINE NUMBER 401

PIXEL /DATA FOR SDC(S) NUMBER/	1	3	5	7	9	11	13	17	18	19	20	22
425	3.672E -3	2.466E -3	2.011E -3	1.413E -3	7.851E -4	2.135E -4	6.251E -5	4.151E -4	4.274E -3	6.535E -4	2.363E -4	2.783E -3
426	3.430E -3	2.779E -3	1.645E -3	1.643E -3	8.693E -4	1.570E -4	4.480E -5	2.146E -4	3.720E -3	5.624E -4	2.363E -4	2.655E -3
427	3.511E -3	2.779E -3	1.430E -3	1.355E -3	8.693E -4	1.194E -4	4.948E -6	1.573E -4	3.681E -3	1.525E -4	1.356E -4	2.933E -3
428	3.591E -3	2.466E -3	1.430E -3	1.239E -3	7.010E -4	1.570E -4	1.380E -5	3.291E -4	3.977E -3	1.526E -5	1.105E -4	2.970E -3
429	3.834E -3	2.361E -3	1.791E -3	1.528E -3	6.168E -4	1.194E -4	4.948E -6	3.291E -4	2.888E -3	1.681E -4	1.105E -4	2.933E -3
430	3.591E -3	2.361E -3	2.376E -3	1.643E -3	7.010E -4	2.135E -4	4.948E -6	2.146E -4	3.835E -3	1.681E -4	5.525E -5	2.709E -3
431	3.430E -3	2.674E -3	2.376E -3	1.643E -3	7.010E -4	1.570E -4	1.833E -5	4.151E -4	3.977E -3	1.526E -4	1.105E -4	2.671E -3
432	3.753E -3	3.674E -3	1.645E -3	1.413E -3	4.485E -4	1.382E -4	8.376E -6	3.578E -4	3.977E -3	2.052E -4	1.356E -4	2.634E -3
433	3.591E -3	3.092E -3	2.376E -3	1.643E -3	5.327E -4	1.382E -4	9.376E -6	3.291E -4	4.175E -3	1.070E -4	1.850E -4	2.596E -3
434	3.915E -3	3.092E -3	2.157E -3	1.413E -3	4.485E -4	1.570E -4	4.480E -5	3.578E -4	4.027E -3	2.892E -4	1.850E -4	2.558E -3
435	3.591E -3	3.715E -3	1.719E -3	1.586E -3	7.010E -4	1.570E -4	4.480E -5	3.578E -4	4.225E -3	2.437E -4	1.356E -4	2.783E -3
436	3.753E -3	3.405E -3	1.865E -3	1.643E -3	7.010E -4	1.570E -4	5.366E -5	5.216E -4	4.175E -3	2.892E -4	3.118E -4	2.746E -3
437	3.672E -3	3.301E -3	2.011E -3	1.586E -3	4.485E -4	1.194E -4	5.366E -5	3.578E -4	3.977E -3	4.255E -4	3.370E -4	2.746E -3
438	3.915E -3	2.888E -3	2.054E -3	1.643E -3	3.644E -4	1.382E -4	2.266E -5	3.034E -4	3.881E -3	2.892E -4	2.615E -4	2.634E -3
439	3.672E -3	3.092E -3	2.888E -3	1.643E -3	4.485E -4	1.006E -4	3.594E -5	1.287E -4	4.027E -3	4.255E -4	1.608E -4	2.709E -3
440	3.511E -3	2.779E -3	2.300E -3	1.643E -3	2.802E -4	1.006E -4	3.594E -5	7.142E -5	3.720E -3	5.624E -4	2.363E -4	2.709E -3
441	3.349E -3	2.674E -3	1.867E -3	1.528E -3	2.802E -4	1.194E -4	5.200E -7	2.432E -4	3.720E -3	5.169E -4	2.111E -4	2.596E -3
442	3.430E -3	2.466E -3	1.719E -3	1.528E -3	2.802E -4	1.194E -4	9.376E -6	1.573E -4	3.681E -3	2.602E -4	1.060E -4	2.281E -3
443	3.995E -3	3.092E -3	1.645E -3	1.470E -3	3.644E -4	8.181E -5	1.380E -5	2.432E -4	3.835E -3	3.803E -4	2.363E -4	3.306E -3
444	3.915E -3	2.779E -3	2.230E -3	1.528E -3	4.485E -4	1.759E -4	1.380E -5	5.010E -4	3.908E -3	2.437E -4	1.356E -4	3.119E -3
445	3.511E -3	2.888E -3	1.051E -3	1.355E -3	4.485E -4	1.382E -4	3.594E -5	2.432E -4	3.908E -3	4.208E -4	1.626E -4	3.119E -3
446	3.591E -3	2.775E -3	2.011E -3	1.355E -3	4.485E -4	1.006E -4	2.709E -5	3.291E -4	3.977E -3	3.803E -4	1.356E -4	3.134E -3
447	3.591E -3	2.361E -3	1.719E -3	1.297E -3	6.168E -4	1.006E -4	2.709E -5	2.146E -4	3.528E -3	2.437E -4	1.105E -4	3.119E -3
448	3.834E -3	2.570E -3	2.157E -3	1.124E -3	4.485E -4	1.006E -4	1.380E -5	3.005E -4	4.126E -3	2.892E -4	1.356E -4	3.232E -3
449	3.834E -3	2.888E -3	2.034E -3	1.355E -3	6.168E -4	1.382E -4	2.266E -5	3.578E -4	4.225E -3	3.347E -4	1.105E -4	3.052E -3
450	3.915E -3	3.092E -3	1.645E -3	1.413E -3	7.851E -4	1.570E -4	2.266E -5	2.432E -4	3.978E -3	2.437E -4	2.111E -4	3.453E -3
451	3.834E -3	2.674E -3	2.741E -3	1.817E -3	3.644E -4	1.006E -4	5.366E -5	3.005E -4	4.373E -3	4.255E -4	2.363E -4	3.082E -3
452	3.995E -3	3.510E -3	1.865E -3	1.528E -3	7.010E -4	1.382E -4	1.833E -5	2.719E -4	3.977E -3	3.347E -4	1.376E -4	2.783E -3
453	4.319E -3	2.888E -3	1.923E -3	1.413E -3	7.010E -4	1.006E -4	3.594E -5	3.578E -4	3.879E -3	5.169E -4	1.850E -4	2.783E -3
454	4.235E -3	3.092E -3	2.157E -3	1.586E -3	8.693E -4	1.759E -4	3.594E -5	2.719E -4	4.225E -3	5.167E -4	1.830E -4	3.232E -3
455	4.225E -3	3.156E -3	2.376E -3	1.643E -3	8.692E -4	1.006E -4	4.490E -5	3.005E -4	4.521E -3	6.575E -4	1.606E -4	3.007E -3
456	3.834E -3	2.674E -3	2.157E -3	1.586E -3	7.851E -4	1.759E -4	4.480E -5	1.287E -4	4.373E -3	4.714E -4	3.118E -4	3.157E -3
457	3.834E -3	2.888E -3	2.157E -3	1.643E -3	7.010E -4	1.570E -4	4.480E -5	3.005E -4	4.126E -3	4.253E -4	3.873E -4	2.821E -3
458	3.753E -3	2.775E -3	1.428E -3	1.470E -3	4.495E -4	1.194E -4	2.246E -5	1.860E -4	4.225E -3	3.803E -4	1.605E -4	3.082E -3
459	3.834E -3	3.156E -3	1.865E -3	1.470E -3	5.327E -4	8.181E -5	2.709E -5	1.287E -4	4.420E -3	3.803E -4	1.820E -4	3.082E -3
460	3.753E -3	3.405E -3	1.865E -3	1.239E -3	6.168E -4	6.700E -5	2.266E -5	3.005E -4	4.225E -3	3.347E -4	1.105E -4	2.821E -3
461	3.915E -3	3.092E -3	2.011E -3	1.470E -3	8.653E -4	1.382E -4	2.266E -5	2.719E -4	4.126E -3	3.347E -4	3.424E -5	2.783E -3
462	3.834E -3	2.674E -3	1.430E -3	1.701E -3	7.851E -4	1.570E -4	2.709E -5	1.860E -4	4.126E -3	4.258E -4	8.528E -5	3.306E -3
463	3.995E -3	3.301E -3	1.719E -3	1.701E -3	7.010E -4	1.570E -4	4.480E -5	2.719E -4	4.225E -3	6.080E -4	1.850E -4	2.671E -3
464	3.672E -3	2.674E -3	2.011E -3	1.413E -3	7.010E -4	1.570E -4	3.594E -5	2.719E -4	4.175E -3	5.624E -4	1.866E -4	2.905E -3
465	3.672E -3	3.301E -3	2.157E -3	1.586E -3	4.485E -4	1.570E -4	3.152E -5	3.005E -4	4.225E -3	5.169E -4	1.608E -4	2.432E -3
466	3.591E -3	2.888E -3	2.230E -3	1.586E -3	6.168E -4	1.194E -4	3.152E -5	1.573E -4	4.126E -3	6.080E -4	2.363E -4	3.206E -3
467	3.915E -3	3.156E -3	1.719E -3	1.528E -3	7.010E -4	1.759E -4	9.376E -6	2.719E -4	4.373E -3	4.714E -4	2.607E -4	3.119E -3
468	3.995E -3	3.405E -3	2.011E -3	1.586E -3	7.010E -4	1.759E -4	4.923E -5	1.860E -4	4.373E -3	6.080E -4	1.856E -4	3.082E -3
469	3.995E -3	2.466E -3	2.230E -3	1.759E -3	5.327E -4	1.759E -4	1.380E -5	3.005E -4	3.977E -3	7.901E -4	1.356E -4	3.306E -3
470	4.157E -3	3.405E -3	1.572E -3	1.701E -3	5.327E -4	1.036E -4	3.152E -5	3.005E -4	4.274E -3	5.624E -4	1.356E -4	3.082E -3
471	3.834E -3	3.092E -3	1.280E -3	1.759E -3	4.485E -4	1.570E -4	4.420E -5	2.432E -4	4.373E -3	4.714E -4	1.105E -4	3.082E -3
472	3.834E -3	2.888E -3	2.011E -3	1.701E -3	3.644E -4	1.382E -4	3.152E -5	2.719E -4	4.076E -3	4.714E -4	1.105E -4	3.007E -3
473	4.076E -3	2.570E -3	2.011E -3	1.586E -3	4.485E -4	1.755E -4	2.266E -5	2.719E -4	4.125E -3	4.256E -4	2.111E -4	3.119E -3
474	3.753E -3	3.510E -3	1.353E -3	1.759E -3	7.010E -4	1.382E -4	4.923E -5	1.287E -4	4.126E -3	4.258E -4	2.615E -4	3.119E -3
475	3.753E -3	2.674E -3	1.719E -3	1.556E -3	6.168E -4	1.194E -4	4.037E -5	7.142E -5	3.923E -3	4.714E -4	2.363E -4	3.119E -3

ORIGINAL PAGE IS OF POOR QUALITY

Table A.8 Calibrated Radiances for Site D